Analysis and Simulation of Piezoelectric Vibration Energy Harvesters Having Uniform Stress Profile

A thesis submitted in partial fulfilment of the requirements for the degree of

DOCTOR OF PHILOSOPHY

by

SUSHANTA KUNDU

Department of Electronics and Electrical Engineering
Indian Institute of Technology Guwahati
Guwahati, Assam, India - 781039
January 2022

CERTIFICATE

This is to certify that the thesis entitled "**Analysis and Simulation of Piezoelectric Vibration Energy Harvesters Having Uniform Stress Profile**," submitted by Sushanta Kundu (11610204), a research scholar in the Department of Electronics and Electrical Engineering, Indian Institute of Technology Guwahati, for the award of the degree of Doctor of Philosophy, is a record of an original research work carried out by him under my supervision and guidance. The thesis has fulfilled all requirements as per the regulations of the Institute and in my opinion has reached the standard needed for submission. The results embodied in this thesis have not been submitted to any other University or Institute for the award of any degree or diploma.

Dated:

Guwahati

Prof. Harshal B. Nemade
Professor
Department of Electronics and Electrical Engineering
Indian Institute of Technology Guwahati
Guwahati - 781 039, Assam, India

DECLARATION

This is to declare that the thesis entitled "**Analysis and Simulation of Piezoelectric Vibration Energy Harvesters Having Uniform Stress Profile**," submitted by me to the Indian Institute of Technology Guwahati for the award of the degree of Doctor of Philosophy, is a bonafide record of research work carried out by me under the supervision of Prof. Harshal B. Nemade. Hereby I declare that the contents of this thesis, in full or in parts, have not been submitted to any other University or Institute for the award of any degree or diploma.

Dated:

Guwahati

Sushanta Kundu

ACKNOWLEDGMENT

I express my deepest and most sincere gratitude to my supervisor Prof. Harshal B. Nemade, for his guidance, help, and encouragement throughout my research work. I am grateful to him for all the discussions, the knowledge he imparted, and the academic freedom he has given me. I greatly admire his attitude towards research and creative thinking. His insightful feedbacks have helped me immensely in improving myself scientifically and personally.

I am grateful to my doctoral committee chairman, Prof. Roy P. Paily, for his critical assessment during the entire period of progress. I extend my sincere thanks to my doctoral committee members, Prof. Pravat K. Giri and Dr. Gaurav Trivedi, for their support, encouragement, and suggestions rendered during my research work.

My special thanks to the technical and administrative staff of the EEE Department, IIT Guwahati, Sri Sidananda Sonowal, Dr. Sanjeev Das, Sri Pranab J Goswami, Dr. Madhuriya P. Das, Sri Mukut Baruah, Sri Dasarath Das, without their help, I could not have completed this thesis.

My special thanks to Dr. Basudeba Behera, Dr. Shyam Trivedi, Dr. Jitendra, Dr. Vivek Lukose, Mandar Maitra, Dr. Arijit Roy, Gautam, Raju, Kasturi, Tamen, Santosh for their help support and all the helpful technical discussions.

I want to express my immense gratitude and heartfelt thanks to my parents, Smt. Bibha Bati Kundu and Late. Nilkamal Kundu for their support, encouragement, and kind blessings. I would like to thank my elder brothers, Dr. Shyam Sundar Kundu and Sri Jayanta Kundu, for the fruitful discussions, great support, and encouragement. I express my gratitude to my better half Smt. Rubi Pegu, for all her patience and kind support.

Sushanta Kundu

ABSTRACT

With the evolution of low-power electronic devices, self-powered micro-sensors and communication nodes have become more realistic. At the same time, the need to power remote systems or embedded devices independently has motivated many researchers towards harvesting electrical energy from various ambient energy sources. Mechanical vibration is a valuable energy source that has been used to harvest electrical energy in past decades. The simplicity and compatibility of the piezoelectric energy harvesters attracted many researchers to work on vibration energy harvesters. The majority of the vibration energy harvesters are based on piezoelectric cantilever beams.

The objective of the presented work is to improve the electrical power output by modifying the geometry of the piezoelectric vibration energy harvester (PVEH). The main contributions of the thesis are as follows. The thickness profile of bimorph cantilever-based conventional PVEH is modified to achieve uniform stress along the beam length. Two new thickness-tapered geometries are proposed. The first geometry, PVEH-1, consists of a substrate of tapered thickness profile and piezoelectric layers of uniform thickness. The second proposed geometry, PVEH-2, consists of a bimorph cantilever with a substrate of uniform thickness and piezoelectric layers of tapered thickness profile. The third contribution is about improving the power output of conventional diaphragm-based PVEH by dividing the diaphragm into several identical slices (*sectors*). Further, a broadband energy harvester is designed using several slices of different central angles.

In the conventional cantilever-based PVEH of uniform thickness, the stress on the surface is maximum at the fixed end and decreases linearly to zero at the free end. The high-stress area is prone to mechanical failure while the piezoelectric material towards the free end remains underutilized. To resolve this issue, modification is proposed in the thickness profile of the cantilever-based PVEH, and two novel geometries for PVEH are introduced. The first proposed geometry (PVEH-1) consists of a thickness-tapered substrate layer sandwiched between two piezoelectric layers of uniform thickness. The second proposed geometry (PVEH-2) consists of a uniform substrate layer sandwiched between two piezoelectric layers of tapered thickness.

Analytical expressions for resonance frequency, end-mass displacement, generated power, and stress profile are derived for PVEH-1 and PVEH-2. The results from the derived analytical expressions are validated by comparing with the results from FE analysis of each geometry. The

harvested power and the stress profile of the proposed PVEH-1 are compared with the harvested power and stress profile of an equivalent conventional PVEH. The proposed PVEH-1 generates more power by experiencing less peak stress than the equivalent conventional PVEH. Similarly, the PVEH-2 showed more generated power and less peak stress than the equivalent conventional PVEH. Because of reduced peak stress, both the proposed PVEH are suitable for harvesting energy from vibration sources of high accelerations.

Another popular geometry investigated in the thesis is diaphragm-based PVEH. The diaphragm-based PVEH generally has a high resonance frequency of vibration, and the stress distribution is mainly concentrated at the central portion only and responsible for most of the generated electrical power. A diaphragm-based PVEH is modified by dividing into several identical sectors to reduce the resonance frequency and improve the stress distribution. FE analysis is carried out to find resonance frequency, proof-mass displacement, stress profile, and generated power. It is observed that the slicing of the diaphragm reduces the resonance frequency of vibration and increases the harvested power. The optimal slicing angle for the best performance is found from the FE analysis results. It is also observed that the slices of different angles exhibit different resonance frequencies. A set of different angular slices are combined to design a broadband energy harvester.

TABLE OF CONTENTS

Certificate i
Declaration iii
Acknowledgment v
Abstract vii
Table of contents ix
List of figures xv
List of tables xix
Abbreviations xxi
Symbols xxiii
1. INTRODUCTION 1
1.1 Applications of energy harvester 1
1.2 Sources of energy harvesting 2
1.2.1 Solar energy harvesting 2
1.2.2 Thermoelectric energy harvesting 3
1.2.3 Vibration energy harvesting 3
1.3 Vibration energy harvesting 4
1.3.1 Electromagnetic system 5
1.3.2 Electrostatic system 6
1.3.3 Piezoelectric system 6
1.4 Piezoelectric vibration energy harvester (PVEH) 7
1.4.1 Piezoelectric materials 7
1.4.2 Piezoelectric constitutive equations 8
1.5 Cantilever-based PVEH 10
1.5.1 Types of cantilever-based PVEH 11
1.6 Diaphragm-based PVEH 12
1.7 Nonlinear PVEH 12
1.8 Literature review of PVEH 13
1.8.1 Literature survey on cantilever-based PVEH 13
1.8.2 Literature survey on diaphragm-based PVEH 17
1.9 Fabrication methods 18
1.10 Stress distribution on the conventional PVEH 19
1.11 Strategies to solve stress non-uniformity 19
1.12 Research gap 21

1.13 Objective of the thesis 22
1.14 Thesis contribution 23
1.15 Scope of the thesis 23
1.16 Thesis outline 24
2. FINITE ELEMENT ANALYSIS OF PVEH 27
2.1 FE modeling and simulation 28
2.1.1 FE analysis of bimorph PVEH 28
2.1.2 Types of FE analysis 29
2.1.3 Simulated PVEH geometry 29
2.2 Simulation results 30
2.2.1 Resonance frequency of vibration 30
2.2.2 Time-domain analysis 31
2.2.3 Frequency domain analysis 32
2.3 Comparison of results 33
2.4 Conclusions 34
3. PVEH OF UNIFORM THICKNESS 37
3.1 Modeling assumptions 37
3.2 Model derivation 38
3.2.1 PVEH with parallel connection of the piezoelectric layers 40
3.2.2 PVEH with series connection of the piezoelectric layers 41
3.3 Natural frequency of the PVEH 42
3.4 Model validation by FE analysis 42
3.4.1 FE modeling in COMSOL Multiphysics 42
3.4.2 Short-circuit and open-circuit analysis 43
3.4.3 Effect of load resistance 43
3.4.4 Performance at optimal load resistance 45
3.4.5 Variation of voltage and current with the load resistor 46
3.4.6 Damping effect of the load resistance 47
3.5 Power density 49
3.6 Conclusions 49
4. THICKNESS PROFILE FOR UNIFORM STRESS IN PVEH 51
4.1 Stress and power relation 52
4.2 Stress on the conventional cantilever beam 52
4.3 Derivation of thickness profile for uniform stress 54
4.4 Design of PVEH with uniform stress 56
4.4.1 PVEH-1 (Thickness-tapered substrate) 57

4.4.2 PVEH-2 (Thickness-tapered piezoelectric layer) 57
4.5 Conclusions 57
5. ANALYSIS OF PVEH-1 (THICKNESS-TAPERED SUBSTRATE) 59
5.1 Derivation of analytical expressions for PVEH-1 59
5.1.1 Geometry and assumptions 59
5.1.2 Derivation of spring constant and resonance frequency 60
5.1.3 Stress on the piezoelectric material 62
5.1.4 Derivation of coupled equations 63
5.1.5 Parallel connection of piezoelectric layers 65
5.1.6 Series connection of piezoelectric layers 65
5.2 Geometrical and material properties of PVEH-1 66
5.3 Results from the derived analytical expressions 67
5.3.1 Calculation of resonance frequency 67
5.3.2 Variation of end-mass displacement with load resistance 68
5.3.3 Variation of electrical power with load resistance 68
5.4 Comparison of analytical results with FE analysis 69
5.4.1 Comparison of end-mass displacement 69
5.4.2 Comparison of generated power at optimal load resistance 70
5.4.3 Comparison of the stress profile 71
5.5 Comparison with conventional PVEH 72
5.5.1 Comparison of the end-mass displacement 73
5.5.2 Comparison of the stress profiles 73
5.5.3 Comparison of generated power 75
5.5.4 Comparison of generated power at equal stress 75
5.6 Input acceleration and power 77
5.7 Power density 78
5.8 Advantages of the proposed thickness-tapered PVEH-1 78
5.9 Possible fabrication technique for PVEH-1 79
5.10 Conclusions 79
6. ANALYSIS OF PVEH-2 (THICKNESS-TAPERED PIEZOELECTRIC LAYER) 81
6.1 Derivation of analytical expressions for PVEH-2 81
6.1.1 Geometry and assumptions 81
6.1.2 Derivation of spring constant and resonance frequency 83
6.1.3 Stress on the piezoelectric material 84
6.1.4 Derivation of coupled equations 85
6.1.5 Parallel connection of piezoelectric layers 85

6.1.6 Series connection of piezoelectric layers 86
6.2 Geometrical and material properties of PVEH-2 86
6.3 Results from the derived analytical expressions 87
6.3.1 Calculation of resonance frequency 87
6.3.2 Variation of end-mass displacement with load resistance 88
6.3.3 Variation of electrical power with load resistance 88
6.4 Comparison of analytical results with FE analysis 89
6.4.1 Comparison of end-mass displacement 89
6.4.2 Comparison of generated power at optimal load resistance 90
6.4.3 Comparison of the stress profile 91
6.5 Comparison with conventional PVEH 92
6.5.1 Comparison of end-mass displacement 93
6.5.2 Comparison of the stress profile 93
6.5.3 Comparison of generated power 95
6.5.4 Comparison of generated power at equal stress 95
6.6 Power density 96
6.7 Advantages of the proposed PVEH-2 over conventional PVEH 97
6.8 Possible fabrication technique for PVEH-2 97
6.9 Comparison of Proposed PVEH-1 and PVEH-2 98
6.10 Conclusions 99
7. ANALYSIS OF DIAPHRAGM-BASED PVEH 101
7.1 FE analysis of the diaphragm-based PVEH 101
7.1.1 Resonance frequency of vibration 102
7.1.2 Voltage and power from the PVEH 103
7.1.3 Stress profile on the diaphragm surface 104
7.3 Angular slicing of the diaphragm 105
7.3.1 Angular slicing 106
7.3.2 FE analysis of the angular slices 106
7.3.3 Optimal slicing angle 111
7.4 Broadband PVEH using angular slices 113
7.4.1 Design of the broadband PVEH 113
7.5. Results from the broadband PVEH 114
7.5.1 Displacement of the proof mass 114
7.5.2 Stress on the surfaces 115
7.5.3 Generated power from the broadband PVEH 116
7.6 Advantages of using slices 116

7.7 Possible fabrication approach for the diaphragm-based PVEH 117
7.8 Conclusions 117
8. CONCLUSIONS AND FUTURE SCOPE 119
PUBLICATIONS 123
BIBLIOGRAPHY 125

LIST OF FIGURES

Figure 1.1: General model of the vibration energy harvester. 5

Figure 1.2: Typical electromagnetic energy harvester. 5

Figure 1.3: An example of (a) Molecular model of a piezoelectric material, (b) Molecular model under stress, (c) Polarizing effect on the bulk material. 7

Figure 1.4: Piezoelectric cantilever beam. 11

Figure 1.5: Different configurations of piezoelectric and substrate layers. 11

Figure 1.6: Diaphragm-based PVEH. 12

Figure 2.1: A cantilever-based bimorph PVEH. 28

Figure 2.2: Meshing of cantilever-based PVEH. 29

Figure 2.3: Original device described in [84] and corresponding simulated device. 30

Figure 2.4: (a) Mode shape at the fundamental resonance frequency, (b) plot of displacement versus frequency for short-circuit and open-circuit conditions. 31

Figure 2.5: Plot of end-mass and base displacements versus time obtained from FE analysis 31

Figure 2.6: Time-domain response of PVEH at 20 Hz frequency. 32

Figure 2.7: Time-domain response of PVEH at 80 Hz frequency. 32

Figure 2.8: Plot of end-mass displacement versus frequency. 33

Figure 2.9: Plot of power versus frequency from (a) analytical expressions reported in [135] and (b) FE simulation 33

Figure 2.10. Plot of end-mass displacement versus frequency from (a) analytical expressions reported in [135] and (b) FE simulation. 34

Figure 3.1**:** Side view of energy harvester and cross-sectional view of the bimorph. 37

Figure 3.2**:** (a) parallel and (b) series connection of bimorph. 38

Figure 3.3: Spring-mass-damper model of PVEH. 38

Figure 3.4: Plots of end-mass displacement versus excitation frequency obtained from (a) analytical expression and (b) FE simulation 44

Figure 3.5: Plots of generated power versus input frequency for different load resistances obtained using (a) analytical expression and (b) FE simulation. 44

Figure 3.6: Plots of end-mass displacement for 10 kΩ load versus frequency obtained from (a) analytical expression and (b) FE simulation. 45

Figure 3.7: Plots of harvested power for 10 kΩ load versus frequency obtained from (a) analytical expression and (b) FE simulation 45

Figure 3.8: Variation of the peak voltage with load resistance for input excitations at the short-circuit resonance frequency (100 Hz) and open-circuit resonance frequency (105.5 Hz) using analytical expression (MATLAB) and FE analysis (COMSOL). 46

Figure 3.9: Variation of the peak current with load resistance for input excitations at the short-circuit resonance frequency (100 Hz) and open-circuit resonance frequency (105.5 Hz) using analytical expression (MATLAB) and FE analysis (COMSOL). 46

Figure 3.10: Variation of the peak power with load resistance for excitations at the short-circuit resonance frequency (100 Hz) and open-circuit resonance frequency (105.5 Hz) using analytical expression (MATLAB) and FE analysis (COMSOL). 47

Figure 3.11: Plots of (a) displacement of end-mass and (b) generated power versus load resistance at the resonance frequency..... 48

Figure 4.1: Side view of a conventional cantilever beam. 52

Figure 4.2: Stress distribution on a conventional cantilever calculated from (4.8). 54

Figure 4.3: Stress distribution on a conventional cantilever obtained from FE analysis. 54

Figure 4.4: (a) side view, and (b) 3D view of the thickness-tapered cantilever beam. 55

Figure 4.5: Stress distribution on (a) conventional and (b) thickness-tapered cantilever from FE simulation..... 56

Figure 4.6: Side view of the PVEH-1 geometry. 57

Figure 4.7: Side view of the PVEH-2 geometry. 57

Figure 5.1: Side view of the PVEH-1. 60

Figure 5.2: Cross-section view of the beam. 60

Figure 5.3: Equivalent spring-mass-damper model of an energy harvester. 64

Figure 5.4: Geometry of PVEH-1 simulated in COMSOL Multiphysics. 67

Figure 5.5: First vibration mode shape of PVEH-1. 67

Figure 5.6: Plot of end-mass displacement versus frequency for various load resistance values. 68

Figure 5.7: Plot of power versus frequency for various load resistance values. 69

Figure 5.8: Plot of end-mass displacement versus frequency at short-circuit condition from (a) the derived analytical expression and (b) FE analysis. 69

Figure 5.9: Plot of end-mass displacement versus frequency at optimal load from (a) the derived analytical expression and (b) FE analysis. 70

Figure 5.10: Plot of power versus frequency at optimal load obtained from (a) analytical expression and (b) FE analysis. 70

Figure 5.11: Stress distribution along the length obtained from (a) analytical result and (b) FE analysis. 71

Figure 5.12: Geometry of the equivalent conventional PVEH. 73

Figure 5.13: Comparison of end-mass displacement of PVEH-1 (tapered thickness) and conventional PVEH (uniform thickness). 73

Figure 5.14: Comparison of stress distribution along the length of (a) proposed PVEH-1 and (b) conventional PVEH. 74

Figure 5.15: 3-D view of stress distribution on the (a) proposed PVEH-1 and (b) conventional PVEH. 74

Figure 5.16: Comparison of harvested power from proposed PVEH-1 (tapered thickness) and conventional PVEH (uniform thickness). 75

Figure 5.17: Stress profile comparison of the proposed PVEH-1 (tapered thickness) and conventional PVEH (uniform thickness) for equal peak stress of 10 MPa. 76

Figure 5.18: Generated power from the proposed PVEH-1 (tapered thickness) and conventional PVEH (uniform thickness) for equal peak stress of 10 MPa..... 76

Figure 5.19: Variation of power for different input accelerations for the proposed PVEH-1. 77

Figure 5.20: Variation of power for different input accelerations for the conventional PVEH. 77

Figure 6.1: Side view of PVEH-2. 82

Figure 6.2: Cross-section view of the PVEH-2 beam. 82

Figure 6.3: Geometry of PVEH-2 simulated in COMSOL Multiphysics. 87

Figure 6.4: Plot of end-mass displacement versus frequency for various load resistance values. 88

Figure 6.5: Plot of power versus frequency for various load resistance values. 89

Figure 6.6: Plot of end-mass displacement versus frequency at short-circuit condition from (a) the derived analytical expression and (b) FE analysis. 90

Figure 6.7: Plot of end-mass displacement versus frequency at optimal load from (a) the derived analytical expression and (b) FE analysis. 90

Figure 6.8: Plot of power versus frequency at optimal load obtained from (a) analytical expression and (b) FE analysis. 91

Figure 6.9: Stress distribution along the length obtained from (a) analytical result and (b) FE analysis. 91

Figure 6.10: Geometry of the equivalent conventional PVEH. 93

Figure 6.11: Comparison of end-mass displacement of PVEH-2 (tapered thickness) and conventional PVEH (uniform thickness). 93

Figure 6.12: Comparison of stress distribution along the length of PVEH-2 (tapered thickness) and conventional PVEH (uniform thickness). 94

Figure 6.13: 3-D view of stress distribution on the (a) proposed PVEH-2 and (b) conventional PVEH. 94

Figure 6.14: Comparison of harvested power from proposed PVEH-2 (tapered thickness) and conventional PVEH (uniform thickness). 95

Figure 6.15: Stress profile comparison of the proposed PVEH-2 (tapered thickness) and conventional PVEH (uniform thickness) for equal peak stress of 10 MPa. 96

Figure 6.16: Generated power from the proposed PVEH-2 (tapered thickness) and conventional PVEH (uniform thickness) for equal peak stress of 10 MPa. 96

Figure 6.17: Thickness-tapered beam using several layers of piezoelectric material. 98

Figure 7.1: Geometry of circular diaphragm-based PVEH. 102

Figure 7.2: Plot of displacement versus frequency for short-circuit and open-circuit conditions. 103
Figure 7.3: Distribution of voltage on the diaphragm surface. 103
Figure 7.4: Plot of proof mass displacement versus frequency at optimal load. 104
Figure 7.5: Plot of generated power versus frequency at optimal load. 104
Figure 7.6: Distribution of stress on the diaphragm surface. 105
Figure 7.7: Angular slicing of the diaphragm. 105
Figure 7.8: 3-D view of the diaphragm divided in equal slices each of angle (a) 90^{o} and (b) 36^{o}. 106
Figure 7.9: Plots of (a) total power generated in the diaphragm versus frequency and (b) stress distribution in 120^{0} slice. 107
Figure 7.10: Plots of (a) total power generated in the diaphragm versus frequency and (b) stress distribution in 90^{0} slice. 107
Figure 7.11: Plots of (a) total power generated in the diaphragm versus frequency and (b) stress distribution in 60^{o} slice. 107
Figure 7.12: Plots of (a) total power generated in the diaphragm versus frequency and (b) stress distribution in 45^{o} slice. 108
Figure 7.13: Plots of (a) total power generated in the diaphragm versus frequency and (b) stress distribution in 36^{o} slice. 108
Figure 7.14: Plots of (a) total power generated in the diaphragm versus frequency and (b) stress distribution in 20^{o} slice. 108
Figure 7.15: Plots of (a) total power generated in the diaphragm versus frequency and (b) stress distribution in 10^{o} slice. 109
Figure 7.16: Variation of peak stress and power density with slicing angle. 111
Figure 7.17: Displacement profile of 32.7^{o} slices from FE simulation. 111
Figure 7.18: Plot of generated power versus frequency from the conventional diaphragm and divided diaphragm sliced with 32.7^{o}. 112
Figure 7.19: Stress distribution on the 32.7^{o} slices. 112
Figure 7.20: A 3-D view of the broadband PVEH geometry. 114
Figure 7.21: Displacement of the mass for different angular slices. 114
Figure 7.22: Stress profile on the surface for input frequencies (a) 120 Hz, (b) 125 Hz, (c) 130 Hz, (d) 135 Hz, and (e) 140 Hz. 116
Figure 7.23: Plot of generated power versus frequency for individual slices and their combination. 116

LIST OF TABLES

Table 1.1: Available energy sources for generating electrical energy. 2
Table 1.2: Power density comparison of ambient energy sources [22], [23]. 3
Table 1.3: Peak frequency and acceleration amplitude of various vibration sources [23]. 4
Table 1.4 Comparison of three types of vibration energy harvesters. 6
Table 1.5 Properties of some piezoelectric materials [46]–[49]. 8
Table 2.1: Geometric and material properties of the simulated PVEH. 30
Table 2.2: Comparison of results from MATLAB and COMSOL. 34
Table 3.1: Geometric and material parameters used in the simulation. 43
Table 3.2: Variation of resonance frequency with the load resistance. 48
Table 3.3: Comparison of results from analytical expressions and FE analysis. 49
Table 4.1: Geometric parameters of the conventional cantilever to study the stress profile. 53
Table 5.1: Geometric and material parameters of the simulated PVEH-1. 66
Table 5.2: Comparison of results using the analytical expressions and FE analysis. 71
Table 5.3: Geometrical and material parameters of the equivalent conventional PVEH. 72
Table 5.4: Output comparison of the proposed and conventional PVEH. 77
Table 5.5: Comparison of the proposed PVEH-1 and conventional PVEH at different accelerations. 78
Table 6.1: Geometric and material parameters of the simulated PVEH-2. 87
Table 6.2: Comparison of results using analytical model and FE analysis. 92
Table 6.3: Geometrical parameters of the equivalent conventional PVEH. 92
Table 6.4: Output comparison of the proposed and conventional PVEH. 97
Table 6.5: Comparison of proposed PVEH-1 and PVEH-2 98
Table 7.1: Geometrical and material parameters of the diaphragm. 102
Table 7.2: Performance comparison of diaphragm divided in different *n* number of slices. 110
Table 7.3: Details of the angular slices used to design broadband PVEH. 113

ABBREVIATIONS

AC	Alternate Current
BTO	Barium Titanate
DC	Direct Current
EM Waves	Electromagnetic Waves
FE	Finite Element
FEA	Finite Element Analysis
HMS	Health Monitoring System
KE	Kinetic Energy
MEMS	Microelectromechanical System
PE	Potential Energy
PEH	Piezoelectric Energy Harvester
PVDF	Polyvinylidene Fluoride
PVEH	Piezoelectric Vibration Energy Harvester
PZT	Lead Zirconate Titanate
RF	Radio Frequency
VEH	Vibration Energy Harvester
WSN	Wireless Sensor Nodes

SYMBOLS

b	Cantilever beam width
b_m	Mechanical damping coefficient
C_p	Capacitance of piezoelectric layer
D	Charge density displacement
d_{31}, d_{33}	Piezoelectric charge constant for 31 and 33 modes
E	Electric field
F	Force on the end-mass
g	Acceleration due to gravity (9.81 m/s^2)
g_{31}, g_{33}	Piezoelectric voltage constant for 31 and 33 modes
h_o	Beam thickness at the fixed end
h_p	Piezoelectric layer thickness
$h_p(x)$	Varying thickness of piezoelectric layer
h_{ps}	Distance between the center of piezoelectric layer and the NA
$h_{ps}(x)$	Distance between the center of piezoelectric layer and NA of thickness-tapered beam
h_s	Substrate layer thickness
$h_s(x)$	Varying thickness of substrate layer
I	Cross-section moment of inertia of cantilever beam
i	Current through load resistance
k	Spring constant of cantilever
k_{31}, k_{33}	Piezoelectric coupling coefficients for 31 and 33 modes
L	Cantilever beam length
l_b	End-mass width
L_{eff}	Effective length of cantilever

l_h	End-mass thickness
l_m	Length of end-mass
L_p	Length of piezoelectric layer
m_e	Equivalent mass of cantilever
M_t	Mass of the end-mass
$M(x)$	Moment of cantilever
NA	Neutral axis of composite beam
q	Charge on the electrode
R	Load resistance
s_{11}, s_{33}, s_{15}	Elastic compliance of piezoelectric material
S	Strain
T	Stress
T_c	Curie temperature of piezoelectric material
T_k	Maximum kinetic energy
U	Maximum potential energy
v	Generated voltage across load resistance
$v(t)$	Time varying output voltage
$y(t)$	Time varying amplitude of input vibration
Y_0	peak amplitude of input vibration
Y_s	Young's modulus of substrate material
Y_p	Young's modulus of piezoelectric material
$\ddot{y}$	Input acceleration at the base
YI	Bending stiffness of cantilever beam
Z	peak displacement of the end-mass
$z(t)$	Time varying end-mass displacement

Greek Symbols

ε_{33}	Permittivity of piezoelectric material
ε_o	Permittivity of free space
ζ_m	Mechanical damping ratio
η	Ratio of Young's moduli of the substrate and the piezoelectric material
θ	damping coefficient of PVEH due to electromechanical energy conversion
ρ_s	Mass density of substrate material (PZT-5H)
ρ_p	Mass density of piezoelectric material (Brass)
ρ_m	Mass density of end-mass material
ρ	Mass per unit length of composite beam
ω_n	Resonance frequency of vibration
ω	Frequency of input vibration

CHAPTER 1

INTRODUCTION

The perception of energy harvesting generally relates to the process of using ambient energy, which is converted largely into electrical energy in order to power small and autonomous electronic devices. Energy harvesting, energy scavenging, power harvesting, and power scavenging are the most commonly used four terms describing the same process [1]. The main components of an energy harvester are the generator which converts available ambient energy into electrical energy, the controller circuit which regulates the generated voltage, and the storage which can be a battery or a supercapacitor [2].

1.1 APPLICATIONS OF ENERGY HARVESTER

Research in vibration energy harvesting has escalated as the power requirement of electronic components reduced considerably due to recent advancements in semiconductor technology. The eventual goal in this field is to power electronic devices by using the freely available energy in the environment. Achieving this goal will minimize the requirement for an external power source and periodic replacement of batteries for electronic devices.

The primary use of energy harvesters is in powering devices for health monitoring of large structures and machineries like buildings [3], [4], bridges [5]–[7], railways [8], [9], airplanes [10]–[12], etc. Energy harvesting systems are used to power wireless acceleration sensors for building condition monitoring [4], to power acoustic sensors and scour detectors in bridges for structural health monitoring [5], [7]. Energy harvesters are also used to power ZigBee nodes for railway condition monitoring [12] and as a backup source for various low-power sensors in an airplane [11].

Energy harvesting system is also used for powering tire pressure monitoring systems [13] and accelerometers [14]. Usually, in health monitoring systems (HMS), wireless sensor nodes (WSN) are used for data transfer [15], and the nodes are generally powered by energy harvesting

systems. Besides, energy harvesting systems can be used to power wearable electronics [16], and it has the potential to power medical implants like artificial pacemakers, cochlear implants, etc. in the near future [17].

In the past decade, several research groups have developed energy harvesting systems to harness energy from solar, wind, temperature gradient, vibration, EM waves etc.

1.2 SOURCES OF ENERGY HARVESTING

In recent years, numerous energy harvesting methods have been proposed using thermoelectric, EM waves, solar, vibrations, human movements, ocean currents, etc. Table 1.1 lists some of the readily available energy sources that have been tapped for generating electricity or have the potential to be employed in energy harvesting [18]–[21].

Table 1.1: Available energy sources for generating electrical energy.

Energy sources and examples	
Environment	Solar, wind, temperature gradient, daily temperature, ocean currents, EM waves, acoustic waves, RF signal.
Structures	Bridges, tunnels, roads, control-switch, farmhouse, ducts, cleaners.
Vehicles	Trains, tires, tracks, aircraft, helicopters, automobiles, peddles, brakes, shock absorbers, turbines.
Human body	Breathing, skin temperature, arm motion while walking, blood pressure, jogging, swimming, eating, talking, finger motion.
Industrial	Motors, vibrating machines, chillier, compressors, pumps, conveyors, fans, cutting and dicing.

Among the different ambient energy sources mentioned above, thermoelectric generators, vibration/kinetic driven power generators, and solar cells are the most widely studied because of their ubiquity, high efficiency, suitable power density, and potentials for miniaturization. The power density of different ambient energy sources is compared in Table 1.2.

1.2.1 Solar energy harvesting

Solar power harvesting systems are one of the most commonly considered strategies of energy harvesting. Solar energy harvesting systems consist of solar arrays and signal processing circuitry.

Table 1.2: Power density comparison of ambient energy sources [22], [23].

Energy Source	Power Density
Solar	Outdoor: 15000 μW/cm^2 Indoor: 10 μW/cm^2
Vibration	Electrostatic: 50–100 μW/cm^2 Electromagnetic: 119 μW/cm^2 Piezoelectric: 250 μW/cm^3
Thermal	For 5°C gradient: 60 μW/cm^2

The photovoltaic effect generates electrical power on the solar cells, which is the direct conversion of incident light into electricity. The advantages of solar systems include their ease of incorporation, modularity, zero-emission or noise, no moving parts, and use of easily available source, i.e., sunlight. Disadvantages of solar systems consist of the additional signal processing circuitry essential to provide high-quality continuous current at a precise voltage, variability in quality and amount of power generation, and relatively large surface area needed for arrays of cells. Another disadvantage of solar systems is that it has low conversion efficiencies and higher cost, in addition to intermittent availability of sunlight.

1.2.2 Thermoelectric energy harvesting

Environments that naturally contain temperature gradients and heat flow have the potential to generate electrical power using thermal-to-electric energy conversion. The temperature difference provides the potential for efficient energy conversion, while heat flow provides the power, limited availability of heat limits the power produced. Nevertheless, thermoelectric energy harvesting has shown to be a viable technology for systems with exceptionally low-power requirements and promises to become more prevalent as the power requirements for such applications. An excellent example of thermoelectric energy harvesting is the thermoelectric wristwatch that converts body heat into electrical power that drives the watch [24].

The advantages of thermoelectric generators are that they are reliable, solid-state, and have long operation times with little noise and emissions. However, realization of power generating thermoelectric devices for very small sizes is limited due to the lack of large temperature gradients (>10 °C) in small device volumes (<1 cm^3) [25].

1.2.3 Vibration energy harvesting

Harvesting electrical energy from vibration deals with the conversion of mechanical energy into electrical energy. Energy harvesting devices based on vibration have power density values

comparable to other power sources such as thin- and thick-film lithium and lithium-ion batteries [25]. The vibration-based energy harvesting system is described in detail in the next section.

From Table 1.2, it is clear that outdoor solar energy has the highest power density, but indoor solar power density has a low value, and it does not apply to embedded applications where no or not enough light is available, in contrast, vibration power density has a relatively higher power density [22]. The use of vibration energy harvesting devices is an area of interest for wireless, self-powered microsystems, and macro-scaled devices. There are several opportunities for energy harvesting via vibration.

1.3 VIBRATION ENERGY HARVESTING

Vibration energy is a readily available source of energy. Random vibrations with different frequencies and amplitudes are freely available in the surroundings. Table 1.3 shows the various vibration sources and their typical vibration frequency and corresponding acceleration.

Table 1.3: Peak frequency and acceleration amplitude of various vibration sources [23].

Vibration source	**Peak frequency (Hz)**	**Acceleration amplitude (m/s^2)**
Clothes dryer	121	6.4
Microwave oven (small)	121	2.25
Second story floor of offices	100	0.2
Windows near a busy street	100	0.7
Washing machine	109	0.5
Refrigerator	240	0.1
Car instrument panel	13	3
Car engine compartment	200	12
Vehicles	5–2000	0.5–110

Table 1.3 shows that most of the vibration sources show a peak frequency around 100 Hz. But, some vibration sources show a relatively high peak frequency and much higher acceleration amplitude. Harvesting electrical energy from vibration deals with the conversion of mechanical energy into electrical energy, the process of converting mechanical energy into electrical energy is described by the energy flow diagram shown in Figure 1.1. When the mechanical input vibration energy overcomes the energy harvesting system's internal damping, the harvester's mass component starts to oscillate. This mechanical oscillation of the mass component is used to generate electrical energy through any electromechanical transduction mechanism.

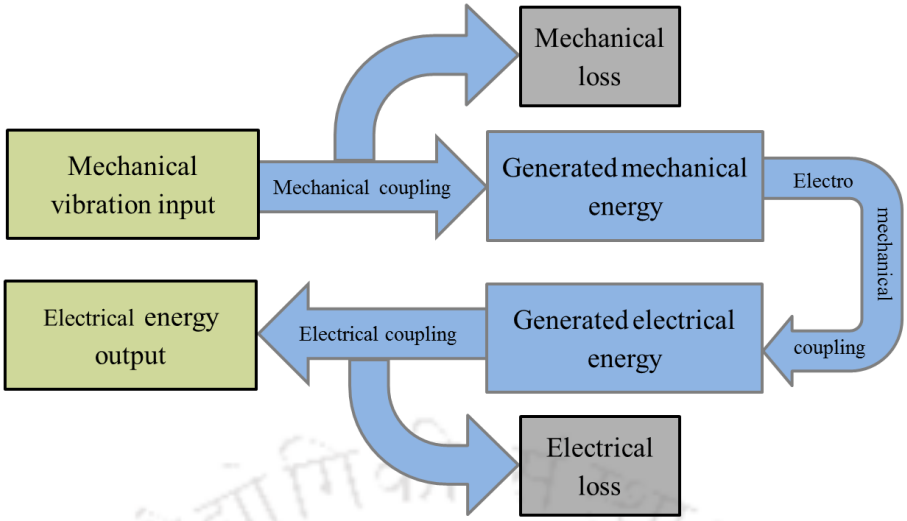

Figure 1.1: General model of the vibration energy harvester.

The electromechanical transaction of the vibration energy is generally carried out using electromagnetic conversion, electrostatic conversion, and piezoelectric conversion techniques.

1.3.1 Electromagnetic system

The basic physics behind the generation of electrical power from an electromagnetic generator is that when a changing magnetic field interacts with a closed-loop circuit, a current is induced in the loop, and if the loop is open-circuited, a voltage will be generated across the terminals of the circuit. The voltage generated for a micro-size generator is usually between 0.1 V and 0.2 V [25].

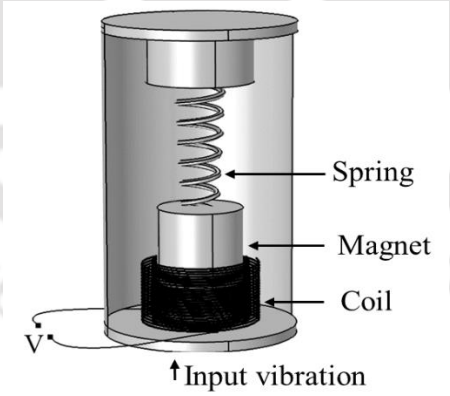

Figure 1.2: Typical electromagnetic energy harvester.

A typical vibration-based generator consists of an oscillating spring and mass system, as shown in Figure 1.2. The vibration of the base forces the magnetic mass to move relative to the stationary coil. As the magnetic flux through the coils changes, an alternating current/voltage is generated [26], [27].

1.3.2 Electrostatic system

Electrostatic energy generators consist of a variable capacitor whose capacitor plates are electrically isolated from each other by air, or vacuum, or an insulator [28]. When the system is exposed to the external mechanical vibrations, the gap between the plates will vary, causing a change in capacitance. In order to extract electrical energy from the vibrational input energy, the capacitor plates must be charged and the mechanical input vibrations work against the electrostatic forces present in the device. The main disadvantage of electrostatic energy harvesters is its requirement of an external energy source and normally, it has lower energy density [29], [30].

1.3.3 Piezoelectric system

In a piezoelectric vibration energy harvester (PVEH), energy transaction happens due to the piezoelectric effect. The PVEHs are attractive due to their high power density [31] and compatibility with microelectromechanical system (MEMS) fabrication technology [25]. The cantilever-based energy harvesters are preferred due to their ability to vibrate at low resonance frequency and high average stress on the surface for a given input condition [32]. Table 1.4 discusses the advantages and disadvantages of the above three types of vibration-based energy harvesters.

Table 1.4 Comparison of three types of vibration energy harvesters.

	Electromagnetic	**Electrostatic**	**Piezoelectric**
Advantages	• No voltage source required • High current output • Relatively high-power output • No need for smart material	• Small size • Easily integrated into micro-systems • Precise control of the mechanical resonance • No need for smart material	• No voltage source required • Higher output voltage • Small size • Simple structure • High efficiency • Compatible with MEMS
Disadvantages	• Complex design • Difficult to integrate into micro-system • Low output voltage	• Separate voltage source required • Higher operating frequency	• Limited material selection • Low output current • Brittleness

Considering the advantages of PVEH, we are motivated to work on PVEH, analyze the structures, improve geometry and yield. The following part of the chapter describes PVEH in detail.

1.4 PIEZOELECTRIC VIBRATION ENERGY HARVESTER (PVEH)

PVEH generates electrical energy from vibration using the piezoelectric effect. In this type of vibration energy harvester, a resonant structure is used, which oscillates when a suitable input vibration is applied to the structure. The most popular resonant structure is fixed-free cantilever-based structure [33]–[36], however, other types of structure, viz. piezoelectric stack [37], [38], diaphragm [39]–[41], and several other unconventional geometries [42]–[45] are also reported for energy harvesting applications.

1.4.1 Piezoelectric materials

The name piezoelectric is composed of two parts; piezo, which is derived from the Greek word for pressure, and electric from electricity. The rough translation is, therefore, the pressure-electric effect. In a piezoelectric material, the application of a force or stress results in the development of electric displacement in the material. This is known as the direct piezoelectric effect. Conversely, the application of an electric field to the same material will result in deformation or strain. This is known as the indirect or converse piezoelectric effect.

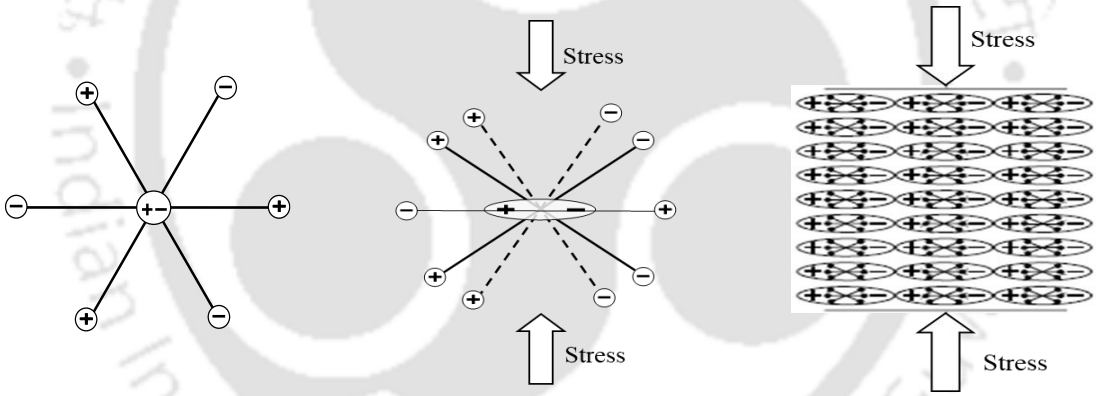

Figure 1.3: An example of (a) Molecular model of a piezoelectric material, (b) Molecular model under stress, (c) Polarizing effect on the bulk material.

When piezoelectric materials are subjected to external force, the material becomes polarized due to the external force the dimension of the piezoelectric material changes, and this change in dimension results in the variation in bond lengths between cations and anions. This phenomenon was discovered by Jacques and Pierre Curie brothers in 1880 and named as piezoelectricity or piezoelectric effect, which describes a relationship between stress and voltage. Conversely, a piezoelectric material will have a change in dimension when it is exposed to an electric field. This inverse mechanism is called electrostriction. The piezoelectric effect is observed in many crystals, for instance, tourmaline, topaz, quartz, Rochelle salt, and cane sugar.

Different types of piezoelectric materials are available such as single crystals (e.g., quartz SiO_2 and Rochelle salt), ceramics (e.g., Lead Zirconate Titanate or PZT, $BaTiO_3$ or BTO, and $LiNbO_3$), and polymers (e.g., polyvinylidene fluoride or PVDF). Table 1.5 shows the properties of different types of piezoelectric materials.

Table 1.5 Properties of some piezoelectric materials [46]–[49].

Constants	**Materials**				
	Quartz	**BTO**	**PZT**	**PVDF**	**ZnO**
d_{31} (10^{-12} C/N)	–0.93 (d_{12})	–79	–190 – –320	23	–5.12
d_{33} (10^{-12} C/N)	–2.3 (d_{11})	149	374 – 593	–33	12.3
$\varepsilon_{33}/\varepsilon_0$	4.4	1900	1800 – 3800	12 – 13	10.8 – 11
k_{31}	NA	0.21	0.32 – 0.44	0.12	0.181
k_{33}	0.07	0.48	0.70	0.15	0.466
T_c (°C)	573*	120	230 – 350	80 – 100	NA
g_{31} (10^{-3} Vm/N)	NA	5	–9.1 – –11.4	216	– 0.46
g_{33} (10^{-3} Vm/N)	– 58	14.1	20 – 25	330	1.11

From Table 1.5, we can see that PZT has the highest electromechanical coupling coefficient and the highest Curie temperature. Additionally, PZT can be poled easily and has a wide range of dielectric constants. The superior properties of PZT make it popular in the design of PVEH.

1.4.2 Piezoelectric constitutive equations

Piezoelectric constitutive equations describe mathematically how the piezoelectric material's stress (T), strain (S), charge-density displacement (D), and electric field (E) interact with each other. The constitutive equations are the combination of mechanical and electrical equations. A mechanical constitutive equation describes how a material deforms on the application of stress or vice-versa, and an electrical constitutive equation describes how charge moves in a dielectric material on the application of voltage or vice versa. The piezoelectric constitutive equations combine both the electrical and mechanical equations to describe the coupling between the electrical and mechanical properties of the material.

The linear form of the piezoelectric constitutive equation in Strain-Charge form can be written as per IEEE Standard on Piezoelectricity [50] as.

$$S = s^E T + dE \tag{1.1}$$

$$D = dT - \varepsilon^T E \tag{1.2}$$

where S is the six-dimensional strain vector, T is the vector of stresses, s^E is six by six compliance matrix evaluated at constant electric field, d is the three by six matrix of piezoelectric strain coefficients, E is the electric field vector, D is the three-dimensional electric displacement vector, and ε^T is the three by three dielectric constant matrix evaluated at constant stress.

The piezoelectric constitutive equations can be written in matrix form as [51]

$$\begin{Bmatrix} S_1 \\ S_2 \\ S_3 \\ S_4 \\ S_5 \\ S_6 \end{Bmatrix} = \begin{pmatrix} s_{11} & s_{12} & s_{13} & s_{14} & s_{15} & s_{16} \\ s_{21} & s_{22} & s_{23} & s_{24} & s_{25} & s_{26} \\ s_{31} & s_{32} & s_{33} & s_{34} & s_{35} & s_{36} \\ s_{41} & s_{42} & s_{43} & s_{44} & s_{45} & s_{46} \\ s_{51} & s_{52} & s_{53} & s_{54} & s_{55} & s_{56} \\ s_{61} & s_{62} & s_{63} & s_{64} & s_{65} & s_{66} \end{pmatrix} \begin{Bmatrix} T_1 \\ T_2 \\ T_3 \\ T_4 \\ T_5 \\ T_6 \end{Bmatrix} + \begin{pmatrix} d_{11} & d_{21} & d_{31} \\ d_{12} & d_{22} & d_{32} \\ d_{13} & d_{23} & d_{33} \\ d_{14} & d_{24} & d_{34} \\ d_{15} & d_{25} & d_{35} \\ d_{16} & d_{26} & d_{36} \end{pmatrix} \begin{Bmatrix} E_1 \\ E_2 \\ E_3 \end{Bmatrix} \tag{1.3}$$

and

$$\begin{Bmatrix} D_1 \\ D_2 \\ D_3 \end{Bmatrix} = \begin{pmatrix} d_{11} & d_{12} & d_{13} & d_{14} & d_{15} & d_{16} \\ d_{21} & d_{22} & d_{23} & d_{24} & d_{25} & d_{26} \\ d_{31} & d_{32} & d_{33} & d_{34} & d_{35} & d_{36} \end{pmatrix} \begin{Bmatrix} T_1 \\ T_2 \\ T_3 \\ T_4 \\ T_5 \\ T_6 \end{Bmatrix} + \begin{pmatrix} \varepsilon_{11} & \varepsilon_{12} & \varepsilon_{13} \\ \varepsilon_{21} & \varepsilon_{22} & \varepsilon_{23} \\ \varepsilon_{31} & \varepsilon_{32} & \varepsilon_{33} \end{pmatrix} \begin{Bmatrix} E_1 \\ E_2 \\ E_3 \end{Bmatrix} \tag{1.4}$$

Piezoelectric materials are transversely isotropic and it is commonly assumed that the direction-3 is along the polarization direction, which also coincides with the axis of transverse isotropy. Hence the above two equations can be rearranged considering the transversely isotropic nature of the material as [51]

$$\begin{Bmatrix} S_1 \\ S_2 \\ S_3 \\ S_4 \\ S_5 \\ S_6 \end{Bmatrix} = \begin{pmatrix} s_{11} & s_{12} & s_{13} & 0 & 0 & 0 \\ s_{12} & s_{11} & s_{13} & 0 & 0 & 0 \\ s_{13} & s_{13} & s_{33} & 0 & 0 & 0 \\ 0 & 0 & 0 & s_{44} & 0 & 0 \\ 0 & 0 & 0 & 0 & s_{44} & 0 \\ 0 & 0 & 0 & 0 & 0 & 2(s_{11} - s_{12}) \end{pmatrix} \begin{Bmatrix} T_1 \\ T_2 \\ T_3 \\ T_4 \\ T_5 \\ T_6 \end{Bmatrix} + \begin{pmatrix} 0 & 0 & d_{31} \\ 0 & 0 & d_{31} \\ 0 & 0 & d_{33} \\ 0 & d_{15} & 0 \\ d_{15} & 0 & 0 \\ 0 & 0 & 0 \end{pmatrix} \begin{Bmatrix} E_1 \\ E_2 \\ E_3 \end{Bmatrix} \tag{1.5}$$

and

$$\begin{Bmatrix} D_1 \\ D_2 \\ D_3 \end{Bmatrix} = \begin{pmatrix} 0 & 0 & 0 & 0 & d_{15} & 0 \\ 0 & 0 & 0 & d_{15} & 0 & 0 \\ d_{31} & d_{31} & d_{33} & 0 & 0 & 0 \end{pmatrix} \begin{Bmatrix} T_1 \\ T_2 \\ T_3 \\ T_4 \\ T_5 \\ T_6 \end{Bmatrix} + \begin{pmatrix} \varepsilon_{11} & 0 & 0 \\ 0 & \varepsilon_{11} & 0 \\ 0 & 0 & \varepsilon_{33} \end{pmatrix} \begin{Bmatrix} E_1 \\ E_2 \\ E_3 \end{Bmatrix} \tag{1.6}$$

The above two equations show that for transversely isotropic piezo-ceramics, there are five elastic constants (s_{11}, s_{12}, s_{13}, s_{33}, s_{44}), three piezoelectric strain constants (d_{31}, d_{33}, d_{15}) and two dielectric or permittivity constants (ε_{11}, ε_{33}). The above constitutive equation can be expanded as

$$\begin{aligned} S_1 &= s_{11}T_1 + s_{12}T_2 + s_{13}T_3 + d_{31}E_3 \\ S_2 &= s_{12}T_1 + s_{11}T_2 + s_{13}T_3 + d_{31}E_3 \\ S_3 &= s_{13}T_1 + s_{13}T_2 + s_{33}T_3 + d_{33}E_3 \\ S_4 &= s_{44}T_4 + d_{15}E_2 \\ S_5 &= s_{44}T_5 + d_{15}E_1 \\ S_6 &= 2(s_{11} - s_{12})T_6 \end{aligned} \tag{1.7}$$

and

$$\begin{aligned} D_1 &= d_{15}T_5 + \varepsilon_{11}E_1 \\ D_2 &= d_{15}T_4 + \varepsilon_{11}E_2 \\ D_3 &= d_{31}T_1 + d_{31}T_2 + d_{33}T_3 + \varepsilon_{33}E_3 \end{aligned} \tag{1.8}$$

The relationship between strain and charge for a piezoelectric material can be found in the above two sets of equations.

1.5 CANTILEVER-BASED PVEH

Considering the cantilever beam as shown in Figure 1.4, the top and bottom surfaces are covered with electrodes, and the cantilever can vibrate only in *z*-direction that is along the direction-3, the strain due to vibration will only be along direction-1 and the electric displacement will only be in direction-3. Thus, the stresses T_2, T_3, T_4, T_5, and T_6 will be zero and electric displacements D_1 and D_2 will be zero, then the piezoelectric strain charge constitutive equation can be written as [25]

$$S_1 = s_{11}^E T_1 + d_{31}E_3 \tag{1.9}$$

$$D_3 = d_{31}T_1 + \varepsilon_{33}^T E_3 \tag{1.10}$$

The equation (1.9) relates to the converse piezoelectric effect. It shows that a strain will result from an applied electric field in the material. The direct piezoelectric effect is described in equation (1.10) and shows that a charge density field will result from applied stress.

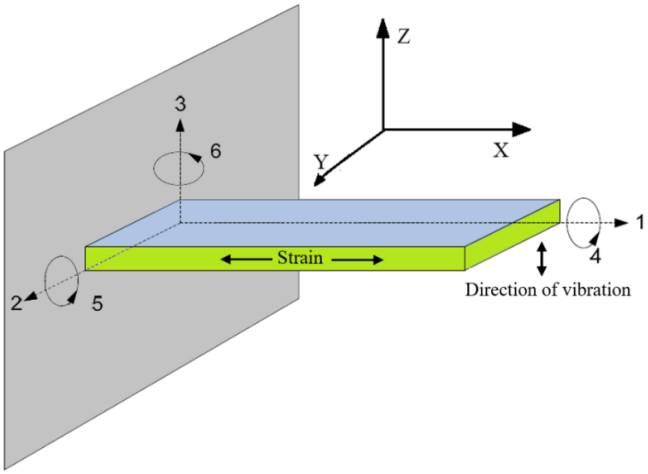

Figure 1.4: Piezoelectric cantilever beam.

1.5.1 Types of cantilever-based PVEH

Piezoelectric vibration energy harvester consists of one or more piezoelectric layers and substrate. Depending upon the number of layers, PVEH can be classified as unimorph [52], [53] energy harvester, and multicopy [54] energy harvester. A unimorph energy harvester is where only one piezoelectric layer is used whereas, in a multimorph energy harvester, more than one piezoelectric layer is used. The majority of the multimorph energy harvesters are bimorph, where piezoelectric layers are used on both sides of a metal substrate. Figure 1.5 shows types of layers (a), a unimorph (b), bimorph in series connection (c), and bimorph in parallel connection (d).

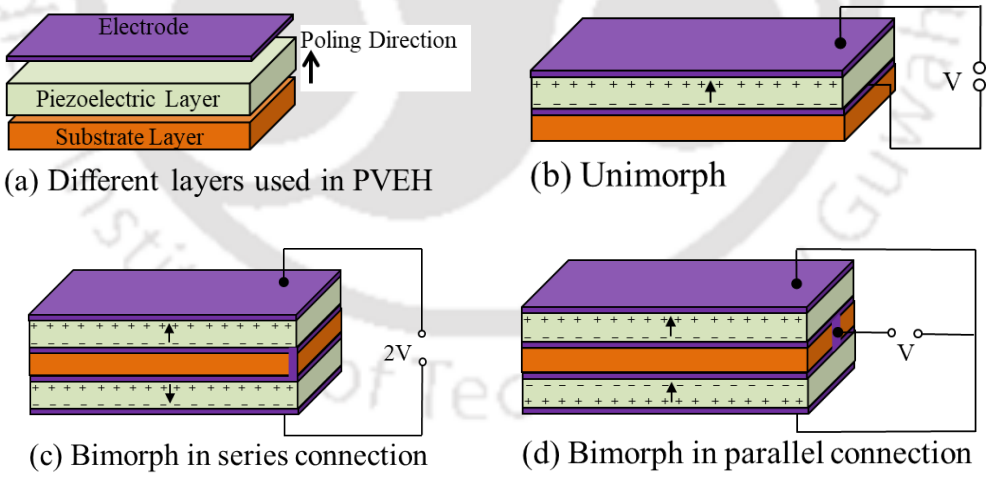

Figure 1.5: Different configurations of piezoelectric and substrate layers.

In the bimorph cantilever configuration, the two piezoelectric layers can be wired in series connection or in parallel connection. In a parallel connection, the two piezoelectric layers are polarized in the same direction, and the outer electrodes are joined together to work as a single terminal. The other terminal is taken by shorting both sides of the substrate layer, as shown in Figure 1.5 (d). In this configuration, the same amount of charge occurs on each outer electrode.

When the structure is subjected to stress, in parallel connection, the individual currents add up and produce larger currents. In a series connection, the two piezoelectric layers are oppositely polarized and the charges generated on the outer electrodes of both the piezoelectric layers are opposite in nature. External load is connected between the metal substrate and outer electrodes of both the piezoelectric layers, as shown in Figure 1.5 (c). In this configuration, the individual voltages of the two piezoelectric layers are added up and produce a higher output voltage.

1.6 DIAPHRAGM-BASED PVEH

PVEH using circular diaphragms with a solid structure at the center featuring as a proof mass has drawn much attention in recent years [55]–[58]. A diaphragm-based PVEH operates in a similar manner to that of a cantilever-based PVEH. The piezoelectric circular diaphragm is constructed by attaching a thin circular piezoelectric disc to a metallic shim. A diaphragm structure is normally clamped on the outer edge, and a proof mass is placed at the center of the disc [59]–[61], as shown in Figure 1.6. The diaphragm-based PVEH can be operated as resonance structure [58], [62], or impact-based structure [63]. Diaphragm-based PVEH are also used as self-powered pressure sensors [64] and walking energy harvesters [65]. The detailed analysis of diaphragm-based PVEH is presented in chapter 7.

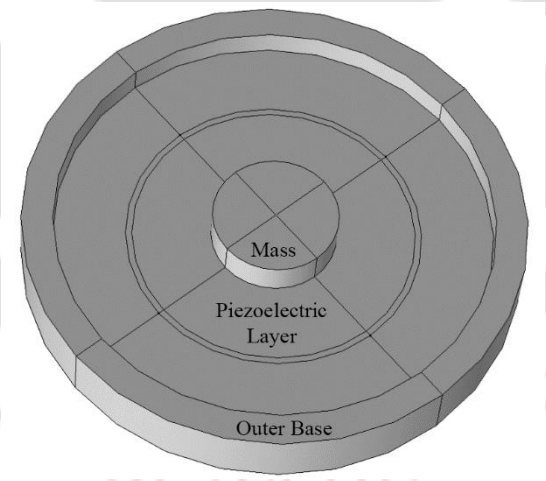

Figure 1.6: Diaphragm-based PVEH.

1.7 NONLINEAR PVEH

A linear energy harvester generates highest power when the energy harvester is excited with the natural frequency of vibration, as the frequency of vibration deviates from the resonance frequency of the energy harvesting system the output power falls sharply from its peak. Sometimes the source vibration frequency is not constant and varies randomly with time, in this scenario a nonlinear energy harvester can be used. In a nonlinear energy harvester, the spring

constant of the vibrating mechanism is a nonlinear parameter and the nonlinearity is normally introduced by modifying the structural design [66]. A nonlinear energy harvester can be a monostable or a multi-stable structure [67]. The nonlinear PVEHs are generally used when the vibration source is of random frequency [68]–[70] but a linear energy harvester generates more power when the source frequency is of a narrow bandwidth and matches with the resonance frequency of the energy harvester. The scope of the thesis is limited to the geometry optimization of linear PVEH to achieve uniform stress on the piezoelectric material.

1.8 LITERATURE REVIEW OF PVEH

The research objective is to modify the conventional PVEH to increase the power density. Therefore, a detailed literature survey is carried out for conventional PVEH based on cantilever and diaphragm and various modifications to achieve higher power density.

1.8.1 Literature survey on cantilever-based PVEH

The first vibration-based micro-generator was analyzed by William and Yates [71] in 1995. They developed an analytical model for the generator using a spring-mass-damper system. The proposed micro-generator had a volume of 25 mm^3, and the electrical power output was 0.1 mW and 1.0 μW, respectively, for 330 Hz and 70 Hz operating frequency.

Beeby et al. [72] in 1999 studied the microelectromechanical fabrication technology to fabricate a PZT-based vibration energy harvester on a silicon substrate. They recommended the plasma etching process over wet etching of silicon wafer for better bonding of PZT with silicon.

Jones et al. [73] in 2001 developed a cantilever-based PVEH and used steel as a substrate and PZT as a piezoelectric material. The substrate and the piezoelectric layer had a thickness of 100 μm and 70 μm, respectively. Experimental results showed that the energy harvester had a resonance frequency of 80.1 Hz and a maximum output electrical power of 2.1 μW.

Roundy and Wright [74] in 2004 derived an analytical model for a cantilever-based bimorph PVEH. They used brass as a substrate material and PZT-5H as the piezoelectric material. Their theoretical analysis was verified with experimental results. The 1 cm^3 sized device generated 375 μW of electrical power for an acceleration of 2.5 m/s^2 at 120 Hz frequency.

Shahruz [75] in 2006 designed an array of cantilever-based PVEH, each with different dimensions. The research suggested that an array of cantilevers with varying resonance frequencies could work as a mechanical bandpass filter and could be used to harvest vibration energy for a wide range of frequencies.

Fang et al. [76] in 2006 fabricated a unimorph PVEH using MEMS fabrication technology. In this work, a PZT layer of thickness 1.64 μm was used with Ti/Pt electrodes. The device showed a resonance frequency of 609 Hz and generated 2.16 μW of power across a load resistance of 21.4 kΩ.

Yuantai et al. [77] in 2007 designed a bimorph PVEH with axial preload to adjust the resonance frequency of the system. Analytical expressions were derived for the system and results showed that axial preload could change the device resonance frequency from 58 Hz to 169 Hz.

Huan Xue et al. [78] in 2008 designed multiple piezoelectric bimorphs of different aspect ratios to be used as a broadband PVEH. They revealed that the operating frequency band of the energy harvester could be shifted towards the ambient vibration frequency range by changing the number of piezoelectric bimorphs connected in a parallel connection.

Erturk and Inman [79] in 2008 derived a distributed parameter model for PVEH, and this model was able to estimate harvested power from all the modes of vibration. They also discussed the issues with different mathematical modeling of PVEH [80] and proposed a correction factor for the lumped parameter-based model in [81]. The correction factor presented in this article was essential for PVEH with a lower ratio of end-mass to beam mass and for PVEH without any end-mass.

Lee et al. [82] in 2009 fabricated PZT-based PVEH on silicon-based cantilever using aerosol deposition method. The piezoelectric cantilever was designed to operate in {3-1} mode and {3-3} mode. The {3-1} mode of operation produced an output power of 2.765 μW at 255.9 Hz frequency for an acceleration of 2.5*g* while the {3-3} mode of operation produced an output power of 1.288 μW at 214 Hz frequency for an acceleration of 2.0*g*.

Elvin and Elvin [83] in 2009 developed an equivalent circuit model for an unimorph PVEH generator. The derived model was validated with the published analytical solutions given in [79].

Erturk and Inman [84] in 2009 developed a distributed parameter model for a piezoelectric bimorph. The model was used to estimate power generated from series and parallel connected bimorphs, and the results were compared with the experimental results from an identical PVEH. The energy harvester generates 23.9 mW of power at 45.6 Hz resonance frequency across an optimal load resistance of 35 kΩ.

Durou et al. [85] in 2010, developed a cantilever-based PVEH of resonance frequency 76 Hz. The energy harvester was excited with an acceleration of 0.2*g*, and the generated peak power was 13.9 μW.

Park et al. [86] in 2010 fabricated a d_{33} mode PVEH with sol-gel spin-coating method. The peak power generated from this device was reported as 1.1 μW for an input acceleration of 0.39*g* at 528 Hz frequency.

Zhu et al. [87] in 2010 studied different design strategies for PVEH using coupled piezoelectric-circuit FE method. They suggested three design strategies to harvest maximum power from vibration and claimed that their strategy would increase the power density from 200 μW/cm^3 to around 1 to 2 mW/cm^3.

Challa et al. [88] in 2011 developed a self-tuning PVEH using magnetic stiffness technique. Their device can tune its resonance frequency from -27% to 22% of the untuned resonance frequency. However, the tuning mechanism consumes enormous energy, and the energy harvester needs 88 min to generate that energy.

Xu et al. [89] in 2012 reported a piezoelectric bimorph-based energy harvester with silicon end-mass. They have noticed an increase in coupling coefficient due to two piezoelectric layers and claimed to have generated 37.1 μW power for 1*g* acceleration.

Ahmad et al. [90] in 2012 developed a cantilever-based PVEH to harvest electrical energy from rain droplets. The cantilever consisted of five layers of PZT and had a resonance frequency of 315.15 Hz. They reported 400 μJ of harvested energy for 230 drops per second rainfall.

Zhao and Erturk [91] in 2013 presented electrostatic modeling of piezoelectric bimorph energy harvester for random broadband vibrations. They verified their mathematical results by comparing them with experimental results.

Alsuwaiyan et al. [92] in 2014 presented PVEH from a multi-frequency vibration source using three cantilevers of resonance frequencies 40 Hz, 45 Hz, and 53.4 Hz. The reported peak power was 440 μW at around 40 Hz frequency.

Yaowen Yang et al. [93] in 2015 proposed a PVEH geometry to harvest electricity from two-dimensional vibration. The proposed geometry was able to generate energy with base excitation from any direction in the horizontal and vertical plane. The peak harvested power was 2.9 mW for input vibration at 60^o, and the lowest was 1.8 mW for input vibration at 15^o to the horizontal direction.

Emamian et al. [94] in 2016 developed a PVEH using screen printing technique. The PVEH was a unimorph with a 12.5 μm polarized PVDF layer sandwiched between Metglas electrodes. They

reported that the device could generate 0.28 μW of power across a 1 MΩ load resistance at 54 Hz frequency. The power density was reported as 11.67 $\mu W/cm^3$.

Baishya et al. [95] in 2017 proposed a correction factor for lumped parameter model of cantilever-based PVEH. The model was able to predict resonance frequency and output power accurately and was verified with published experimental results.

Zhang et al. [96] in 2017 proposed a rotational piezoelectric energy harvester to harvest wind energy. In their design, a PVDF beam generated electricity using impact-induced vibration. The reported peak power was 2566.4 μW for a wind speed of 14 m/s.

Yang et al. [97] in 2017 analyzed the efficiency of cantilever-based PVEH systems using theoretical and experimental studies. They reported that the efficiency decreased with the increase in excitation frequency. They also noted that at resonance, the phase difference was 90^o between excitation and response, and the PVEH showed the highest efficiency.

Palosaari et al. [98] in 2018 investigated the effect of substrate layer thickness on bimorph PVEH. They used four different substrate configurations and claimed that the thinner substrate layer showed higher efficiency.

Khalili et al. [99] in 2019 developed a PVEH system to harvest mechanical energy from roadways and derived an electromechanical model to characterize it. The energy harvester was exposed to dynamic loading of 1.1 kN and 11 kN at 66 Hz frequency, and the voltage output was reported as 95 V and 1190 V respectively across a 500 kΩ load resistance.

Pradeesh and Udhayakumar [100] in 2019 studied the effect of piezoelectric material and end-mass placement on the PVEH performance and reported that the piezoelectric material should be placed near the fixed end to generate maximum power, and the end-mass shape had a negligible effect on the harvested energy.

Asthana & Khanna [101] in 2020 designed a bimorph PVEH and derived an analytical model based on Euler-Bernoulli beam theory. They estimated the harvested power as 1.31 mW at 90 Hz frequency for 1*g* input acceleration.

Taemin et al. [102] in 2020 designed a wideband PVEH based on an array of four cantilevers with resonance frequencies 111 Hz, 117 Hz, 123 Hz, and 129 Hz. In the second part of the paper, the four cantilevers were merged together to form a single-substrate PVEH, and the performances were compared. It was reported that the PVEH array was able to produce 105.5 mW of power at

1.5*g* acceleration, while the single-substrate PVEH was able to generate 321 mW of power at the same acceleration.

Jeong et al. [103] in 2021, proposed a smartpen PVEH that can generate electrical energy during writing. The energy harvester was able to store 3.1 μJ of energy in a capacitor from 10 seconds of writing.

1.8.2 Literature survey on diaphragm-based PVEH

Kim et al. [104] in 2004 developed an energy harvester using cymbal transducer having a ceramic disc. The diameter and thickness of the disk were respectively 29 mm and 1 mm. The reported generated power was 39 mW for 7.8 N of dynamic force at 100 Hz frequency.

Mo et al. [41], [105] in 2010 designed an unimorph circular diaphragm-based PVEH with smaller radius of the piezoelectric layer than the substrate layer. They derived an analytical expression for the proposed diaphragm-based PVEH and later, they used experimental results to validate the analytical results. It was shown that the strain and deflection due to load and bending were the limiting factors in the design process.

Chen et al. [62] in 2012 demonstrated a circular diaphragm-based PVEH, and they used a pre-stressed diaphragm at 1*g* acceleration. The reported harvested power was 12 mW at 113 Hz frequency across a 33 kΩ load resistor.

Deterre et al. [106] in 2012 developed a diaphragm-based PVEH to harvest electrical energy from fluid pressure. Their ultimate goal was to generate electric energy to power active implantable medical devices. A fluid pressure of 0 to 50 mmHg is applied at 2 Hz frequency to the diaphragm as mechanical input energy. They also proposed an active energy harvesting method to increase energy extraction efficiency from piezoelectric material.

Mohammadi and Abdalbeigi [107] in 2013 derived an analytical model for simply supported and clamped supported diaphragm-based PVEH. Their parametrical study found an optimal value for the thickness and radius of unimorph piezoelectric layer.

Xiao et al. [58] in 2014 reported a broadband PVEH using four similar circular diaphragms with varying tip-masses. They reported that the four diaphragms showed resonance frequency in the range of 120 Hz to 225 Hz and generated 5.14 mW, 6.65 mW, 9.7 mW, and 10 mW of power for an input acceleration of 1*g*.

Wang et al. [108] in 2014 developed a broadband PVEH using circular diaphragm array. The array was comprised of three diaphragms in parallel connection and was able to generate 21.4 mW power across an optimal load resistance of 11 kΩ at 1*g* acceleration.

Dong et al. [109] in 2015 studied the relation between piezoelectric material properties performance of diaphragm-based PVEH. They recommended piezoelectric material with a higher d_{33} coefficient and a lower dielectric coefficient for higher harvested power.

Yang et al. [60] in 2017 developed a PVEH using circular diaphragm structure and applied a pre-stress of 0.3 N. They optimized the structural parameters to obtain maximum output power and lower resonance frequency. It was reported that the optimized structure was able to harvest 16.3 mW power at 219 Hz frequency.

Shu et al. [110] in 2018 developed a diaphragm-based PVEH, they had applied input acceleration at the center of the diaphragm and the outer edge was allowed to vibrate freely. They reported 20.8 mW of generated power for 1*g* acceleration at 237 Hz frequency.

Xu et al. [111] in 2020 developed a diaphragm-based PVEH and discussed the non-uniform strain distribution on the disk. The designed PVEH with 19 mm diameter was able to harvest 8.34 mW of power for 1g acceleration.

Mehdipour and Honarvar [112] in 2021, derived an analytical model for unimorph diaphragm-based PVEH. They studied the effect of different parameters on the zero-strain point of the PVEH disk and found that the radii of the disk control the position of the zero-strain point. They also reported that optimized performance is observed inside the radius of the zero-strain boundary.

Yuan et al. [57] in 2021 developed an acoustic energy harvester using piezoelectric diaphragm-based geometry. Their experimental results showed that the energy harvester could generate 8.452 µW of power from urban railway noise.

1.9 FABRICATION METHODS

The cantilever-based PVEH structure usually consists of a substrate layer, one or more piezoelectric layers and an end-mass attached to the free end of the cantilever. The substrate layer typically works as a mechanical support for the piezoelectric layers and the end-mass. The materials used for the substrate layers are primarily stainless steel, brass, aluminum, or micromachined silicon, depending on the fabrication processes and the physical size [113], [114]. Though many piezoelectric materials are available, Lead Zirconate Titanate (PZT) is the most commonly used piezoelectric material for PVEH fabrication [115] because of its high

piezoelectric coefficients and easy availability. Other piezoelectric materials used for PVEH are ZnO nanowires, Barium Titanate, PVDF, Aluminum Nitride [116], [117] etc. In this study, PZT is considered as the piezoelectric material because of its high electromechanical coupling coefficient, and brass is considered as the substrate material as all the studied devices are macro-sized.

PZT films can be deposited on a substrate using sputtering, chemical vapor deposition (CVD), Sol-gel process, metal-organic decomposition (MOD), and chemical solution deposition (CSD) techniques [116]. These fabrication processes can produce piezoelectric thin films on a silicon substrate. However, for thick film deposition, screen-printing methods are used [89]. When the PVEH geometry is of larger size, readymade piezoelectric patches (readily available in the market) are used. In this process, the piezoelectric patches are generally glued to the substrate layer with a suitable adhesive [118], [119].

1.10 STRESS DISTRIBUTION ON THE CONVENTIONAL PVEH

The literature on cantilever-based PVEH suggests that the fixed-free geometry is the most popular choice to design PVEH. The conventional cantilever-based energy harvesters consist of rectangular beams of uniform cross-section area with one or more piezoelectric layers. The main advantage of choosing a cantilever-based structure is its strain generating capability and low resonance frequency of vibration. Though the cantilever with a uniform cross-section area is preferred for PVEH, the stress distribution on the conventional PVEH is highly non-uniform [120], [121]. A fixed-free cantilever-based PVEH exhibits considerable stress on the fixed end and very low stress on the free end of the beam. Thus, the piezoelectric material at the free end generates much lower electrical energy and remains underutilized.

1.11 STRATEGIES TO SOLVE STRESS NON-UNIFORMITY

The stress non-uniformity in conventional cantilever-based PVEH reduces the average stress on the piezoelectric material, and as a result, the harvested power density decreases. Several research groups have proposed geometrical modifications to achieve uniformity in stress along the length of the energy harvester beam.

Roundy et al. [32] in 2005 proposed that tapering the width of a cantilever beam would increase the average strain on the piezoelectric material and improve the harvested electrical energy.

Baker et al. [122] in 2005 used two width-tapered beams, one trapezoidal and the other triangular beam. They reported that the trapezoidal beam showed a 30% improvement in the generated power density while the triangular beam showed a 50% increase in the generated power density.

Mehraeen et al. [123] in 2010 designed a cantilever-based PVEH with tapered thickness. The thickness-tapered bimorph was made by varying the substrate thickness, and they reported that tapering the substrate thickness led to additional harvested power and a more uniform stress profile.

Ben Ayed et al. [124] in 2014 investigated linear and quadratic shaped cantilever structures for unimorph PVEH. They reported a change in resonance frequency and mode shape for change in the beam shape. They also reported that the quadratic shape beam yielded double electrical energy than the rectangular-shaped cantilever beam.

Muthalif and Nordin [125] in 2015 designed a triangular-shaped PVEH and compared its performance with a rectangular-shaped beam. They reported that the triangular-shaped cantilever beam produced double average strain along the length than a rectangular cantilever beam and showed that the triangular-shaped PVEH generated more voltage across resistive load compared to rectangular-shaped PVEH.

Sriramdas et al. [126] in 2015 modified a bimorph PVEH to have a multistep thickness profile of piezoelectric layers and reported reduction in resonance frequency and 90% increase in harvested power for the same input acceleration.

Hosseini and Nouri [127] in 2016 studied rectangular, triangular, and trapezoidal beams for PVEH application and strain distribution. They reported that the triangular beam generated more strain and voltage than the other two.

X D Xie et al. [128] in 2017 studied rectangular, trapezoidal, and triangular beams for PVEH design and found that triangular beam showed the best strain distribution among the three. They also reported that the triangular beam showed an enhanced electromechanical coupling coefficient and less stress value.

H. Salmani et al. [129] in 2018 developed a PVEH based on an exponentially tapered-width cantilever. They carried out width tapering for various beams of different lengths and observed that tapering led to a higher voltage for all the beam lengths.

Alireza Keshmiri and Nan Wu [130] in 2018 presented an analytical approach to a wideband PVEH using thickness-tapered cantilever arrays. They showed that an array of nonlinearly tapered piezoelectric cantilevers could be used to generate higher voltage over a wide frequency range.

Srinivasulu Raju et al. [131] in 2019 designed a width-tapered PVEH with a rectangular cavity and reported that their design generated 157.8% higher voltage than PVEH having a uniform cantilever beam.

Pradeesh and Udhayakumar [132] in 2019 compared several geometrical designs for PVEH applications and reported that inverted tapering of width and thickness generates 47.39% more electrical power than a conventional rectangular cantilever-based energy harvester.

Chaudhury et al. [133] in 2019 analyzed four different geometries of PVEH, the modeling and analysis were carried out using FEM software. They reported that the width-tapered perforated structure showed an output voltage of around 8.5 volts which was 97% higher than the rectangular structure.

Biao Wang et al. [121] in 2020 developed a linearly varying thickness-tapered PVEH, and the PVEH was based on the Garolite FR-4 epoxy laminate. They reported a 78% increase in energy conversion efficiency for the thickness-tapered beam compared to conventional PVEH with uniform thickness.

D. S. Ibrahim et al. [134] in 2020 has done a comparative study between a width-tapered and a thickness-tapered beam for PVEH application. They derived expressions for the strain on both the beams and concluded that the thickness-tapered beam showed an 18% decrease in resonance frequency and a 6.4% increase in power compared to the width-tapered beam.

In summary, literature clearly indicates that the most suitable option to obtain higher power is by using variable cross-section beam such that the stress profile is more uniform. There are two major options in variable cross-section design, one is width-tapered and the other is thickness-tapered beam. Both the geometrical modifications have their own merits and demerits. A width-tapered beam is much easier to fabricate while a thickness-tapered beam occupies less volume. A comparison between width-tapered and thickness-tapered piezoelectric vibration energy harvesters (PVEH) revealed that the thickness-tapered PVEH produces a higher power output compared to the width-tapered PVEH [134]. Width-tapered PVEH are well examined and width-tapered PVEH having uniform stress distribution are reported, however thickness-tapered PVEH having uniform stress distribution has not been reported.

1.12 RESEARCH GAP

It is clear from the above literature that the more uniform the distribution of stress on the piezoelectric material, the more is the harvested power. Uniform stress distribution on a cantilever-based PVEH increases the average stress on piezoelectric material and thus generates

higher power. A uniform stress distribution will also increase the device's reliability in terms of mechanical failure. Therefore, a suitable cantilever geometry which can produce uniform stress along the beam length is most desired for vibration-based energy harvesters. The uniformity in stress will ensure that the piezoelectric material contributes equally to the electrical energy generation process. The increase in average stress on the beam should increase the overall power density of the energy harvester.

The above literature also implies that the majority of the research groups have two geometrical modifications to achieve uniform stress distribution. The first approach is by modifying the width of the cantilever-based structure and the second approach is by modifying the thickness of the cantilever-based structure.

In literature, most of the reported geometry modifications to reduce stress non-uniformity is by width tapering of the cantilever, which results in a trapezoidal-shape or a triangular-shape PVEH. In trapezoidal-shape PVEH, the stress distribution improves to some extent, but it's not perfectly uniform. In the triangular-shape PVEH, the stress is uniform. However, the surface area to attach piezoelectric material reduces significantly due to the narrow width at the free end. Some research groups have modified the thickness profile to achieve improved stress distribution by tapering the thickness in linear or exponential outline and reported better stress uniformity. A comparative study between width-tapered and thickness-tapered PVEH suggested that the thickness-tapered PVEH generates more power than the width-tapered PVEH. However, an optimal thickness-tapered geometry for uniform stress distribution and its analytical model for thickness-tapered PVEH has not been reported and needs more research.

1.13 OBJECTIVE OF THE THESIS

Considering the present research gaps mentioned above, the main objectives of this thesis are as follows.

- To study necessary modifications required in the thickness profile for perfectly uniform stress on cantilever-based PVEH.
- Reduction in peak stress value on the PVEH system for better device reliability.
- Design of PVEHs with higher electrical power density utilizing cantilevers of constant stress.
- Development of analytical expressions to analyze the proposed PVEHs.
- Exploring other geometrical modifications to increase PVEH power density.

1.14 THESIS CONTRIBUTION

The thesis aims to improve the electrical power generation capability of PVEH by modifying the geometry. For each proposed geometry, improved harvested power, power density, peak stress, and stress profile of the PVEH are estimated and compared with equivalent conventional PVEH geometries. The main contributions of the thesis are as follows.

- The thickness profile of bimorph cantilever-based conventional PVEH is modified to achieve uniform stress along the beam length. Two new thickness-tapered geometries are proposed. The first geometry, PVEH-1, consists of a substrate of tapered thickness profile and piezoelectric layers of uniform thickness. The desired thickness profile for uniform stress distribution is derived analytically. The uniform stress profile ensures a lower value of peak stress and increased average stress in the beam leading to high power density. The performance of PVEH-1 is compared with equivalent conventional PVEH having a uniform thickness.
- The second proposed geometry, PVEH-2, consists of a bimorph cantilever with a substrate of uniform thickness and piezoelectric layers of tapered thickness profile. Analytical expressions are derived for end-mass displacement, generated voltage, resonance frequency, and stress profile on the piezoelectric material. FE analysis of the PVEH is carried out, and the results are verified with the solutions from the analytical expressions. The generated power and stress distribution of the proposed energy harvester are compared with equivalent conventional PVEH of uniform thickness.
- The conventional diaphragm-based PVEH is modified by introducing radial cuts in the diaphragm. FE analysis is carried out to find resonance frequency, end-mass displacement, and generated power. The diaphragm is further divided into several identical sectors, and the changes in resonance frequency and electrical power density are studied. The sectored diaphragm-based PVEH is further analyzed to design a wideband energy harvester.

1.15 SCOPE OF THE THESIS

In this thesis, issues with conventional PVEH are studied, and geometrical modification is proposed to improve electrical energy output and increase device reliability. The scope of the thesis is limited to the following analyses

- FE modeling and analysis of conventional cantilever-based PVEH to study resonance frequency, displacement, stress profile, generated electrical power across a resistive load.

Validation of FE analysis results by comparing with published experimental and analytical results.

- The thesis covers proposals to improve stress distribution on the conventional cantilever-based PVEH by modifying thickness profile, derivation of analytical expressions for the proposed thickness modified PVEHs to estimate various outputs, and finally verification of analytical results with FE analysis.
- The thesis includes proposals to improve the power density of diaphragm-based PVEH by introducing radial cuts in the diaphragm and verification using FE analysis.
- In this study, it is considered that the input frequency varies around the fundamental resonance frequency of the energy harvesting device. Normally the frequency of the second-order mode is approximately six times higher than the frequency of fundamental mode and broadband excitation sources covering higher order modes are rare. In addition, higher order modes have lower amplitude and lower stress contributing insignificant power compared to the fundamental mode. The unique shape of fundamental mode allows use of single electrode whereas harvesting additional power from higher order modes is not practical from the same electrode. Therefore analysis of higher order modes is not included in the scope of the thesis.
- As all the performances of the geometries proposed in the thesis are thoroughly verified with FE simulations, experimental verification is unnecessary and is not included in the scope of the thesis.

1.16 THESIS OUTLINE

The thesis is organized into eight chapters. The summary of each chapter is briefly discussed below.

Chapter 1: This chapter presents an introduction to the piezoelectric vibration energy harvester (PVEH), it covers a brief background of piezoelectric materials and energy harvesting techniques. It also presents a literature review for various types of piezoelectric vibration energy harvesters and thereafter motivation and contributions of the thesis.

Chapter 2: In this chapter, PVEH with bimorph piezoelectric layers and an end-mass is modeled and simulated using finite element (FE) analysis software. A piezoelectric-circuit coupled model is constructed and simulated for Eigenmode frequency analysis to obtain resonance frequencies of vibration for open and short circuit conditions. The model is also analyzed for the time domain

and frequency domain response of the PVEH with respect to the sinusoidal input excitation. The FE analysis results are verified with the published experimental and analytical results.

Chapter 3: In this chapter, an analytical model is derived for the one-dimensional vibration of a PVEH consisting of piezoelectric bimorph cantilever with an end-mass. The model can be used to study series as well as parallel-connected piezoelectric layers. The analytical model can estimate the harvested electrical power across a resistive load due to input sinusoidal base excitation; it can also be used to estimate resonance frequency and displacement of end-mass. The results from the derived analytical model are verified with the results from FE analysis of the same PVEH.

Chapter 4: In this chapter, an optimal thickness profile for cantilever-based PVEH is proposed to achieve uniform stress along the beam length. The stress uniformity ensures that the entire piezoelectric material on the beam surface experiences the same level of stress. In the proposed geometry, width is kept constant while the thickness is optimized. The proposed thickness profile is further used to design two separate PVEH geometries, PVEH-1 and PVEH-2. The PVEH-1, consists of a substrate of tapered thickness profile and two piezoelectric layers of uniform thickness, and the PVEH-2 consists of a substrate of uniform thickness profile and two piezoelectric layers of tapered thickness.

Chapter 5: The proposed geometry, PVEH-1, consists of a substrate of tapered thickness profile and two piezoelectric layers of uniform thickness. Analytical expressions are derived for the end-mass displacement, resonance frequency, generated voltage, and generated power. The analysis shows that the proposed PVEH experiences almost uniform stress along the length and generates higher electrical power than an equivalent conventional PVEH with uniform thickness. Due to uniformity in the stress distribution, the proposed PVEH experiences much lower peak stress and higher average stress than that of an equivalent conventional PVEH. The results from the derived analytical expressions are validated with that of the finite element (FE) analysis of an identical PVEH.

Chapter 6: The second proposed geometry is PVEH-2, it is a bimorph with a substrate of uniform thickness and piezoelectric layers of tapered thickness profile. Here the substrate layer thickness is kept uniform, and the piezoelectric layer thickness is varied to get the desired thickness profile. Analytical expressions are developed for the end-mass displacement, generated voltage, resonance frequency, and stress profile. The stress profile is found to be uniform along the length, and a significant increase in the power density is observed compared to an equivalent

conventional PVEH. FE analysis of an identical energy harvester is carried out to compare the results with the solutions of derived analytical expressions.

Chapter 7: In this chapter, a circular diaphragm-based piezoelectric vibration energy harvester is simulated using finite element analysis. The modeled diaphragm is a bimorph parallel-connected energy harvester with a resistive load. Initially, the entire diaphragm is simulated to estimate the total harvested electrical power, and subsequently, the diaphragm is divided into smaller angular slices of equal size, and performance is studied. It is found that the slicing of the diaphragm increases the generated power significantly, which in turn increases the power density of the entire system. As the angular slices of different angles resonate at different frequencies, a combination of different slices is used to design a broadband PVEH.

Chapter 8: The final chapter provides key conclusions of the work done and recommendations for future work.

CHAPTER 2

FINITE ELEMENT ANALYSIS OF PVEH

Finite element (FE) analysis is a computer-based procedure used to model complex systems. In this analysis, the simulation occurs in a virtual environment to produce output results, thus removing the complexity of designing a physical prototype. FE analysis can develop complex geometrical models with almost any kind of size and shape. With the help of FE analysis, it is easy to determine how different factors affect the output results. FE analysis also eliminates the need for a physical prototype in the design steps, significantly reducing the compulsory time and expenditure. FE analysis demonstrates excellent visualization of the simulated device to help the design engineers spot any vulnerabilities and make it easy to fix them before fabrication.

In FE analysis, the entire structure with physical complexities and mathematical discontinuities is divided into smaller and easily manageable segments. These segments signify the physical properties of its local domain. By dividing the entire structure into smaller parts, the simulator understands how the whole system will react to the different external excitations.

The simulation process starts with the placement of nodes on the entire geometry. The node is a point in the system linked with the material properties and structural data of its location. The lines connecting all the nodes create the mesh of the structure. The meshing creates a finite number of simpler and smaller elements of the whole system. All the elements are defined by simple equations concerning strength, stress, thickness, length, etc. The accuracy of the simulation result depends on the density of the mesh structure; higher mesh density provides more accurate results but requires more computational power and time.

In this chapter, FE modeling and simulation of conventional PVEH coupled with resistive load is carried out using COMSOL Multiphysics. A cantilever-based PVEH is simulated to obtain

various output parameters. The results from the FE analysis are verified with the published experimental and analytical results.

2.1 FE MODELING AND SIMULATION

Commercially available software COMSOL Multiphysics is used for the FE modeling and simulation of PVEH. The FE modeling starts with the structural configuration of the energy harvester, where the geometry and sizes are defined. After building the geometry, all the materials are specified. While specifying a particular material, all the physical and electrical parameters like Young's modulus, material density, Poisson's ratio, electrical conductivity, dielectric constant, piezoelectric constants, etc., need to be defined. The substrate, end-mass, and base are defined as linear elastic materials, and the top and bottom layers are defined as a piezoelectric material, as shown in Figure 2.1. The electrode thickness on the piezoelectric material is considered negligible and defined as electrical terminals in the simulation. These terminals are further connected to an external resistive load. Free tetrahedral meshing is used to mesh the energy harvester structure with a minimum element size less than the thickness of the thinnest layer. This simulation of PVEH is carried out using two different physics modules, viz. piezoelectric devices from structural mechanics and electrical circuits from AC/DC module.

2.1.1 FE analysis of bimorph PVEH

Bimorph PVEH devices are modeled and simulated for parallel connection of piezoelectric layers. The fixed end of the cantilever-based bimorph is usually attached to the input vibration source and the end-mass is attached to the free end, as shown in Figure 2.1.

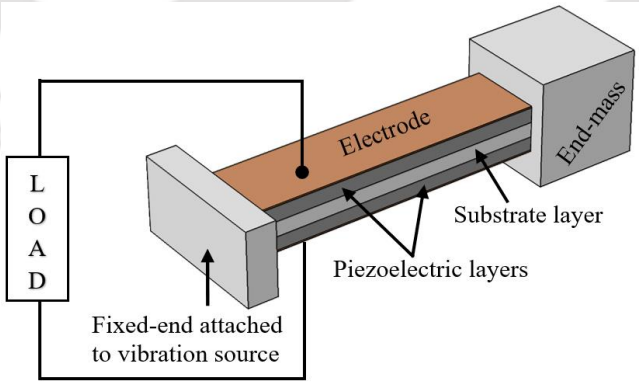

Figure 2.1: A cantilever-based bimorph PVEH.

The meshing of the energy harvester geometry is carried out using the internal tetrahedral meshing available in the software. Figure 2.2 shows the meshed geometry of a cantilever-based PVEH.

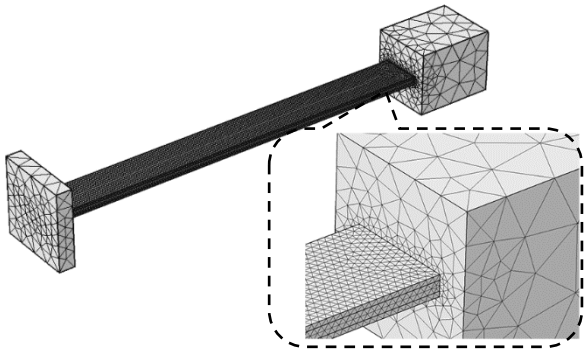

Figure 2.2: Meshing of cantilever-based PVEH.

2.1.2 Types of FE analysis

In the FE analysis of PVEH, the eigenmode frequency analysis, time-dependent analysis, and frequency domain analysis are carried out to visualize different output characteristics of the energy harvester.

The resonance frequency of vibration is estimated from the eigenmode frequency analysis of the energy harvester. During the *eigenmode* frequency analysis, the fixed end of the cantilever is defined as a *fixed body*, and the rest are defined as a *free body*. The load resistance value should be zero to estimate the short-circuit resonance frequency, and it should be very high to estimate the open-circuit resonance frequency. The time-dependent analysis is used to analyze the energy harvester's performance due to varying input excitation over a certain period. This study applies a time-varying input vibration of constant amplitude and frequency to the cantilever base to study its response. In frequency domain analysis, a varying frequency is applied to the base with constant acceleration. In this analysis, peak values of displacement and peak values of voltage across the resistive load are studied.

2.1.3 Simulated PVEH geometry

The accuracy of the FE analysis result depends on the correctness of the defined physical and geometrical parameters. In this study, a PVEH is modeled and simulated to observe output results under different input conditions. The simulation results are further verified with published experimental and analytical results of an identical PVEH.

The energy harvesting device described in [84] by Erturk and Inman is considered for simulation, and the same geometrical parameters and material properties are used. Figure 2.3 (a) shows the image of the device fabricated in [84] and Figure 2.3 (b) shows the corresponding device modeled for simulation. The simulation results from FE analysis are compared with the experimental results reported in [84].

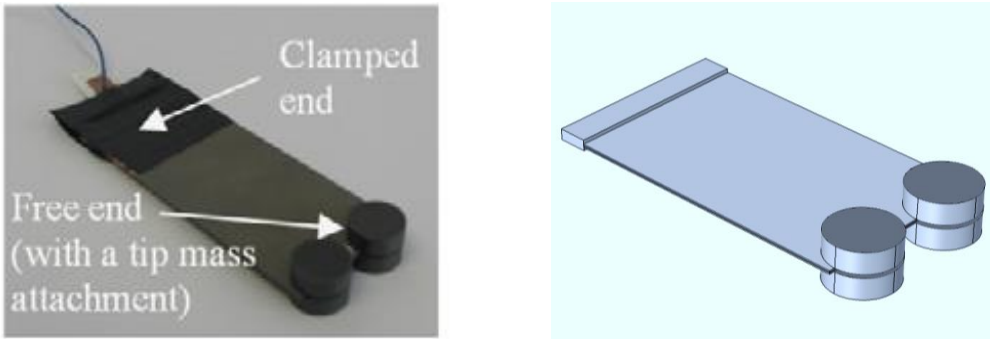

(a) (b)

Figure 2.3: Original device described in [84] and corresponding simulated device.

In addition, the results are also verified with the results obtained by using analytical expressions derived in [135] by the same authors.

In this study, a coupled FE model of the PVEH shown in Figure 2.3 is designed and analyzed in COMSOL. Table 2.1 shows the geometrical and material properties mentioned in [84] and used for FE simulation in this chapter.

Table 2.1: Geometric and material properties of the simulated PVEH.

Geometrical parameters	**Piezoelectric layers**	**Substrate layer**	**Material properties**	**Piezo (PZT-5A)**	**Substrate (Brass)**
Length (mm)	50.8	50.8	Mass density (kg/m^3)	7800	9000
Width (mm)	31.8	31.8	Young's modulus (GPa)	66	105
Thickness (mm)	0.26 (each)	0.14	Piezo constant d_{31} (pm/V)	–190	NA
Tip-mass (kg)	0.012		Permittivity (nF/m)	13.28	NA

2.2 SIMULATION RESULTS

FE analysis of the PVEH is carried out using the geometrical and material properties mentioned in Table 2.1 and different analyses are carried out and the results are discussed in the following subsections.

2.2.1 Resonance frequency of vibration

The resonance frequency of the PVEH is estimated using eigenmode frequency analysis of the energy harvester for short-circuit and open-circuit conditions of the piezoelectric layers, as shown in Figure 2.4 (b). In short-circuit condition, the PVEH shows a resonance frequency of 45.75 Hz, while in the open-circuit condition, the resonance frequency is 48.5 Hz.

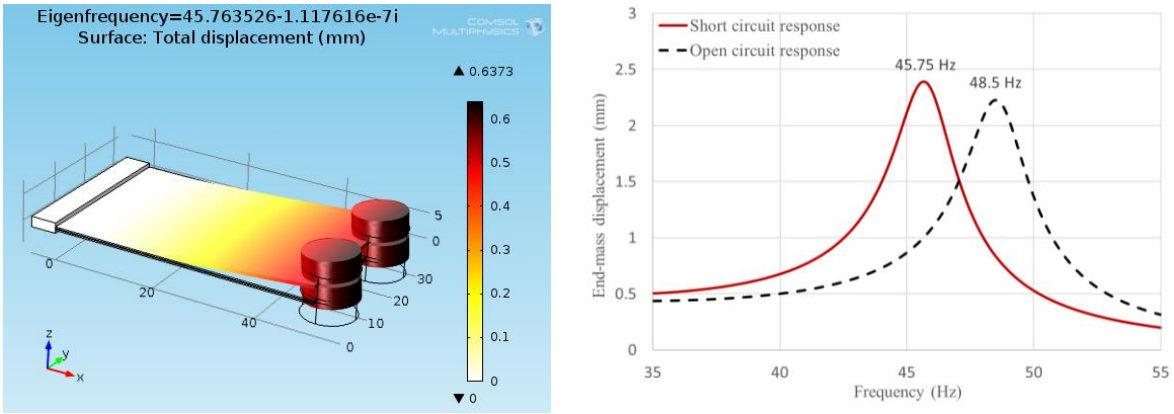

(a) (b)

Figure 2.4: (a) Mode shape at the fundamental resonance frequency, (b) plot of displacement versus frequency for short-circuit and open-circuit conditions.

2.2.2 Time-domain analysis

In time-domain analysis, the simulation result shows the change in behavior of the energy harvester with respect to a time-varying input vibration. The sinusoidal input vibration at the base excites the PVEH to vibrate at the same frequency. Figure 2.5 shows the displacement of the base due to sinusoidal input excitation at the resonance frequency and corresponding end-mass displacement for a load resistance of 1 kΩ.

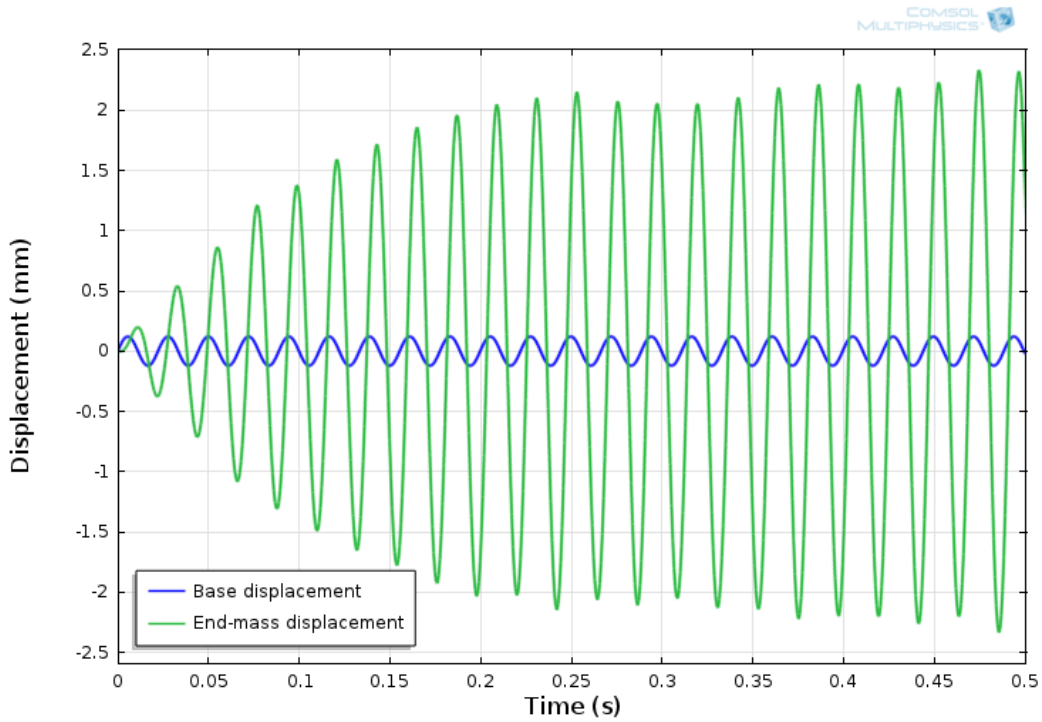

Figure 2.5: Plot of end-mass and base displacements versus time obtained from FE analysis.

In the above case, the input vibration frequency is the same as that of the system resonance frequency and the end-mass of the PVEH shows the highest displacement with a 90^{o} phase difference with the input vibration. When the input vibration frequency is significantly lower

than the resonance frequency, the end-mass oscillates with almost equal phase and amplitude as that of the input vibration, as shown in Figure 2.6. Similarly, when the input vibration frequency is much higher than the system resonance frequency, the end-mass oscillates with almost equal amplitude but 180^{o} out of phase with the input vibration, as shown in Figure 2.7.

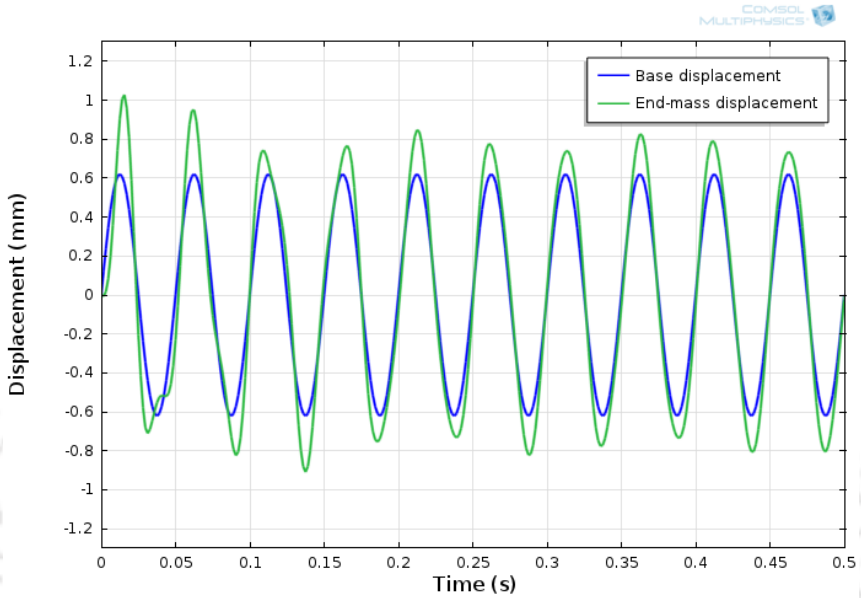

Figure 2.6: Time-domain response of PVEH at 20 Hz frequency.

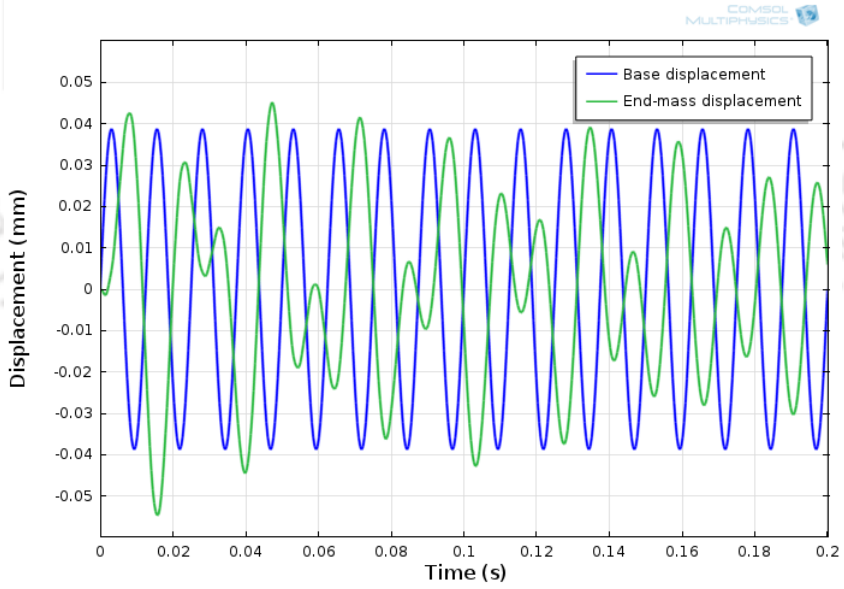

Figure 2.7: Time-domain response of PVEH at 80 Hz frequency.

2.2.3 Frequency domain analysis

In frequency domain analysis, the PVEH is simulated for an input frequency range of interest. During the analysis, the input excitation acceleration is kept constant at 0.2*g*. Figure 2.8 shows the variation of end-mass displacement with input frequency in short-circuit condition. The peak displacement is observed as 2.4 mm at 45.75 Hz frequency.

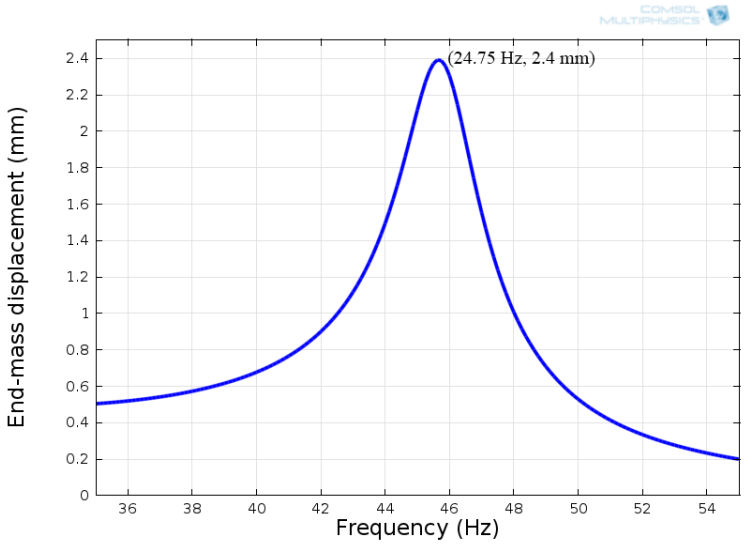

Figure 2.8: Plot of end-mass displacement versus frequency.

2.3 COMPARISON OF RESULTS

The geometrical and material properties of the simulated device are taken from [84], where a bimorph PVEH with end-mass is fabricated and tested. In [135], a mathematical model is presented to estimate output parameters of bimorph PVEH with end-mass. The expressions for end-mass displacement and generated voltage across a load resistance given in [135] are simulated in MATLAB for the same geometrical and material properties as mentioned in Table 2.1. The results from analytical expressions and FE analysis, and the experimental results from [84] are compared. The generated power varies with the variation of connected load resistance, and for an optimal value of load resistance, the harvested power is maximum. The optimal load resistance value is mentioned as 35 kΩ for the original device [84] and we verified it in our simulation. Figure 2.9 and Figure 2.10 compare the results from FE simulation with the corresponding analytical solutions obtained by MATLAB using expressions derived in [135].

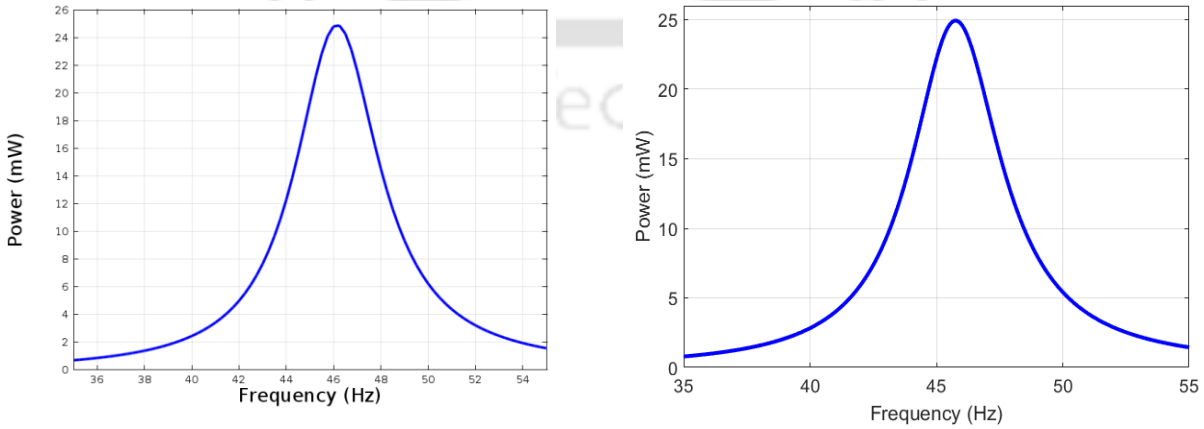

(a) (b)

Figure 2.9: Plot of power versus frequency from (a) analytical expressions reported in [135] and (b) FE simulation.

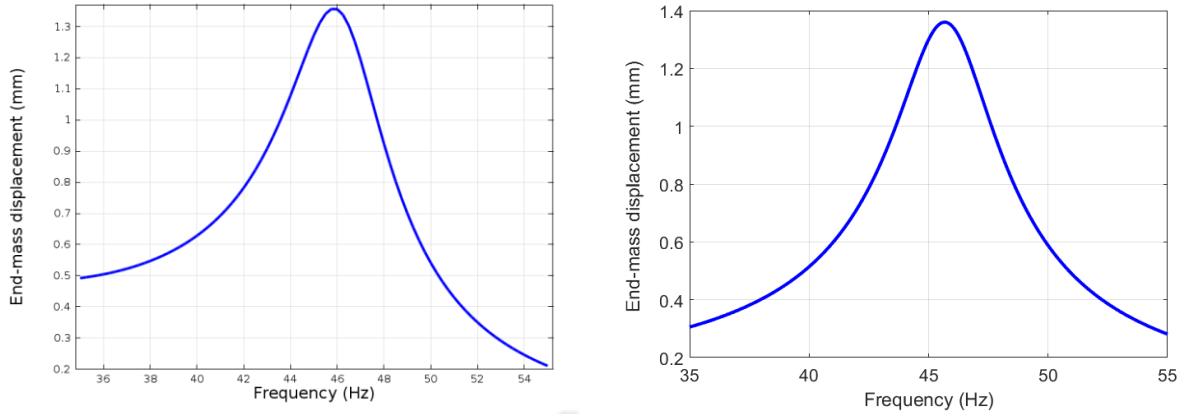

(a) (b)

Figure 2.10. Plot of end-mass displacement versus frequency from (a) analytical expressions reported in [135] and (b) FE simulation.

The FE simulation result of the PVEH demonstrates almost identical results as the experimental results mentioned in [84] and results after solving analytical expressions mentioned in [135], Table 2.2 compares all the results quantitatively.

Table 2.2: Comparison of results from MATLAB and COMSOL.

	From reported analytical model simulated in MATLAB [135]	**From reported experimental results** [84]	**From FE analysis in COMSOL**
Resonance frequency at short-circuit condition	45.38 Hz	45.6 Hz	45.75 Hz
End-mass displacement for R_L = 1 kΩ	2.33 mm	Data not available	2.225 mm
Resonance frequency with R_L = 1 kΩ	45.38 Hz	45.6 Hz	45.75 Hz
Voltage for R_L = 1 kΩ	1.56 V	1.57 V	1.55 V
Resonance frequency with R_L = 470 kΩ	47.8 Hz	48.4 Hz	48.5 Hz
Voltage for R_L = 470 kΩ	94.91 V	84 V	99 V
End-mass displacement for R_L = 470 kΩ	1.69 mm	Data not available	1.54 mm
Maximum generated power	26.44 mW	23.9 mW	26.12 mW

2.4 CONCLUSIONS

A coupled piezoelectric-circuit FE model is analyzed for cantilever-based PVEH using COMSOL Multiphysics. A series-connected bimorph cantilever with end-mass attached is simulated for different input frequencies with constant acceleration. The energy harvester's resonance frequencies for short-circuit and open-circuit conditions are studied. The variation of

generated power and end-mass displacement is studied using frequency domain analysis for different input frequencies.

Results from FE analysis are verified with published analytical expressions simulated in MATLAB and published experimental results of an identical reported device.

CHAPTER 3

PVEH OF UNIFORM THICKNESS

In the previous chapter, FE simulation of PVEH was carried out, and the results were verified with the published experimental and analytical results. FE simulations of PVEH have their advantages and disadvantages over analytical results. An FE simulation can mimic experimental results even for a complicated geometry that is difficult to model analytically. On the other hand, for simple geometry, an analytical expression is easier to derive and can produce output results very swiftly compared to FE simulation results.

In this chapter, analytical expressions are derived to estimate the resonance frequency, end-mass displacement, stress on the cantilever beam, and generated voltage across an externally connected load resistor. The system's resonance frequency is calculated using Rayleigh's method, and the expression for generated voltage is derived for a connected load resistor. The energy harvester performance is studied in terms of the amount of electrical power generated across a connected load resistor. The results from the analytical solution are compared with the results from the FE analysis carried out in COMSOL Multiphysics.

3.1 MODELING ASSUMPTIONS

The energy harvester considered for modeling in this chapter is a composite cantilever with uniform thickness and an end-mass attached symmetrically to the free end, as shown in Figure 3.1. The central layer is a brass substrate sandwiched between two piezoelectric layers of PZT-5H.

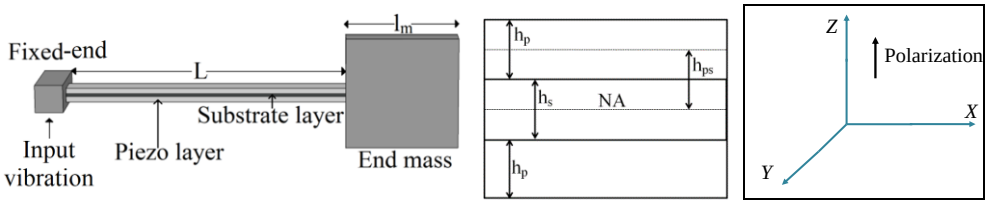

Figure 3.1: Side view of energy harvester and cross-sectional view of the bimorph.

Figure 3.1 shows the schematic diagram of the cantilever-based bimorph PVEH of length L and its cross-section view, where h_s and h_p are the substrate layer and piezoelectric layer thicknesses, NA is the beam's neutral axis, h_{ps} is the distance between the center of the piezoelectric layer and the NA. Due to the motion of the end-mass, the moment exerts stress on the piezoelectric material, generating electrical charge on metallic electrodes attached to both sides of piezoelectric layers. The input vibration is assumed to be sinusoidal and applied in the z-direction, the end-mass motion will also be in the z-direction, and the stress on the piezoelectric material will be in the x-direction.

The piezoelectric layers' top and bottom surfaces are metalized to form the electrodes. The piezoelectric layers can be wired as parallel or series connections, as shown in Figure 3.2 (a) and (b). For parallel connection, the polling of the piezoelectric layers is in the same direction, producing electric fields in opposite directions. On the other hand, piezoelectric layers are poled in the opposite direction for the series connection to create electric fields in the same direction.

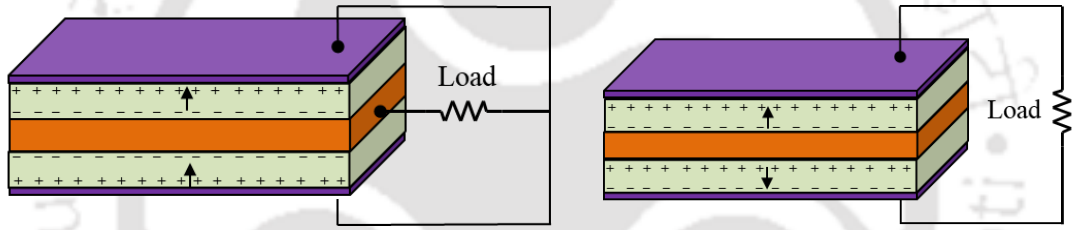

Figure 3.2**:** (a) parallel and (b) series connection of bimorph.

3.2 MODEL DERIVATION

The frequently used spring-mass-damper model of vibration energy harvester [71] is shown in Figure 3.3. The model consists of an equivalent mass m_e, a spring with constant k, and dampers. b_m represents mechanical damping coefficient, and θ represents damping coefficient due to electromechanical energy conversion.

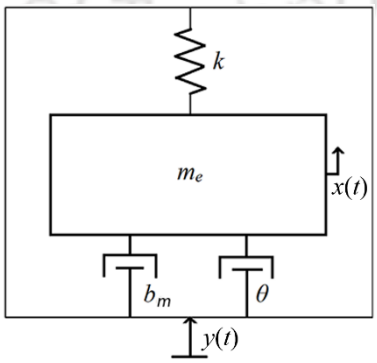

Figure 3.3: Spring-mass-damper model of PVEH.

In Figure 3.3, $y(t)$ is the input base displacement, $x(t)$ is the absolute displacement of the end-mass, and $z(t)$ is the displacement of the end-mass relative to the base displacement. Then, the equation of motion of the end-mass is given by [136], [137]

$$m_e\ddot{z}(t) + b_e\dot{z}(t) + kz(t) + \theta v = m_e\ddot{y}(t) \tag{3.1}$$

$$\ddot{z}(t) + 2\zeta_m\omega_n\dot{z}(t) + \omega_n^2 z(t) + \frac{\theta}{m_e}v = \ddot{y}(t) \tag{3.2}$$

where ω_n is the resonance frequency of vibration, v is the generated voltage, ζ_m is the mechanical damping ratio. The equivalent circuit equation of the PVEH in the electrical domain with mechanical coupling is derived using constitutive equations of piezoelectric material as follows.

For the cantilever-based PVEH, the constitutive equations of piezoelectric material can be written as

$$D_3 = d_{31}T_1 + \varepsilon_{33}^T E_3 \tag{3.3}$$

where T_1 is the stress, D_3 is electric displacement, E_3 is the electric field, and $\varepsilon_{33}^{\mathrm{T}}$ is permittivity at constant stress [91]. The subscripts 1 and 3 denote the direction along which a particular parameter is measured.

The stress $T(x)$ in the piezoelectric layer along the length of the cantilever beam is expressed as

$$T(x) = \frac{M(x)}{I}h_{ps} \tag{3.4}$$

where I representing the cross-section moment of inertia of the composite cantilever beam, $M(x)$ is moment due to the motion of the end-mass [74] and is given by

$$M(x) = (L + l_m/2 - x)F \tag{3.5}$$

where F is the force at the end of the cantilever due to motion of the end-mass and is the product of spring constant k and displacement z of the end-mass. Therefore equation (3.4) becomes

$$T(x) = \frac{kz(L + l_m/2 - x)}{I}h_{ps} \tag{3.6}$$

As noted from equation (3.6), the stress is maximum at $x = 0$ and minimum at $x = L$; thus, the average stress can be written as

$$T = \frac{1}{L}\int_0^L \frac{kz(L + l_m/2 - x)}{I}h_{ps}dx \tag{3.7}$$

$$T = \frac{kz(L + l_m)}{2I}h_{ps} \tag{3.8}$$

The spring constant k is expressed as

$$k = \frac{3YI}{\left(L + \frac{l_m}{2}\right)^3} \tag{3.9}$$

where *YI* is the bending stiffness of the composite cantilever beam and can be written as [125]

$$YI = Y_s \frac{bh_s^3}{12} + Y_p \frac{2b}{3}\left[\left(h_p + \frac{h_s}{2}\right)^3 - \left(\frac{h_s}{2}\right)^3\right] \tag{3.10}$$

Using equations (3.8) and (3.9), we can rewrite equation (3.3) as

$$D_3 = d_{31}\left[\frac{kz(L + l_m)}{2I} h_{ps}\right] - \varepsilon_{33}^T \frac{v}{h_p} \tag{3.11}$$

where *v* is the voltage across a connected load resistor. The generated charge on the electrode is given by

$$q = D_3 bL = d_{31}\left[\frac{kz(L + l_m)}{2I} h_{ps}\right](bL) - \varepsilon_{33}^T \frac{v}{h_p}(bL) \tag{3.12}$$

and the current through the load resistance is written as

$$i = \frac{v}{R} = \frac{dq}{dt} = d_{31}\left[\frac{kbL(L + l_m)}{2I} h_{ps}\right]\frac{dz}{dt} - \frac{\varepsilon_{33}^T bL}{h_p}\frac{dv}{dt} \tag{3.13}$$

and the above equation can be simplified as

$$\frac{v}{R} + C_p \frac{dv}{dt} = \theta \frac{dz}{dt} \tag{3.14}$$

where $\theta = d_{31}\left[\frac{kbL(L+l_m)}{2I} h_{ps}\right]$ is the electrically induced damping coefficient and $C_p = \frac{\varepsilon_{33}^T bL}{h_p}$ represents the capacitance of a single piezoelectric layer.

Equation (3.14) is the electrical circuit equation of the piezoelectric energy harvester. Equations (3.2)and (3.14) are called electromechanically coupled governing equations for the PVEH.

3.2.1 PVEH with parallel connection of the piezoelectric layers

When the piezo layers are connected in a parallel configuration, the equivalent capacitance of the energy harvester becomes double of that in the single piezoelectric layer, thus for parallel-connected energy harvester, equation (3.14) becomes

$$\frac{v(t)}{R} + 2C_p \frac{dv(t)}{dt} = 2\theta \frac{dz(t)}{dt} \tag{3.15}$$

$$v(t) + 2RC_p \frac{dv(t)}{dt} - 2R\theta \frac{dz(t)}{dt} = 0 \tag{3.16}$$

and the equation in the mechanical domain will be

$$\ddot{z}(t) + 2\zeta_m \omega_n \dot{z}(t) + \omega_n^2 z(t) + \frac{2\theta}{m_e} v(t) = \ddot{y}(t) \tag{3.17}$$

Equations (3.16) and (3.17) are called the coupled equation for parallel-connected bimorph PVEH. The dynamic response of the cantilever beam and the voltage across load resistance can be estimated by solving these two equations for $z(t)$ and $v(t)$.

When the input base excitation has a periodic motion of angular frequency ω, the end-mass motion and the output voltage are also periodic of the form $z(t) = Ze^{j\omega t}$ and $v(t) = Ve^{j\omega t}$, where Z and V are respectively the peak amplitudes of displacement and voltage. After solving for displacement z and generated voltage v, we get

$$z(t) = -\frac{m_e\omega^2 Y_0\left(1 + j2RC_p\omega\right)}{(\omega_n^2 - \omega^2 + j2\zeta_m\omega\omega_n)\left(m_e + j2m_eRC_p\omega\right) + j4R\theta^2\omega} e^{j\omega t} \tag{3.18}$$

and

$$v(t) = -\frac{2jR\theta m_e\omega^3 Y_0}{(\omega_n^2 - \omega^2 + j2\zeta_m\omega\omega_n)\left(m_e + j2m_eRC_p\omega\right) + j4R\theta^2\omega} e^{j\omega t} \tag{3.19}$$

Once $v(t)$ is calculated, the power transferred to the load can be computed using the $v(t)^2/R$ relation.

3.2.2 PVEH with series connection of the piezoelectric layers

When the piezoelectric layers are connected in series, the equivalent capacitance becomes half of that in the single layer. Thus for series-connected piezoelectric layers, the equation will be

$$\frac{v(t)}{R} + \frac{C_p}{2}\frac{dv(t)}{dt} = \theta\frac{dz(t)}{dt} \tag{3.20}$$

$$2v(t) + RC_p\frac{dv(t)}{dt} - 2R\theta\frac{dz(t)}{dt} = 0 \tag{3.21}$$

and the equation in the mechanical domain will become

$$\ddot{z}(t) + 2\zeta_m\omega_n\dot{z}(t) + \omega_n^2 z(t) + \frac{\theta}{m_e}v(t) = \ddot{y}(t) \tag{3.22}$$

Equations (3.21) and (3.22) are called the coupled equation for series-connected bimorph PVEH. Solving these two equations for displacement z and generated voltage v, the dynamic response of the beam and generated voltage can be estimated.

After solving for z and v, we get

$$z(t) = -\frac{m_e\omega^2 Y_0\left(2 + jRC_p\omega\right)}{(\omega_n^2 - \omega^2 + j2\zeta_m\omega\omega_n)\left(2m_e + jm_eRC_p\omega\right) + j2R\theta^2\omega} e^{j\omega t} \tag{3.23}$$

and

$$v(t) = -\frac{j2m\omega^3 R\theta Y_0}{(\omega_n^2 - \omega^2 + j2\zeta_m\omega\omega_n)\left(2m_e + jm_eRC_p\omega\right) + j2R\theta^2\omega} e^{j\omega t} \tag{3.24}$$

3.3 NATURAL FREQUENCY OF THE PVEH

The natural frequency of the PVEH is calculated using Rayleigh's method [138], which requires the expressions for maximum potential energy (U) and maximum kinetic energy (T_k). The deflection curve of the cantilever beam as a function of distance x from the fixed-base for an applied force F is given by [138]

$$z(x) = \frac{Fx^2}{6YI}(3L - x) \tag{3.25}$$

The maximum potential (U) energy of the beam is written as

$$U = \frac{1}{2}\int_0^L YI\left[\frac{d^2z}{dx^2}\right]^2 dx \tag{3.26}$$

The maximum kinetic energy (T_k) of the energy harvester vibrating at frequency ω_n is given by

$$T_k = \frac{1}{2}\omega_n^2\int_0^L \rho z^2\, dx + \frac{1}{2}M_t\omega_n^2 Z^2 \tag{3.27}$$

where ρ is the mass per unit length of the composite beam, $\omega_n Z$ represents peak velocity of the end-mass and M_t is its mass [139]

Equating equations (3.26) and (3.27), the natural frequency of vibration can be expressed as

$$\omega_n = \sqrt{\frac{\int_0^L YI\left[\frac{d^2z}{dx^2}\right]^2 dx}{\int_0^L \rho\, z^2\, dx + M_t\, Z^2}} \tag{3.28}$$

3.4 MODEL VALIDATION BY FE ANALYSIS

Analytical expressions have been derived for the end-mass displacement, resonance frequency, generated voltage and generated electrical power from the PVEH. These expressions are solved using MATLAB to obtain the results for varying input frequencies and different load resistances. The results obtained from the derived analytical expressions are compared with the results from FE analysis of an identical PVEH.

3.4.1 FE modeling in COMSOL Multiphysics

The FE model of the PVEH is developed using COMSOL Multiphysics software in chapter-2. The bimorph is connected with the resistive load using the piezoelectric-circuit interface, and a sinusoidal input of constant acceleration of $0.2g$ is applied at the base. The PVEH is simulated to obtain the end-mass displacement and generated power across a load resistance as a function of the input frequency. The geometrical parameters and material properties used in the simulation are shown in Table 3.1.

Table 3.1: Geometric and material parameters used in the simulation.

Parameters	Description	Values	Units
L	Beam length	50	mm
b	Beam width	5	mm
h_p	Piezoelectric layer thickness	0.5	mm
h_s	Substrate layer thickness	0.5	mm
l_m	End-mass length	10	mm
l_b	End-mass width	5	mm
l_h	End-mass thickness	7.8	mm
Y_s	Young's modulus of substrate material	110	GPa
Y_p	Young's modulus of piezoelectric material	60.6	GPa
ρ_s	Mass density of piezoelectric material (PZT-5H)	7500	kg/m^3
ρ_p	Mass density of substrate material (Brass)	9000	kg/m^3
ρ_m	Mass density of end-mass material (Brass)	9000	kg/m^3
$\ddot{y}$	Input acceleration at the base	0.2g	m/s^2

3.4.2 Short-circuit and open-circuit analysis

The stiffness of a piezoelectric material varies with electrical loading; for short-circuit conditions, a piezoelectric material exhibits lower stiffness than an open-circuit condition. The relative displacement of the end-mass is obtained using equation (3.18) and is plotted as a function of input frequency in Figure 3.4 (a). The short-circuit and open-circuit resonance frequencies are 99.80 Hz and 105.50 Hz, respectively. The short-circuit and open-circuit resonance frequencies obtained from FE analysis (Figure 3.4 (b)), respectively, are 100.00 Hz and 105.75 Hz.

3.4.3 Effect of load resistance

The plot of generated power obtained from the derived analytical expression for a set of load resistances is shown in Figure 3.5 (a). As the external load resistance increases, the resonance frequency steadily moves from short-circuit resonance frequency to open-circuit resonance frequency and the harvested power changes. In Figure 3.5, two peaks in the output power are observed for two different load resistance values. The first peak is observed at 100 Hz frequency for a load resistance value of 10 kΩ, and the second peak is observed at 105.5 Hz for a load resistance value of 500 kΩ. The difference of 5.5 Hz for the short-circuit and open-circuit conditions of the PVEH is very well predicted by the derived analytical expression shown in Figure 3.5 (a) and the FE simulation results shown in Figure 3.5 (b).

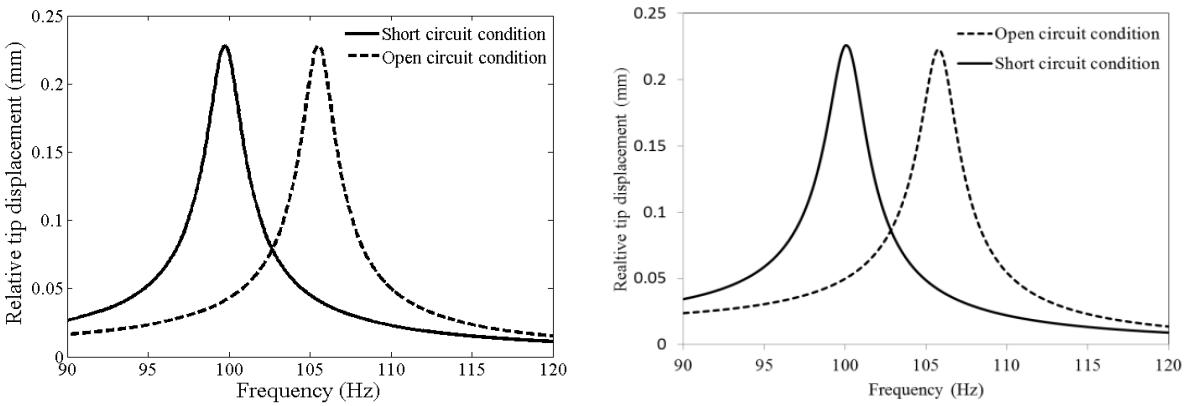

Figure 3.4: Plots of end-mass displacement versus excitation frequency obtained from (a) analytical expression and (b) FE simulation.

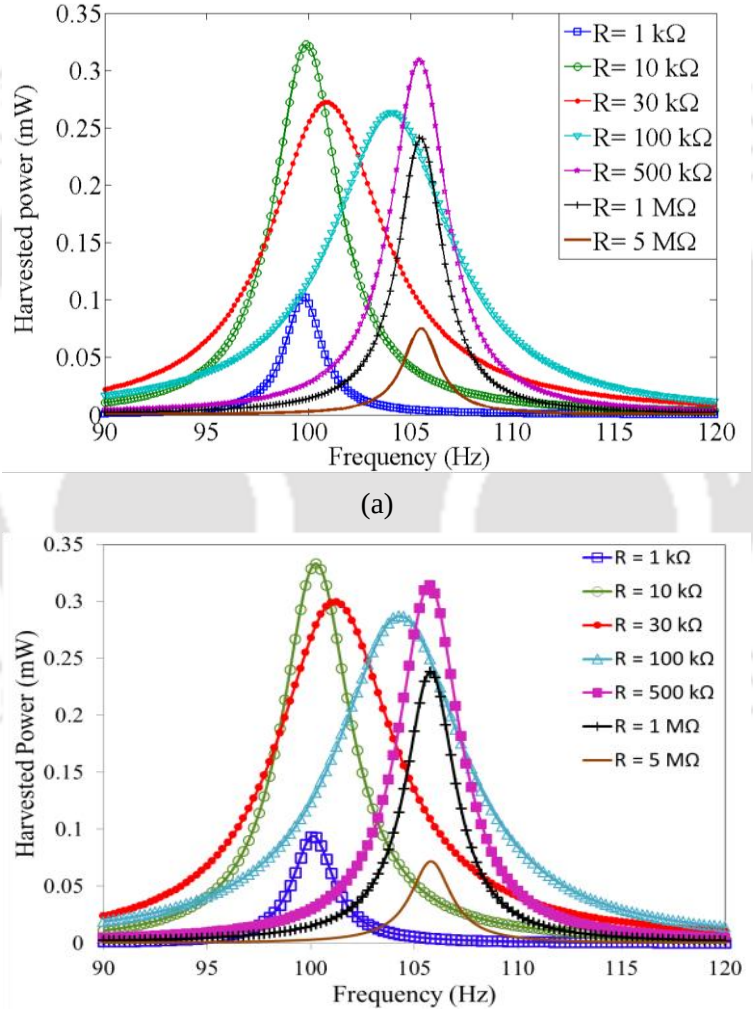

Figure 3.5: Plots of generated power versus input frequency for different load resistances obtained using (a) analytical expression and (b) FE simulation.

3.4.4 Performance at optimal load resistance

At the resonance frequency, the harvested power depends on the load resistance value, and for every excitation frequency, there exists an optimal load resistance value for maximum power generation. When the PVEH is excited with the short-circuit resonance frequency, the optimal load resistance is 10 kΩ. When the PVEH is excited with the open-circuit resonance frequency, the optimal load resistance is 500 kΩ. The peak power output is 0.323 mW for excitation at 100 Hz with the optimal load resistance (10 kΩ) connected.

The performances of the PVEH with the 10 kΩ load resistance connected across its terminals are studied and plotted below. Figure 3.6 (a) and (b) show the plots of end-mass displacement versus frequency obtained using the derived analytical expression and FE simulation, respectively. Figure 3.7 (a) and (b) show the plots of generated power versus frequency obtained using the derived analytical expression and FE simulation, respectively.

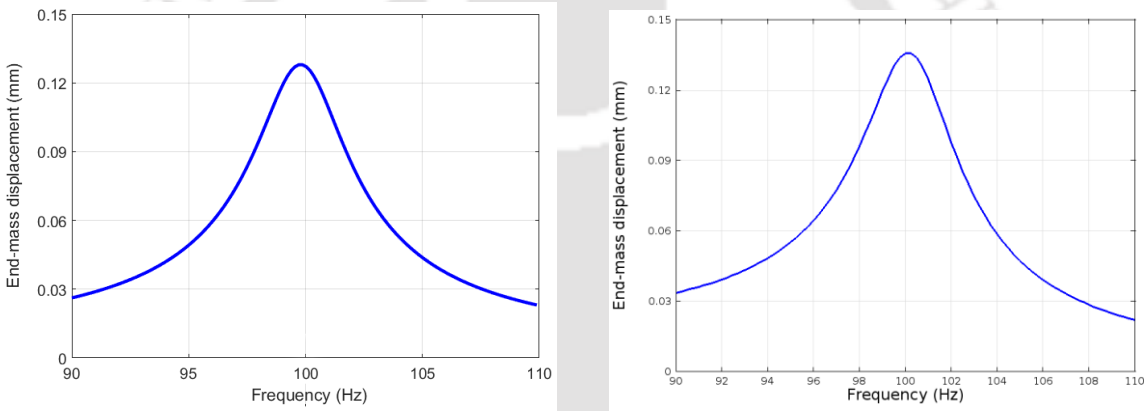

(a) (b)

Figure 3.6: Plots of end-mass displacement for 10 kΩ load versus frequency obtained from (a) analytical expression and (b) FE simulation.

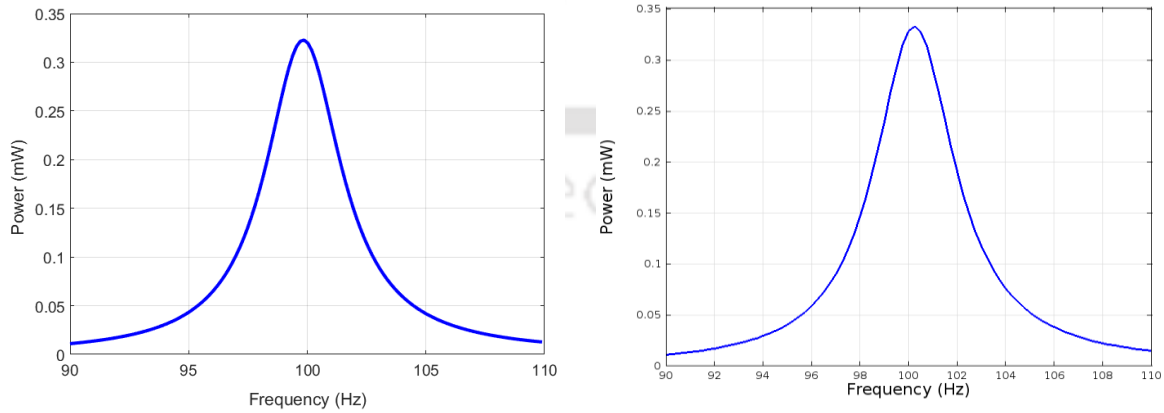

(a) (b)

Figure 3.7: Plots of harvested power for 10 kΩ load versus frequency obtained from (a) analytical expression and (b) FE simulation.

3.4.5 Variation of voltage and current with the load resistor

The short-circuit and open-circuit resonance frequencies are found to be 100 Hz and 105.5 Hz, respectively, and are the frequencies of practical importance. The short-circuit condition is defined as the load resistor value tends to zero, whereas the open-circuit condition is defined as the load resistor value close to infinity. The variation of output voltage with load resistance for excitation at the two frequencies (100 Hz and 105.5 Hz) is shown in Figure 3.8

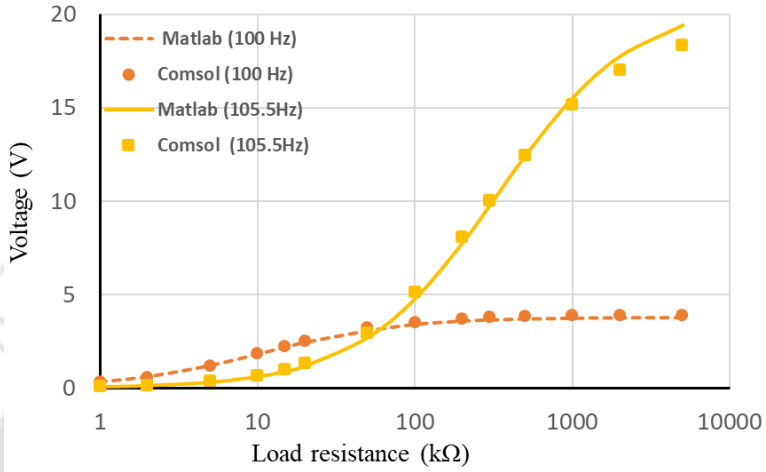

Figure 3.8: Variation of the peak voltage with load resistance for input excitations at the short-circuit resonance frequency (100 Hz) and open-circuit resonance frequency (105.5 Hz) using analytical expression (MATLAB) and FE analysis (COMSOL).

Figure 3.9 shows the variation of current through the load resistance for excitation at the short-circuit and open-circuit resonance frequencies from analytical solution (MATLAB) and FE analysis (COMSOL). The current through the load resistance decreases slowly as the load resistor value increases. There exists a particular load resistor value (62 kΩ) for which the current output is equal for both the excitation frequencies.

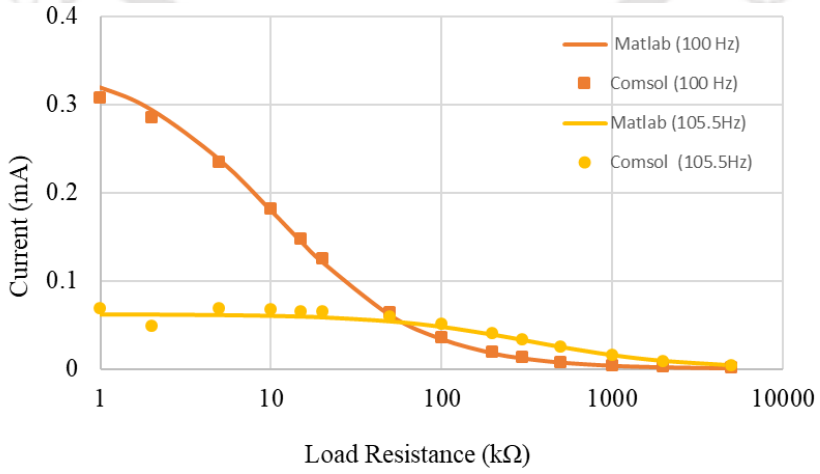

Figure 3.9: Variation of the peak current with load resistance for input excitations at the short-circuit resonance frequency (100 Hz) and open-circuit resonance frequency (105.5 Hz) using analytical expression (MATLAB) and FE analysis (COMSOL).

The electrical power variation with change in resistive load is shown in Figure 3.10 for the excitations at short-circuit and open-circuit frequencies. At short-circuit excitation frequency, the energy harvester has an optimal load resistance value of 10 kΩ, whereas, at open-circuit excitation frequency, the optimal value of load resistor is 500 kΩ. The generated power from the energy harvester for excitation at short-circuit resonance frequency is found to be 0.323 mW for the load resistance value of 10 kΩ. In contrast, for the excitation at the open-circuit resonance frequency, the power is found to be 0.320 mW for the load resistance value of 500 kΩ.

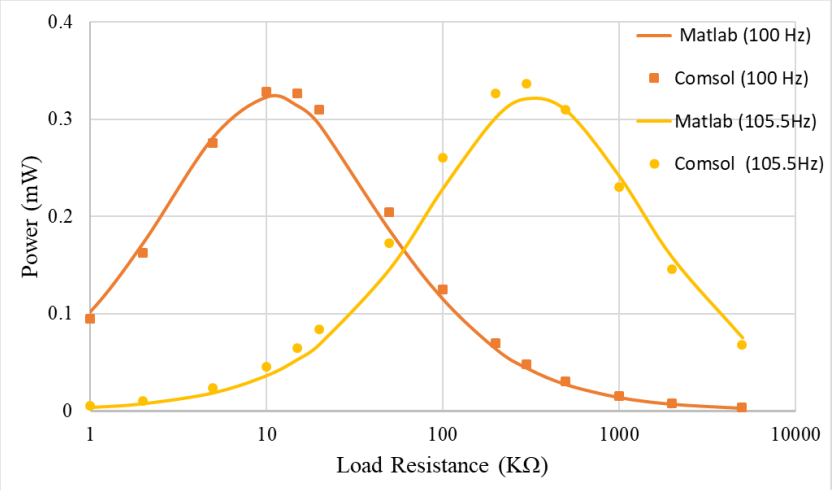

Figure 3.10: Variation of the peak power with load resistance for excitations at the short-circuit resonance frequency (100 Hz) and open-circuit resonance frequency (105.5 Hz) using analytical expression (MATLAB) and FE analysis (COMSOL).

3.4.6 Damping effect of the load resistance

From the discussions above, it is clear that the energy harvester exhibits different resonance frequencies depending on the connected load resistance. As the load resistor value increases from a very low value to a very high value, the energy harvester shifts from short-circuit resonance frequency (100 Hz) to open-circuit resonance frequency (105.5 Hz). Table 3.2 shows the variation of resonance frequency with the load resistance.

Input excitations are applied at the resonance frequencies corresponding to the connected load resistance and the performances are studied. Figure 3.11 shows that below the load resistor value 62 kΩ, the energy harvester works in the range of short-circuit resonance frequency. Above 62 kΩ, the energy harvester starts working in the range of the open-circuit resonance frequency.

Table 3.2: Variation of resonance frequency with the load resistance.

Load resistance (kΩ)	Resonance frequency (Hz)
1	99.82
2	99.82
5	99.82
10	100.15
15	100.15
20	100.25
50	102.25
100	104.12
200	105.06
300	105.40
500	150.40
1000	105.55
2000	105.55
5000	105.55

When the load resistance is very low, the damping due to electrical conversion of energy is minimum, and the displacement of the end-mass is maximum. As the load resistance is increased, the end-mass displacement starts to decrease and reaches a minimum for a load resistance value of R = 62 kΩ. After that, the end-mass displacement increases until it reaches a maximum at the open-circuit condition. Figure 3.11 (a) shows the variation of end-mass displacement with load resistance at the corresponding resonance frequencies and verifies the damping effect due to the load resistance. Figure 3.11 (b) shows the variation of generated peak power with load resistance at the corresponding resonance frequencies. The plot of power from analytical expression shows two maxima, at 99.80 Hz (short-circuit resonance frequency) and at 105.50 Hz (open-circuit resonance frequency). The corresponding frequencies for FE analysis are 100 Hz and 105.75 Hz, respectively.

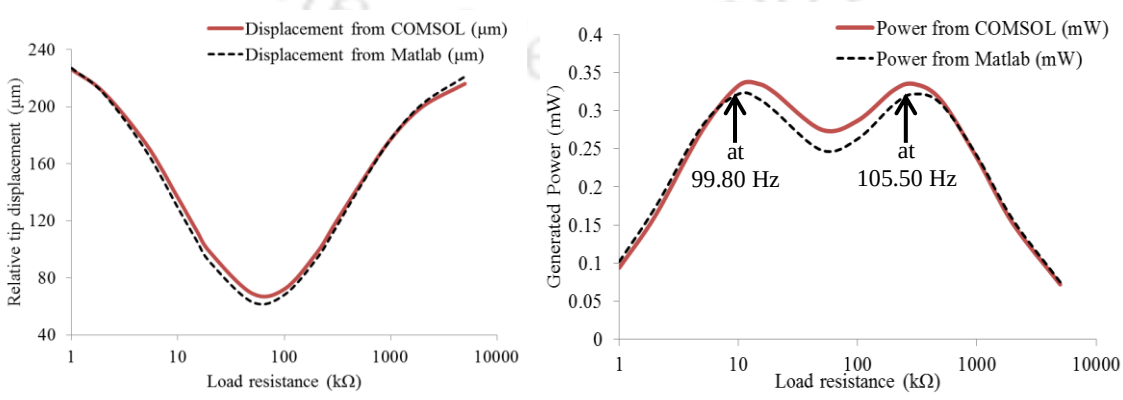

(a) (b)

Figure 3.11: Plots of (a) displacement of end-mass and (b) generated power versus load resistance at the resonance frequency.

3.5 POWER DENSITY

The conventional practice to estimate the energy harvester's performance is by the power density value, usually defined by the amount of generated power divided by the device volume [47], [140]. In this case, the device volume is considered as the sum of the beam volume and the end-mass volume. The base volume is ignored as the base is a part of the vibration source. The volume of the beam is 0.375 $cm^{3,}$ whereas the volume of the end-mass is 0.390 cm^3, yielding the total device volume of 0.765 cm^3. The peak power density for optimal load resistance is found to be 0.422 mW/cm^3 for excitation at 100 Hz with 0.2g acceleration.

3.6 CONCLUSIONS

In this chapter, a lumped parameter model is derived for the analysis of uniform thickness PVEH consisting of a bimorph piezoelectric cantilever with end-mass. Mathematical expressions are derived for natural frequency, displacement of end-mass and generated voltage for parallel and series configurations of the bimorph. For the parallel configuration of the piezoelectric layers, the derived expressions have been evaluated in MATLAB and the results are validated using FE analysis of an identical system.

The analytical model is further used to find the short-circuit and open-circuit resonance frequencies of the PVEH. The effect of load resistance on the end-mass displacement, resonance frequency, generated voltage is studied and the optimal load resistance has been found for maximum power generation. The comparison of the results is summarized in Table 3.3.

Table 3.3: Comparison of results from analytical expressions and FE analysis.

Parameters	**MATLAB result by solving derived analytical expressions**	**FE simulation results**
Short-circuit resonance frequency	99.80 Hz	100.00 Hz
Open-circuit resonance frequency	105.50 Hz	105.75 Hz
Displacement of end-mass at optimal load	127 μm	134 μm
Harvested power at optimal load (10 kΩ)	0.323 mW	0.334 mW
Power density	0.422 mW/cm^3	0.437 mW/cm^3

CHAPTER 4

THICKNESS PROFILE FOR UNIFORM STRESS IN PVEH

In the previous chapter, analytical expressions have been derived to estimate resonance frequency, end-mass displacement, generated voltage, and power for a conventional PVEH of uniform thickness. The results from the analytical expressions are verified with the results from the FE analysis. Usually, a conventional cantilever-based piezoelectric energy harvester is a fixed-free cantilever beam with an end-mass attached to its free end and input excitation applied to the fixed end, i.e., base. When the free end is subjected to a displacement with respect to its base, the beam experiences stress proportional to the strain caused by bending. It is observed that the stress on the cantilever beam is maximum at the fixed end and decreases linearly towards the free end. In the case of a conventional PVEH of uniform cross-section, the piezoelectric material is generally used on the entire length of the cantilever beam [101], [141]–[144], but only a specific portion of the piezoelectric material experiences significant stress and primarily contributes to the generated electrical energy. As a result, some part of the piezoelectric material remains underutilized. For high efficiency, the entire piezoelectric material on the cantilever beam should contribute maximum in the energy generation process. It will significantly increase overall generated power as well as the power density of the energy harvester. In recent years many researchers have claimed to have achieved higher harvested power by altering the cross-section of conventional cantilever-based PHEVs [45], [121], [145]–[149], as discussed in chapter-1.

The main contribution of this chapter is the determination of optimal thickness profile for cantilever-based PVEH to achieve uniform stress throughout the beam so that the entire piezoelectric material on the surface experiences the same level of stress. In the proposed geometry, width is kept constant while the thickness is optimized.

4.1 STRESS AND POWER RELATION

The electric field on a stressed piezoelectric material is proportional to the applied stress. Therefore, for a cantilever-based PVEH, the average stress on the piezoelectric material plays a significant role in the output power. The average stress on piezoelectric material should be maximum to generate maximum power. The relationship of generated voltage with applied stress can be derived using the piezoelectric constitutive equation [150] given in (3.3).

$$D_3 = d_{31}T_1 + \varepsilon_{33}^T E_3 \tag{4.1}$$

where, D = charge density (C/m^2), T = stress (N/m^2), d = piezoelectric constant, ε = permittivity (F/m) and E = electric field (V/m), for an open-circuit case, the above equation reduces to

$$E_3 = -\frac{d_{31}T_1}{\varepsilon_{33}^T} \tag{4.2}$$

And the generated voltage due to stress T can be written as

$$V_3 = -\frac{d_{31}t_p}{\varepsilon_{33}^T}T_1 \tag{4.3}$$

Equation (4.3) shows that increasing the stress on the piezoelectric material increases the generated voltage. The generated power is proportional to the square of the generated voltage, and thus, to maximize the electrical power output, the stress on the piezoelectric material should be of the highest possible value.

4.2 STRESS ON THE CONVENTIONAL CANTILEVER BEAM

A conventional cantilever is a beam with a uniform cross-section throughout the length. Figure 4.1 shows the side view of a conventional cantilever beam having length L where force F is applied at the free end ($x = L$) and the other end ($x = 0$) is fixed. The width of the beam is b and the thickness is h.

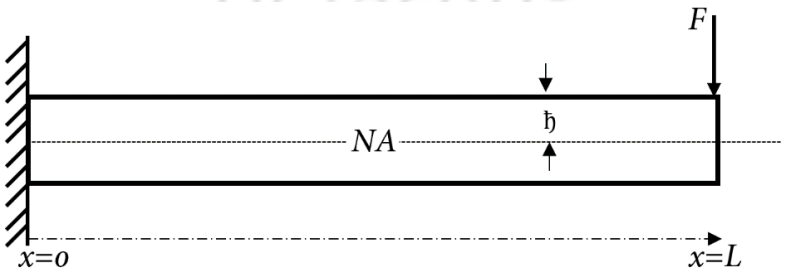

Figure 4.1: Side view of a conventional cantilever beam.

Stress on the surface of a cantilever beam under point force F at the free end depends on the beam bending curvature and the distance between the surface and the neutral axis (NA) denoted

by $\hbar$. Further, the bending curvature depends upon the moment of the applied force and the beam's moment of inertia [151] and is given by

$$\frac{d^2z}{dx^2} = \frac{M(x)}{YI} \tag{4.4}$$

where z is the displacement of the beam's neutral axis, Y is Young's modulus, $M(x)$ is the bending moment at any arbitrary point x along the length, and I is the cross-section moment of inertia. The bending moment $M(x)$ and cross-section moment of inertia I are given by

$$M(x) = (L - x)F \tag{4.5}$$

$$I = \frac{bh^3}{12} \tag{4.6}$$

The stress on the beam surface (at $\hbar = h/2$) along the length due to bending moment $M(x)$ can be written as [151]

$$T(x) = h\frac{M(x)}{2I} \tag{4.7}$$

$$T(x) = \frac{6(L - x)F}{bh^2} \tag{4.8}$$

From (4.8), it is evident that the stress is highest at the fixed end of the cantilever beam. For more elaborate discussion, an example of a conventional cantilever with the specifications given in Table 4.1 is examined.

Table 4.1: Geometric parameters of the conventional cantilever to study the stress profile.

Parameters	Description	Values	Units
L	Beam length	30	mm
b	Beam width	5	mm
h	Beam thickness	1	mm
F	Applied force	0.5	N

The stress on the beam surface is calculated using (4.8) and is plotted against length in Figure 4.2. FE analysis of the same cantilever is carried to find out the stress distribution for an applied force of 0.5 N. Free tetrahedral meshing is used to mesh the geometry. The stress profile on the cantilever surface from FE analysis is shown in Figure 4.3.

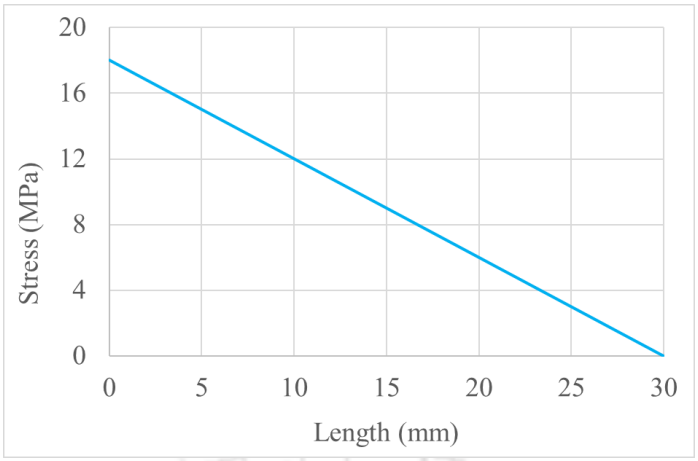

Figure 4.2: Stress distribution on a conventional cantilever calculated from (4.8).

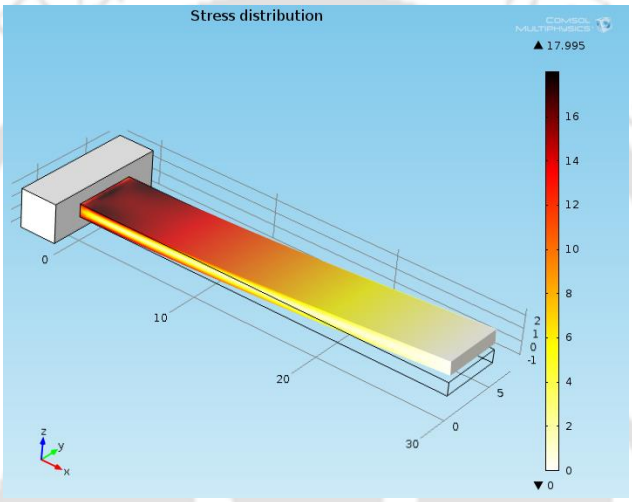

Figure 4.3: Stress distribution on a conventional cantilever obtained from FE analysis.

It is observed that in a conventional cantilever of uniform cross-section, the stress on the beam surface decreases linearly from the fixed end to the free end, as shown in Figure 4.2 and Figure 4.3. In this type of stress distribution, the fixed end of the cantilever experiences very high stress and decreases linearly to zero at the free end. It is noted that the piezoelectric material on the cantilever beam also experiences this stress variation, significantly reducing the average stress on the material and resulting in lower electrical power generation. In addition, the non-uniformity in stress makes the fixed end prone to mechanical failure due to the highest stress value.

4.3 Derivation of thickness profile for uniform stress

Our objective is to design a PVEH where the stress on the piezoelectric material is uniform, so that the average stress and the harvested power will improve. Researchers have worked on uniform strength beams that have geometry resulting in uniform stress along the beam to prevent mechanical failure and increase load-bearing capacity [152], [153]. To achieve uniform stress distribution in PVEH, we have adopted a uniform strength cantilever beam of varying thickness

and uniform width. Figure 4.4 (a) shows the side view of the cantilever beam, and Figure 4.4 (b) shows the 3D view.

In Figure 4.4 (a), $h(x)$ is the beam thickness at any arbitrary point along the length, and h_0 is the thickness of the beam at the fixed end. For a thickness varying beam, the stress at any point on the beam surface can be written as

$$T(x) = \frac{h_x}{2}\frac{M(x)}{I(x)} \tag{4.9}$$

where h_x is the thickness of the beam. The cross-section moment of inertia can be written as

$$I(x) = \frac{bh_x^3}{12} \tag{4.10}$$

where b is the width of the beam. Thus, the stress can be written as

$$T(x) = \frac{6F(L-x)}{bh_x^2} \tag{4.11}$$

And stress on the beam surface at $x = 0$ (fixed end) can be written as

$$T(x=0) = \frac{6FL}{bh_0^2} \tag{4.12}$$

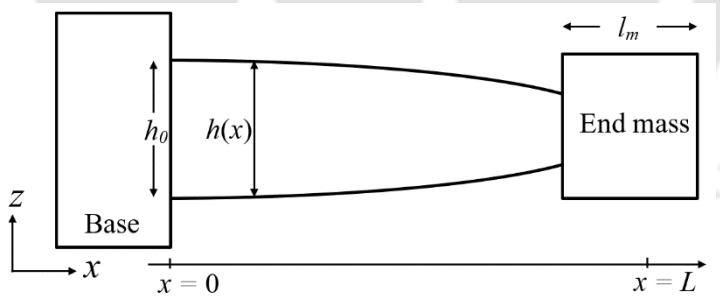

(a)

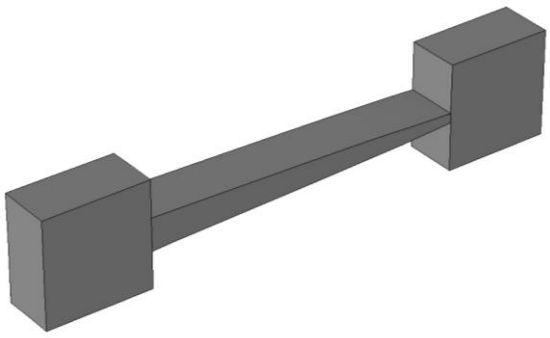

(b)

Figure 4.4: (a) side view, and (b) 3D view of the thickness-tapered cantilever beam.

If we equate (4.11) and(4.12), we get the relationship between h_0 and $h(x)$ for uniform stress profile as

$$h(x) = \sqrt{\frac{(L-x)}{L}}\, h_0 \tag{4.13}$$

It is clear that the thickness should vary according to (4.13) to achieve uniform stress distribution along the length. This thickness profile is the basis for the design of the proposed PVEH introduced in the next section.

The FE analysis of a conventional cantilever of uniform cross-section and a thickness-tapered cantilever as proposed in the above section is carried out to observe variations in stress profiles along the beam length. Figure 4.5 (a) shows the stress distribution on a conventional cantilever with uniform thickness and Figure 4.5 (b) shows the stress distribution on a thickness-tapered cantilever for identical load conditions.

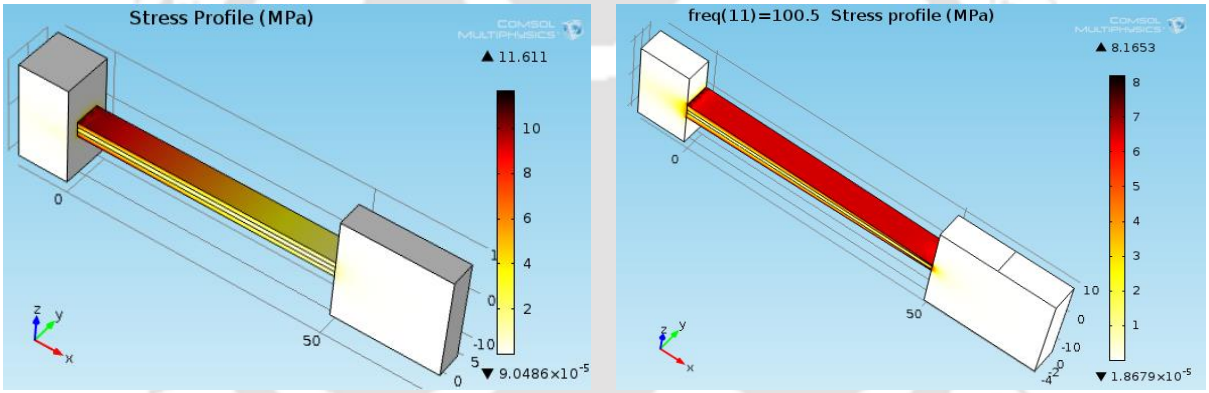

(a) (b)

Figure 4.5: Stress distribution on (a) conventional and (b) thickness-tapered cantilever from FE simulation

The above plots show that the stress on the conventional cantilever of uniform cross-section is concentrated at the fixed end of the beam while it is well distributed on the thickness-tapered beam.

4.4 DESIGN OF PVEH WITH UNIFORM STRESS

Based on the uniform strength cantilever discussed above, two PVEH geometries are proposed. In the first approach (PVEH-1), the substrate layer thickness is varied while keeping the thickness of piezoelectric layers uniform, and in the second approach (PVEH-2), the substrate layer thickness is kept uniform while the thickness of piezoelectric layers is varied. In both the geometries, the overall thickness is maintained according to (4.13).

4.4.1 PVEH-1 (Thickness-tapered substrate)

This geometry consists of a substrate layer with a tapered thickness and two piezoelectric layers of uniform thickness. The end-mass is fixed to the free end and the input excitation is applied to the base. The side view of PVEH-1 is shown in Figure 4.6. The width (along *y*-axis) of the cantilever is kept uniform along the length. The detailed analysis of PVEH-1 is carried out in chapter-5.

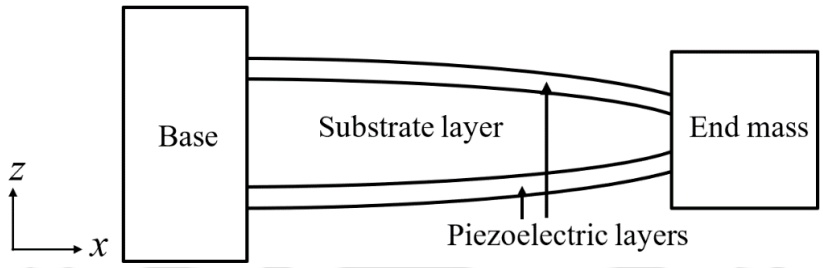

Figure 4.6: Side view of the PVEH-1 geometry.

4.4.2 PVEH-2 (Thickness-tapered piezoelectric layer)

This geometry consists of a substrate layer with uniform thickness and two piezoelectric layers of tapered thickness. The end-mass is fixed to the free end and the input excitation is applied to the base. The side view of PVEH-2 is shown in Figure 4.7. The width (along *y*-axis) of the cantilever is kept uniform along the length. The detailed analysis of PVEH-2 is carried out in chapter-6.

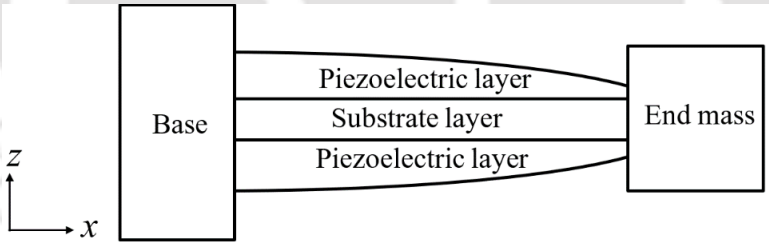

Figure 4.7: Side view of the PVEH-2 geometry.

4.5 CONCLUSIONS

The thickness profile of the conventional cantilever is modified to obtain uniform stress distribution on the beam surface. The modified thickness profile is used to introduce two new PVEH geometries. The first proposed geometry consists of a thickness-tapered substrate layer sandwiched between two piezoelectric layers of uniform thickness, discussed in detail in the next chapter. The second proposed geometry consists of a uniform substrate layer sandwiched between two piezoelectric layers of tapered thickness, discussed in detail in chapter-6.

CHAPTER 5

ANALYSIS OF PVEH-1 (THICKNESS-TAPERED SUBSTRATE)

The previous chapter proposes two new thickness-tapered geometries to obtain uniform stress distribution on the surface of cantilever-based PVEH. The geometries consist of a substrate layer sandwiched between two piezoelectric layers and an end-mass attached to the free end. The first geometry consists of a substrate layer with a tapered thickness and two piezoelectric layers of uniform thickness and is named PVEH-1, and the second geometry consists of a substrate layer with uniform thickness and two piezoelectric layers of tapered thickness and is named PVEH-2. The width, across the length, is uniform in both the PVEH.

The main contribution of this chapter is that, analytical expressions are derived for resonance frequency, end-mass displacement, stress profile on the surface, and generated power for PVEH-1. In addition, FE analysis is carried out and the results are compared with the results from the derived analytical expressions. The performance of the proposed PVEH-1 is also compared with an equivalent conventional PVEH of uniform thickness.

5.1 Derivation of analytical expressions for PVEH-1

The geometry of PVEH-1 consists of a substrate layer with a tapered thickness and two piezoelectric layers of uniform thickness. The end-mass is fixed to the free end, and the input excitation is applied to the base.

5.1.1 Geometry and assumptions

The side view of PVEH-1 geometry is shown in Figure 5.1. The cantilever's width (along y-axis) is kept uniform. The overall thickness of the cantilever beam $h(x)$ is the summation of the thickness $h_s(x)$ of the substrate layer and thickness h_p of two piezoelectric layers, and the length of the piezoelectric layer is L_p. The top and bottom sides of the piezoelectric layers are metalized

to form electrodes that are used to connect an external resistive load. The end-mass length is l_m and is attached to the free end of the beam.

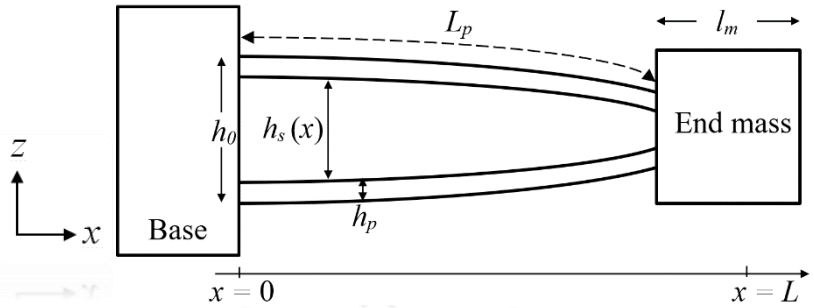

Figure 5.1: Side view of the PVEH-1.

The effective length L is the distance from the base to the center of the end-mass. The cross-section view of the beam is shown in Figure 5.2, and it consists of two piezoelectric layers of uniform thickness h_p and a thickness-tapered substrate of thickness $h_s(x)$. The width b is constant along the length of the beam. The parameter $h_{ps}(x)$ is the distance between the center of the piezoelectric layer from the beam's neutral axis (NA).

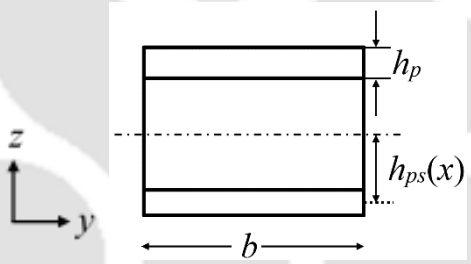

Figure 5.2: Cross-section view of the beam.

As described in (4.13), $h(x)$ is the overall thickness of the beam. Thus, the varying substrate layer thickness $h_s(x)$ can be written as

$$h_s(x) = h(x) - 2h_p \tag{5.1}$$

The input excitation is applied in the z-direction to the base at $x = 0$. When the input excitation frequency is near the cantilever's resonance frequency, the end-mass starts oscillating in the z-direction and exerts stress on the cantilever beam in the x-direction. The stress on the piezoelectric material generates an electrical voltage across the connected load resistance.

5.1.2 Derivation of spring constant and resonance frequency

The resonance frequency of the PVEH-1 is derived using the Euler-Bernoulli beam equation given by [74], [151]

$$\frac{d^2z(x)}{dx^2} = \frac{M(x)}{YI(x)} \tag{5.2}$$

where $z(x)$ is the beam displacement at any point x along the length due to the moment $M(x)$, and $YI(x)$ is the stiffness of the cantilever beam. Solving the second-order differential equation (5.2) yields the beam deflection equation.

The moment $M(x)$ of the beam due to the end-mass motion can be written as [151]

$$M(x) = F(L - x) \tag{5.3}$$

where F is the force at $x = L$ due to the motion of the end-mass, the stiffness of the thickness-tapered composite beam can be written as [84]

$$YI(x) = \frac{Y_p b h^3(x)}{12} + (Y_s - Y_p)\frac{b h_s^3(x)}{12} \tag{5.4}$$

where Y_s and Y_p are Young's moduli of the substrate material and piezoelectric material, respectively, and b is the uniform width of the beam. Using (5.3) and (5.4), the beam equation (5.2) can be rewritten as

$$\frac{d^2z(x)}{dx^2} = \frac{F(L-x)}{\frac{Y_s b h_0^3}{12L^{3/2}}(L-x)^{3/2} - b(Y_s - Y_p)\left[\frac{2}{3}h_p^3 + \frac{h_p h_0^2 (L-x)}{2L} - h_p^2 h_0\sqrt{\frac{L-x}{L}}\right]} \tag{5.5}$$

The differential equation (5.5) is the expanded form of (5.2) representing the Euler-Bernoulli beam equation for the thickness-tapered cantilever beam. The term h_p^3 in the denominator is negligible compared to the other terms and can be ignored for simplicity. Thus, the above equation reduces to

$$\frac{d^2z(x)}{dx^2} = \frac{F(L-x)}{\frac{Y_s b h_0^3}{12L^{3/2}}(L-x)^{3/2} - b(Y_s - Y_p)\left[\frac{h_p h_0^2 (L-x)}{2L} - h_p^2 h_0\sqrt{\frac{L-x}{L}}\right]} \tag{5.6}$$

Solving (5.6) for an applied force F at $x = L$ yields the displacement $z(x)$ along the length. As the cantilever is a mechanical spring, the beam's spring constant (k) can be expressed as the ratio of applied force F and the resultant displacement z at $x = L$. The beam equation (5.6) is solved in MATLAB for a unit force, and the spring constant k is calculated. From the spring constant obtained above, the resonance frequency ω_n of the energy harvester is expressed as

$$\omega_n = \sqrt{\frac{k}{m_e}} = \sqrt{\frac{k}{(33/140)m + M_t}} \tag{5.7}$$

where m_e is the effective mass of the cantilever represented by $(33/140)m + M_t$, where m is the mass of the beam and M_t is the mass of the end-mass [97].

5.1.3 Stress on the piezoelectric material

The end-mass motion exerts stress on the cantilever beam, and the stress is maximum on the top surface and gradually decreases towards the beam's neutral axis. The piezoelectric material on the PVEH experiences maximum stress on the outer surface and reduced stress on the inner surface.

Therefore the stress on the piezoelectric layer along the length x due to the moment $M(x)$ can be written as [74]

$$T(x) = \frac{M(x)}{I(x)} h_{ps}(x) \tag{5.8}$$

and the average stress on the piezoelectric material can be written as

$$T = \frac{1}{L_p} \int_0^{L_p} \frac{M(x)}{I(x)} h_{ps}(x)\, dx \tag{5.9}$$

where $I(x)$ is the cross-sectional moment of inertia of the composite beam and $h_{ps}(x)$ is the distance of the center of the piezoelectric layer from the *NA* as shown in Figure 5.2 and are respectively given as follows.

$$I(x) = \frac{bh^3(x)}{12} + (\eta - 1)\frac{bh_s^3(x)}{12} \tag{5.10}$$

$$h_{ps}(x) = \frac{h(x)}{2} - \frac{h_p}{2} \tag{5.11}$$

where η is the ratio of Young's moduli of the substrate and the piezoelectric material. For a sinusoidal input excitation of frequency ω, the end-mass motion will also be periodic, and hence the force and end-mass displacement will be a function of time given as

$$F(t) = kz(t) \tag{5.12}$$

where $z(t)$ is the displacement of the end-mass. Thus, the average stress as a function of time can be written as

$$T(t) = \frac{1}{L_p} \int_0^{L_p} \frac{(L-x)kz(t)}{\frac{bh^3(x)}{12} + (\eta - 1)\frac{bh_s^3(x)}{12}} \left[\left(\sqrt{\frac{L-x}{L}} \right) \frac{h_0}{2} - \frac{h_p}{2} \right] dx \tag{5.13}$$

Equation (5.13) defines the instantaneous average stress on the piezoelectric material due to the end-mass displacement $z(t)$, and it can be rewritten as

$$T(t) = z(t)\Gamma \tag{5.14}$$

where Γ is given by

$$\Gamma = \frac{1}{L_p}\int_0^{L_p} \frac{(L-x)k}{\frac{bh^3(x)}{12} + (\eta - 1)\frac{bh_s^3(x)}{12}}\left[\left(\sqrt{\frac{L-x}{L}}\right)\frac{h_0}{2} - \frac{h_p}{2}\right] dx \tag{5.15}$$

Note that Γ depends on the composite cantilever's dimension and material properties and not on the input excitation condition.

5.1.4 Derivation of coupled equations

The generated voltage across the piezoelectric layer results from stress on the material. The end-mass motion in the z-direction exerts stress on piezoelectric material in the x-direction. The piezoelectric material is poled in the z-direction, which is the direction of the input vibration. Therefore, the plain stress form of the piezoelectric constitutive equations can be written as [91], [154]

$$D = d_{31}T_1 + \varepsilon_{33}^T E_3 \tag{5.16}$$

where T_1 is the average stress along the length and is given by (5.13), E_3 is electric field across the piezoelectric layer, D_3 is electric displacement, d_{31} is the piezoelectric charge constant which relates generated charge density per unit stress and ε_{33}^T is permittivity of the piezoelectric material at constant stress. The subscripts 1 and 3 denote the direction along which a particular parameter is measured. The generated charge q due to stress T can be written using (5.16) as

$$q = L_p b\left(d_{31}T - \varepsilon_{33}^T \frac{v}{h_p}\right) \tag{5.17}$$

where L_p and b represent the piezoelectric layer's length and width, respectively. The term v represents the voltage across the piezoelectric layer of thickness h_p. When a time-varying sinusoidal excitation is applied to the base, the current $i(t)$ can be written as

$$i(t) = \frac{dq}{dt} \tag{5.18}$$

$$i(t) = L_p b d_{31}\Gamma\frac{dz(t)}{dt} - \frac{L_p b\varepsilon_{33}^T}{h_p}\frac{dv(t)}{dt} \tag{5.19}$$

When an external load resistance R is connected across the electrodes, the current through the load resistance can be written as

$$\frac{v(t)}{R} = L_p b d_{31} \Gamma \frac{dz(t)}{dt} - \frac{L_p b \varepsilon_{33}^T}{h_p} \frac{dv(t)}{dt} \tag{5.20}$$

$$\frac{v(t)}{R} + C_p \frac{dv(t)}{dt} = \theta \frac{dz(t)}{dt} \tag{5.21}$$

Equation (5.21) is the electrical equation for the piezoelectric layer, where C_p represents the capacitance of the piezoelectric layers and θ represents the electromechanical coupling coefficient of the piezoelectric layer.

$$C_p = \frac{\varepsilon_{33}^T b L_p}{h_p} \tag{5.22}$$

$$\theta = d_{31} b L_p \Gamma \tag{5.23}$$

The mechanical equation of the PVEH can be derived using the spring-mass-damper system shown in Figure 5.3, where b_m represents mechanical damping coefficient, $x(t)$ is the absolute displacement of the mass due to input excitation $y(t)$, and θ is the damping due to electromechanical coupling.

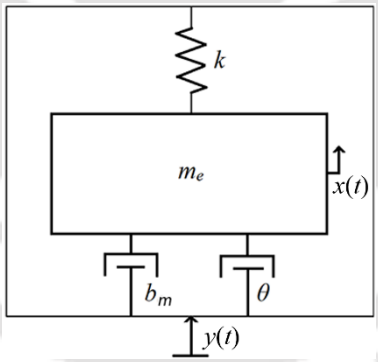

Figure 5.3: Equivalent spring-mass-damper model of an energy harvester.

The equation of motion of the mass relative to the base displacement can be written as [136]

$$\frac{d^2 z(t)}{dt^2} + 2\zeta_m \omega_n \frac{dz(t)}{dt} + \omega_n^2 z(t) + \frac{\theta}{m_e} v(t) = \frac{d^2 y(t)}{dt^2} \tag{5.24}$$

where $z(t)$ is the relative displacement of the mass given by $z(t) = x(t) - y(t)$, ω_n is the resonance frequency of vibration, m_e is the effective mass of the cantilever, ζ_m is the mechanical damping ratio, and $y(t)$ represents input excitation amplitude at the base. Equations (5.21) and (5.24) are the coupled equations of the proposed PVEH-1. In bimorph PVEH, both the piezoelectric layers can be wired in series connection or parallel connection.

5.1.5 Parallel connection of piezoelectric layers

The polarity of the generated voltage on the piezoelectric layers depends on the poling direction of the piezoelectric material and the direction of applied stress. For a bimorph PVEH, if the upper piezoelectric layer experiences tensile stress, the lower piezoelectric layer will experience compressive stress. Consequently, the generated electrical fields on the two piezoelectric layers are in opposite directions. In a parallel connection, both the piezoelectric layers are connected in parallel. The piezoelectric capacitance and the piezoelectric coupling coefficient double due to the parallel connection of two piezoelectric layers. Thus (5.21) and (5.24) can be written as

$$v(t) + 2RC_p\frac{dv(t)}{dt} - 2\theta R\frac{dz(t)}{dt} = 0 \tag{5.25}$$

$$\frac{d^2z(t)}{dt^2} + 2\zeta_m\omega_n\frac{dz(t)}{dt} + \omega_n^2 z(t) + \frac{2\theta}{m_e}v(t) = \frac{d^2y(t)}{dt^2} \tag{5.26}$$

Equations (5.25) and (5.26) are the coupled equations for the proposed thickness-tapered PVEH-1 for parallel-connected piezoelectric layers. Solving (5.25) and (5.26) for displacement $z(t)$ and generated voltage $v(t)$, the generated electrical power can be calculated. When the energy harvester is excited with a sinusoidal excitation of angular frequency ω and peak amplitude Y_0 at the base, the solution for the above equations can be written as

$$z(t) = -\frac{m_e\omega^2 Y_0\left(1 + j2RC_p\omega\right)}{\left(\omega_n^2 - \omega^2 + j2\zeta_m\omega\omega_n\right)\left(m_e + j2m_eRC_p\omega\right) + j4R\theta^2\omega}e^{j\omega t} \tag{5.27}$$

$$v(t) = -\frac{2jR\theta m_e\omega^3 Y_0}{\left(\omega_n^2 - \omega^2 + j2\zeta_m\omega\omega_n\right)\left(m_e + j2m_eRC_p\omega\right) + j4R\theta^2\omega}e^{j\omega t} \tag{5.28}$$

The above analytical expressions are useful in estimating electrical power transferred to the resistive load due to the mechanical motion of the energy harvester.

5.1.6 Series connection of piezoelectric layers

When both the piezoelectric layers are connected in series, the equivalent capacitance of the PVEH becomes half of the capacitance of a single piezoelectric layer. For series connection, the coupled equation of the PVEH can be written as

$$2v(t) + RC_p\frac{dv(t)}{dt} - 2R\theta\frac{dz(t)}{dt} = 0 \tag{5.29}$$

$$\frac{d^2z(t)}{dt^2} + 2\zeta_m\omega_n\frac{dz(t)}{dt} + \omega_n^2 z(t) + \frac{\theta}{m_e}v(t) = \frac{d^2y(t)}{dt^2} \tag{5.30}$$

Equations (3.21) and (5.30) are the coupled equations for the proposed thickness-tapered PVEH-1 for series-connected piezoelectric layers. Solving (3.21) and (5.30) for displacement $z(t)$ and generated voltage $v(t)$, the generated electrical power can be calculated. When the energy harvester is excited with a sinusoidal excitation of angular frequency ω and peak amplitude Y_0 at the base, the solution for the above equations can be written as

$$z(t) = -\frac{m_e\omega^2 Y_0\left(2 + jRC_p\omega\right)}{\left(\omega_n^2 - \omega^2 + j2\zeta_m\omega\omega_n\right)\left(2m_e + jm_eRC_p\omega\right) + j2R\theta^2\omega} e^{j\omega t} \tag{5.31}$$

$$v(t) = -\frac{j2m_e\omega^3 R\theta Y_0}{\left(\omega_n^2 - \omega^2 + j2\zeta_m\omega\omega_n\right)\left(2m_e + jm_eRC_p\omega\right) + j2R\theta^2\omega} e^{j\omega t} \tag{5.32}$$

The above analytical expressions can be used to compute end-mass displacement and the corresponding voltage across a resistive load R.

5.2 GEOMETRICAL AND MATERIAL PROPERTIES OF PVEH-1

The detailed dimensions of the energy harvester used in the simulation are shown in Table 5.1. All calculations are performed for a constant input acceleration of $0.2g$ or 1.96 m/s^2 and a mechanical damping ratio of 0.01. The piezoelectric material considered in all the simulations is PZT-5H, and for this material $d_{31} = -274 \times 10^{-12}$ C/N and $\varepsilon_{33}^T = 30.104 \times 10^{-9}$ F/m. [155].

Table 5.1: Geometric and material parameters of the simulated PVEH-1.

Parameter	Description	Value
L	Beam length	50.00 mm
b	Beam width, end-mass width	5.00 mm
h_s	Substrate thickness at the base	2.50 mm
h_p	Piezoelectric layer thickness	0.25 mm
l_m	Length and height of end-mass	20.00 mm
Y_p	Young's modulus of the piezoelectric material	60.60 GPa
Y_s	Young's modulus of the substrate (Brass)	110.00 GPa
ρ_p	Piezoelectric material (PZT-5H) density	7500 kg/m^3
ρ_s	Substrate material density	9000 kg/m^3
ρ_m	End-mass material density	9000 kg/m^3

The derived analytical expressions are solved in MATLAB using the specifications mentioned in Table 5.1. An FE model is also developed and studied to compare the analytical results. The

3D view of the proposed PVEH-1 developed for FE analysis in COMSOL Multiphysics is shown in Figure 5.4.

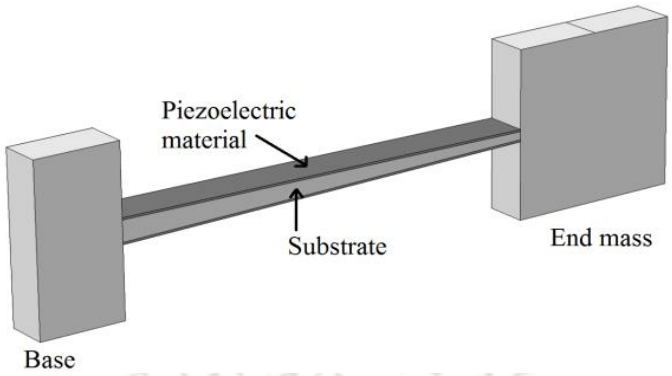

Figure 5.4: Geometry of PVEH-1 simulated in COMSOL Multiphysics.

5.3 RESULTS FROM THE DERIVED ANALYTICAL EXPRESSIONS

The analytical expressions derived for the parallel connected piezoelectric layers are solved using MATLAB, and results are obtained for the resonance frequency of vibration, end-mass displacement, generated power, and stress profile on the surface. In the following sections, all the results are discussed in detail.

5.3.1 Calculation of resonance frequency

The resonance frequency for the PVEH-1 mentioned above is calculated using (5.7). Piezoelectric materials exhibit lower stiffness in short-circuit conditions and higher stiffness in open-circuit conditions [156]. Thus, the resonance frequency in the open-circuit condition is higher than the short-circuit condition. In this study, the default resonance frequency mentioned is for the short-circuit condition. The resonance frequency found from the derived expression is 99.8 Hz and from FE analysis is 99.7 Hz. Figure 5.5 shows the first vibration mode shape of the PVEH-1.

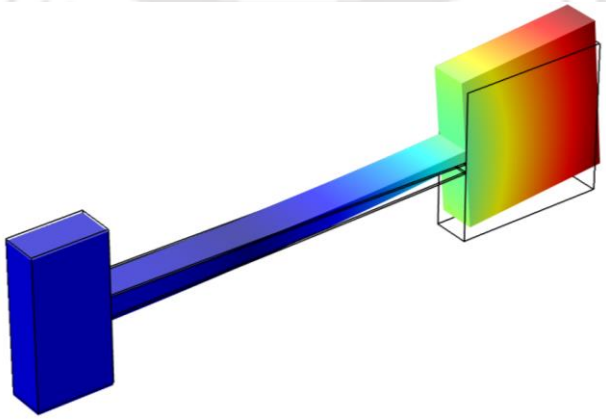

Figure 5.5: First vibration mode shape of PVEH-1.

5.3.2 Variation of end-mass displacement with load resistance

The end-mass displacement due to input base excitation is maximum near the resonance frequency. The end-mass displacement decreases as the excitation frequency moves away from the system resonance frequency. The load resistance also influences the PVEH's end-mass displacement. Figure 5.6 shows the variations of resonance frequency and end-mass displacement with load resistance for an input sinusoidal acceleration of 0.2*g*. As the load resistance increases from a lower value to a very high value, the end-mass displacement varies and two peaks are observed as shown in Figure 5.6. The first peak at 99.8 Hz corresponds to the short-circuit resonance frequency, and the second at 102.8 Hz corresponds to the open-circuit resonance frequency.

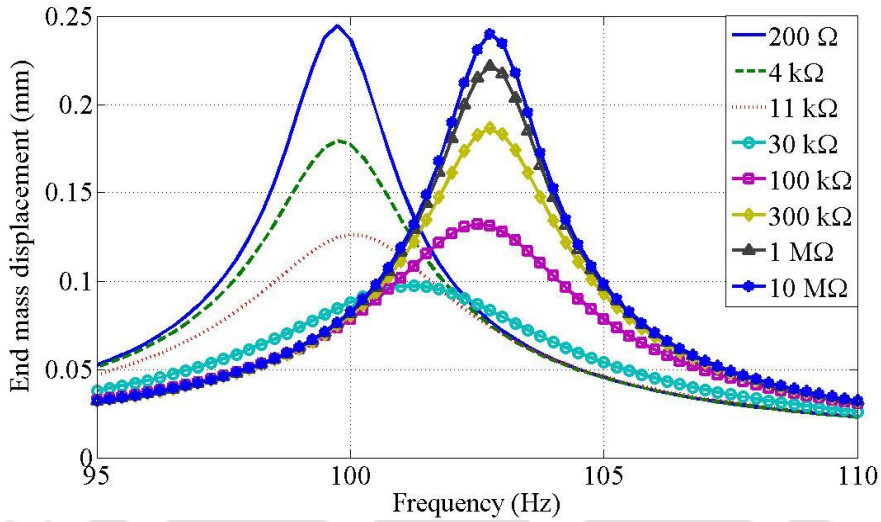

Figure 5.6: Plot of end-mass displacement versus frequency for various load resistance values.

5.3.3 Variation of electrical power with load resistance

The PVEH generates an electrical voltage across the connected load resistance due to stress on it, and the power is calculated as the product of current through the load resistor and voltage across it. Figure 5.7 shows the variation of electrical power for various load resistances obtained from the derived analytical expressions.

As shown in Figure 5.7, the generated electrical power depends on the connected load resistance, and the load resistance value for which the PVEH generates the highest power is called optimal load resistance. The above analysis found that the optimal load resistance is 11 kΩ when the PVEH is excited with the short-circuit resonance frequency.

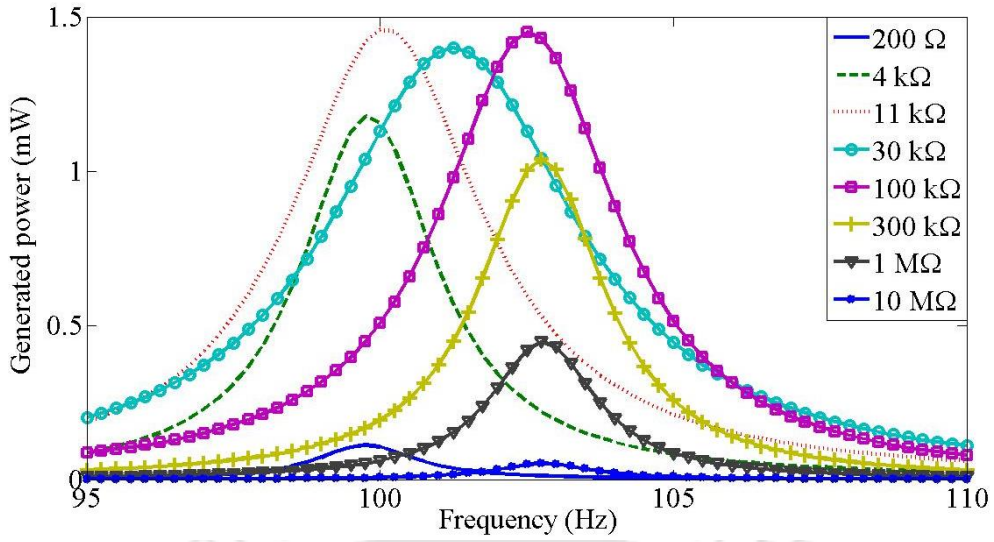

Figure 5.7: Plot of power versus frequency for various load resistance values.

5.4 COMPARISON OF ANALYTICAL RESULTS WITH FE ANALYSIS

An FE model of conventional bimorph PVEH is developed in chapter-2 using COMSOL Multiphysics software. Using the same methodology, an FE model for PVEH-1 is developed, and a sinusoidal input of constant acceleration of $0.2g$ is applied at the base. The PVEH is simulated to obtain the end-mass displacement, generated power, and stress profile on the piezoelectric material.

5.4.1 Comparison of end-mass displacement

The end-mass displacement of the PVEH-1 is calculated using (5.31) for the short-circuit condition and plotted against input frequency in Figure 5.8 (a). The end-mass displacement for the same PVEH obtained from FE analysis is also plotted in Figure 5.8 (b). The analytical result

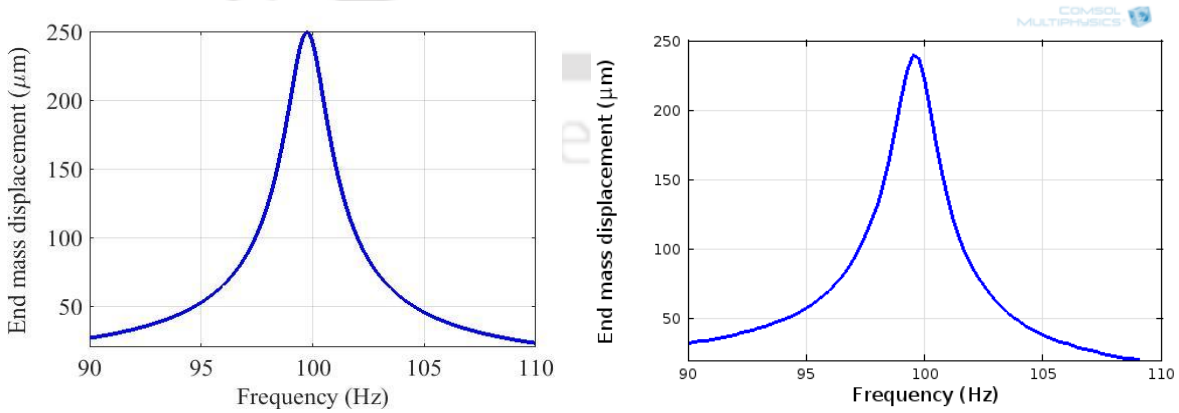

(a) (b)

Figure 5.8: Plot of end-mass displacement versus frequency at short-circuit condition from (a) the derived analytical expression and (b) FE analysis.

shows that the peak value of end-mass displacement is 249 μm at 99.8 Hz frequency, and the result from the FE analysis shows that the peak value of end-mass displacement is 242 μm at 99.7 Hz frequency. FE results are consistent with the analytical results.

When the optimal load resistance (11 kΩ) is connected to the PVEH-1, the plots of end-mass displacement from the analytical result and FE analysis are shown in Figure 5.9 (a) and Figure 5.9 (b), respectively.

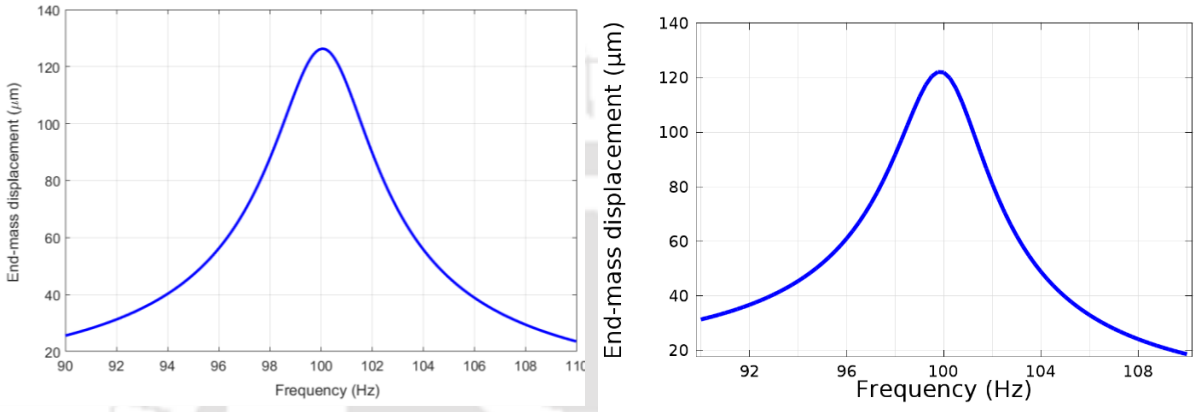

(a) (b)

Figure 5.9: Plot of end-mass displacement versus frequency at optimal load from (a) the derived analytical expression and (b) FE analysis.

5.4.2 Comparison of generated power at optimal load resistance

As shown in Figure 5.7, the electrical power depends on the connected load resistance, and to harvest maximum power, the load resistance should be of optimal value. The load resistance value for which the PVEH generates the highest power is called optimal load resistance. Figure 5.10 (a) and Figure 5.10 (b) show the plots of the generated power at optimal load resistance obtained using the derived analytical expression and FE simulation, respectively.

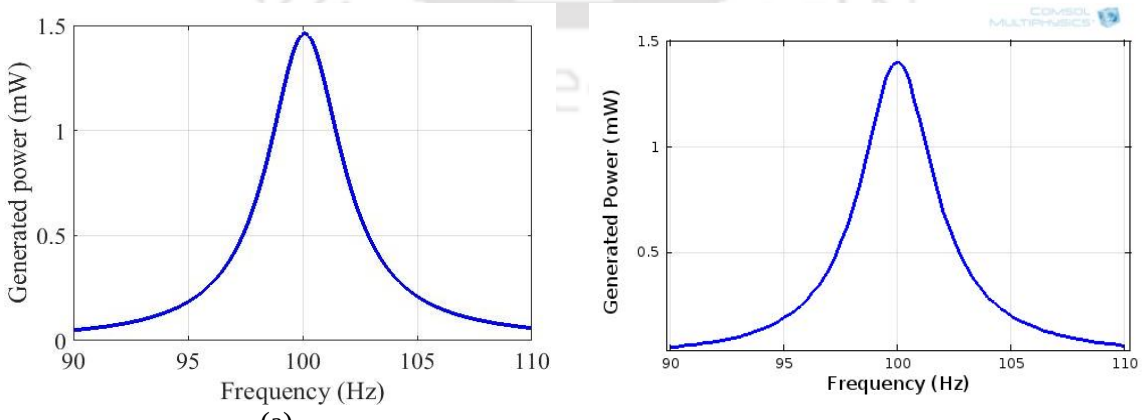

(a) (b)

Figure 5.10: Plot of power versus frequency at optimal load obtained from (a) analytical expression and (b) FE analysis.

5.4.3 Comparison of the stress profile

The end-mass of the cantilever oscillates due to the applied base excitation, and this oscillation produces stress on the piezoelectric material. The stress on the beam surface of the proposed PVEH is uniform in nature which significantly increases the device reliability. The stress profile of the proposed PVEH-1 is shown in Figure 5.11 (a) and Figure 5.11 (b), respectively, from the analytical solution and FE analysis results. The stress profiles are for the input excitation at 100 Hz frequency with 0.2g acceleration. The stress on the piezoelectric material is uniformly distributed along the entire length. This kind of distribution reduces the peak stress on the piezoelectric material and at the same time, raises the average stress on the piezoelectric material.

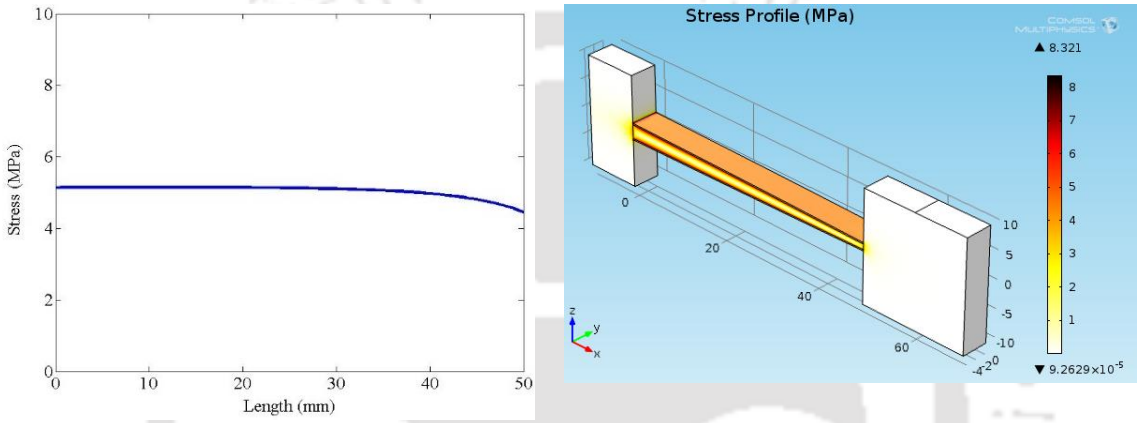

Figure 5.11: Stress distribution along the length obtained from (a) analytical result and (b) FE analysis.

Table 5.2 summarizes the results from the derived analytical solution and FE analysis of the proposed PVEH. From the table, it is clear that the results from the derived analytical model are close to the results from FE analysis. In the next section, the proposed thickness-tapered PVEH-1 is compared with an equivalent conventional PVEH having a uniform thickness.

Table 5.2: Comparison of results using the analytical expressions and FE analysis.

Parameters	**MATLAB result by solving derived analytical expressions**	**Results from FE analysis**
Natural frequency of vibration	99.80 Hz	99.70 Hz
Open-circuit natural frequency of vibration	102.80 Hz	102.75 Hz
End-mass displacement at short-circuit	249 μm	242 μm
End-mass displacement at optimal load	126.20 μm	121.50 μm
Generated power at optimal load 11 kΩ	1.46 mW	1.40 mW
Maximum stress at optimal load	5.14 MPa	5.15 MPa

5.5 COMPARISON WITH CONVENTIONAL PVEH

The conventional PVEH refers to the cantilever-based PVEH with a uniform cross-section throughout the length. In the equivalent conventional PVEH, the thickness of the substrate layer is set as the average substrate thickness of the proposed energy harvester that is 1.812 mm. The piezoelectric layer thickness and the width of the conventional energy harvester beam are equal to that of the proposed energy harvester. Analytical expressions are derived for conventional PVEH with uniform thickness in chapter-3 and are used herein to evaluate the performance of the equivalent conventional PVEH.

The equivalent energy harvester's resonance frequency is kept the same (100 Hz) as the proposed PVEH-1 by adjusting the end-mass. All the parameters of the equivalent conventional PVEH are shown in Table 5.3. The end-mass for the equivalent conventional energy harvester is 15.18 grams, whereas the thickness-tapered energy harvester is 17.9 grams. Both the energy harvesters are excited with a constant acceleration of $0.2g$ (1.96 m/s^2), and their responses are recorded. Figure 5.12 shows the schematic diagram of the equivalent conventional PVEH with a uniform cross-section area.

Table 5.3: Geometrical and material parameters of the equivalent conventional PVEH.

Parameter	Description	Value
L	Beam length	50.00 mm
b	Beam width, end-mass width	5.00 mm
h_s	Thickness of substrate layer	1.812 mm
h_p	Thickness of Piezoelectric layer	0.25 mm
l_m	Length and height of end-mass	18.20 mm
Y_p	Young's modulus of the piezoelectric material	60.60 GPa
Y_s	Young's modulus of the substrate material	110.00 GPa
ρ_p	piezoelectric material (PZT-5H) density	7500 kg/m^3
ρ_s	Substrate material density	9000 kg/m^3
ρ_m	End-mass material density	9000 kg/m^3

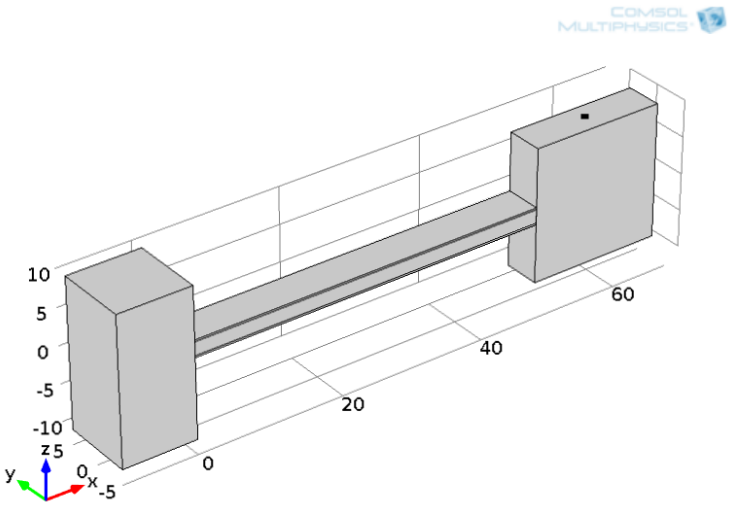

Figure 5.12: Geometry of the equivalent conventional PVEH.

5.5.1 Comparison of the end-mass displacement

The proposed PVEH-1 and the equivalent conventional PVEH are excited with the same input acceleration, i.e., 0.2*g* at their respective bases, and their performances are compared. The displacements of the end-mass for both the devices are measured when optimal load resistances are connected. Figure 5.13 compares the end-mass displacement of the proposed PVEH-1 and its equivalent conventional PVEH, which are 126.2 μm and 124 μm, respectively.

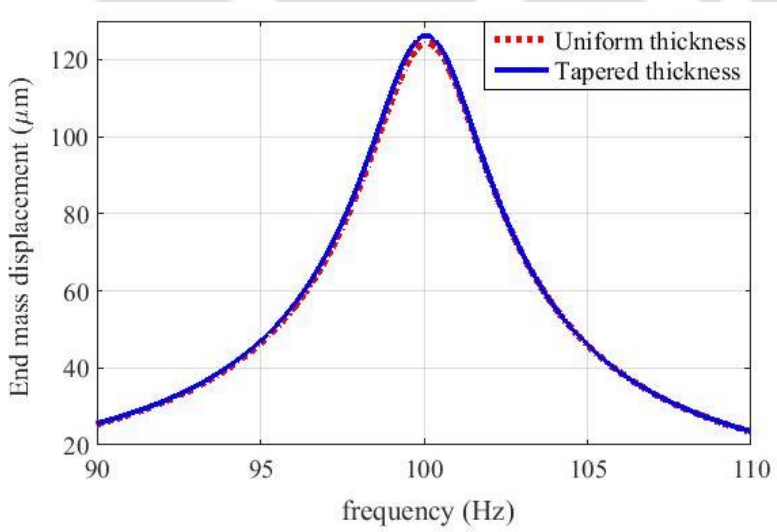

Figure 5.13: Comparison of end-mass displacements of PVEH-1 (tapered thickness) and conventional PVEH (uniform thickness).

5.5.2 Comparison of the stress profiles

Figure 5.14 (a) and (b) show the stress distribution along beam length for the proposed PVEH-1 and conventional PVEH, respectively, for an acceleration of 0.2*g* (1.96 m/s^2) at 100 Hz

frequency. The solid line represents the actual stress value on the piezoelectric material, whereas the dotted line represents the average stress on the piezoelectric material. FE analyses of the proposed PVEH-1 and its equivalent uniform thickness energy harvester are carried out, and their 3D view of stress distribution is shown in Figure 5.15 (a) and (b), respectively.

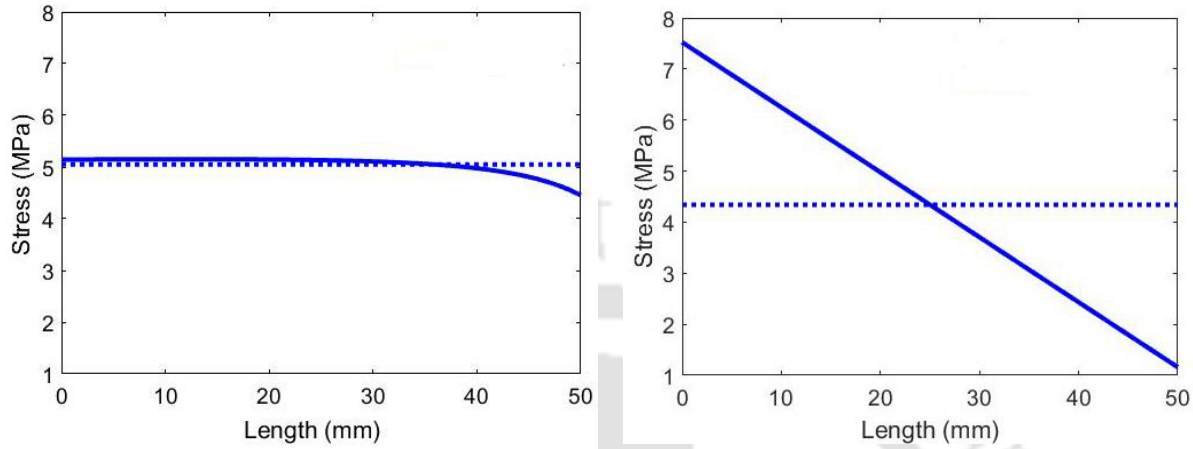

(a) (b)

Figure 5.14: Comparison of stress distributions along the length of (a) proposed PVEH-1 and (b) conventional PVEH.

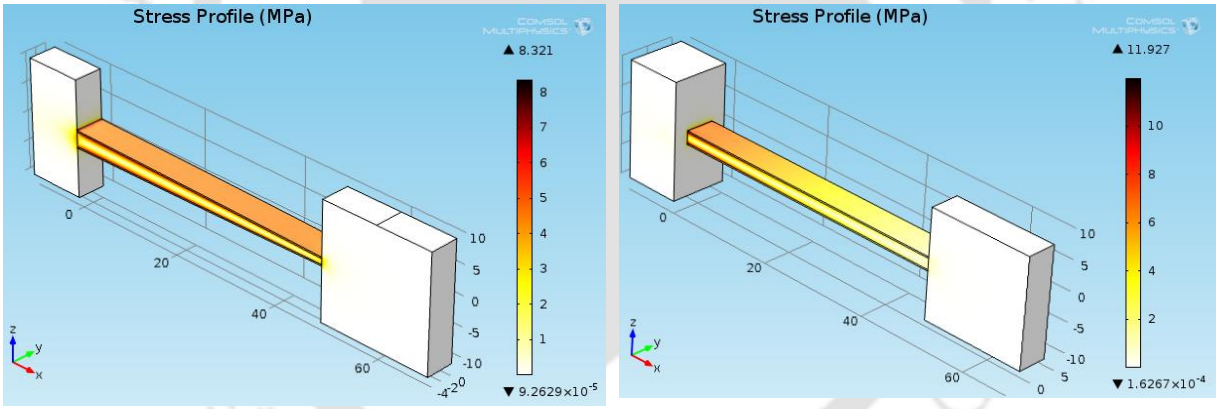

(a) (b)

Figure 5.15: 3-D views of stress distribution on (a) proposed PVEH-1 and (b) conventional PVEH.

The conventional PVEH experiences the highest stress at the fixed end of the beam, whereas the proposed PVEH-1 experiences almost uniform stress along the entire length of the beam. The proposed PVEH-1 will be more reliable since the stress is well distributed along the length, and it can be used for higher input accelerations. The highest value of stress on the proposed PVEH-1 is 5.14 MPa at the fixed end of the beam, and the minimum value of stress is 4.46 MPa at the free end of the beam. On the other hand, the highest value of stress on the conventional PVEH is 7.52 MPa at the fixed end of the beam, and the minimum value of stress is 1.16 MPa at the free end of the beam. The average stress on the beam is calculated by measuring stress on fifty

different points on the beam, and it is found to be 5.05 MPa for the proposed PVEH-1 and 4.34 MPa for the conventional PVEH. Though the peak stress on the proposed PVEH-1 is significantly lower, the average stress is noticeably higher than the conventional PVEH.

5.5.3 Comparison of generated power

The power generated from the PVEH is directly proportional to the average stress on the piezoelectric material. In last section, we have seen that the proposed energy harvester experiences significantly higher average stress on the piezoelectric material, and thus it should generate higher electrical power compared to the conventional PVEH. Figure 5.16 shows generated power for optimal load resistance from the proposed PVEH-1 and equivalent uniform thickness conventional PVEH for the same input acceleration (0.2*g*). The maximum power generated is 1.46 mW and 1.22 mW from the proposed PVEH-1 and conventional PVEH, respectively. In uniform thickness PVEH, the stress reduces linearly along the length as observed in Figure 5.14 (b), and the piezoelectric material towards the free end remains underutilized. In contrast, in the proposed PVEH-1, the piezoelectric material experiences almost uniform stress and contributes equally to the energy generation process, resulting in more harvested power.

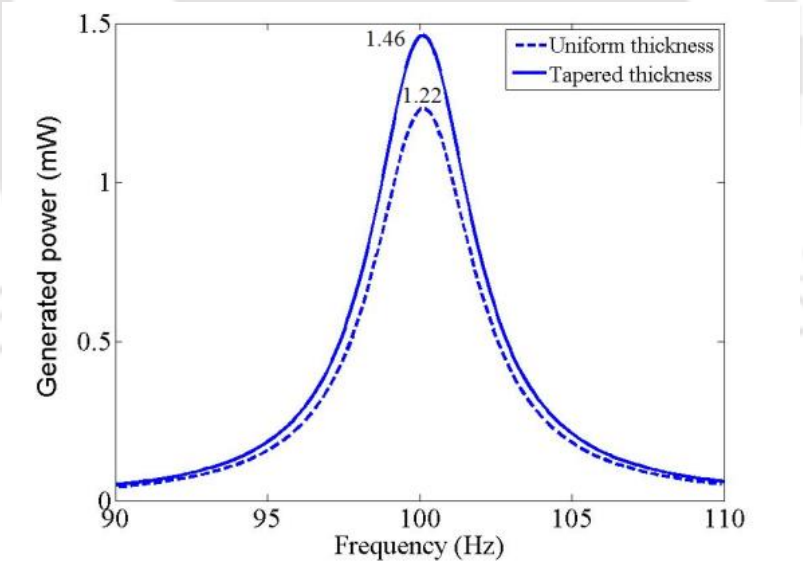

Figure 5.16: Comparison of harvested power from proposed PVEH-1 (tapered thickness) and conventional PVEH (uniform thickness).

5.5.4 Comparison of generated power at equal stress

The proposed PVEH-1 experiences less stress and generates higher power compared to the conventional PVEH for the same input conditions. The lower stress on the proposed PVEH allows the use of this energy harvester for higher input accelerations without much stress on the piezoelectric materials. In this section, both the energy harvesters are exposed to the same peak

stress value, and their performances are compared. Both conventional and proposed PVEH are excited with 100 Hz frequency such that the peak stress on the piezoelectric material is 10 MPa. To achieve the peak stress, the proposed PVEH-1 is excited with 3.81 m/s^2 acceleration, and the conventional energy harvester is excited with 2.593 m/s^2 acceleration. When both the energy harvesters are excited to 10 MPa peak stress, the average stress value on the piezoelectric material is 9.81 MPa for the proposed energy harvester, and the average stress value for the conventional energy harvester is 5.77 MPa. The stress distribution on the proposed PVEH-1 and the conventional PVEH is shown in Figure 5.17. The generated power from the proposed PVEH-1 is 5.5 mW, and from the conventional PVEH is 2.19 mW for the peak stress value of 10 MPa.

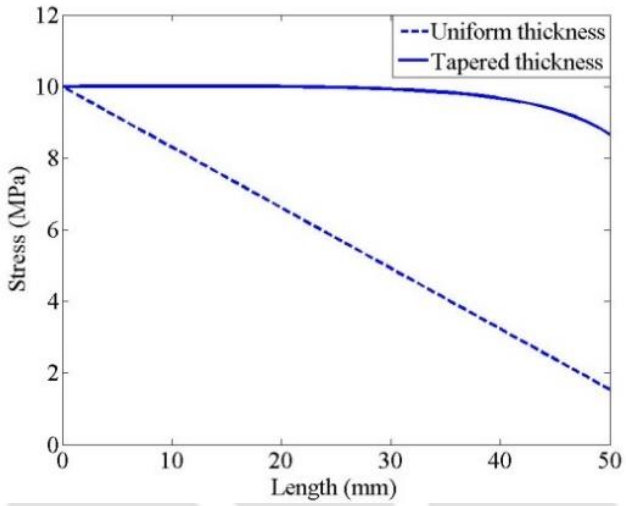

Figure 5.17: Stress profile comparison of the proposed PVEH-1 (tapered thickness) and conventional PVEH (uniform thickness) for equal peak stress of 10 MPa.

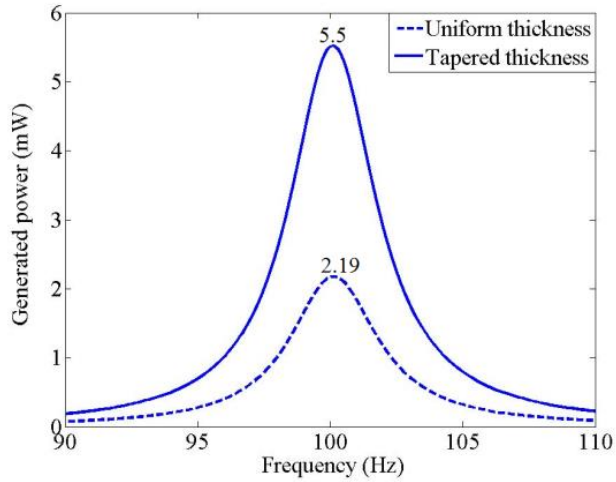

Figure 5.18: Generated power from the proposed PVEH-1 (tapered thickness) and conventional PVEH (uniform thickness) for equal peak stress of 10 MPa.

The proposed PVEH-1 shows a significant improvement in the generated power than the equivalent PVEH of uniform thickness. The summary of all the observations is given in Table 5.4 to compare both the energy harvesters quantitively.

Table 5.4: Output comparison of the proposed and conventional PVEH.

	Proposed PVEH-1	**Conventional PVEH**
Displacement of end-mass at 0.2*g* acceleration	126 μm	124 μm
Generated power at 0.2*g* acceleration	1.46 mW	1.22 mW
Maximum stress at 0.2*g* acceleration	5.14 MPa	7.56 MPa
Average stress at 0.2*g* acceleration	5.05 MPa	4.34 MPa
Generated power at 10 MPa peak stress	5.522 mW	2.190 mW

5.6 INPUT ACCELERATION AND POWER

Increasing the input acceleration significantly increases the stress on piezoelectric material and so the harvested power. Figure 5.19 and Figure 5.20 show the variation of power for different input accelerations for the PVEH-1 and corresponding conventional PVEH, respectively.

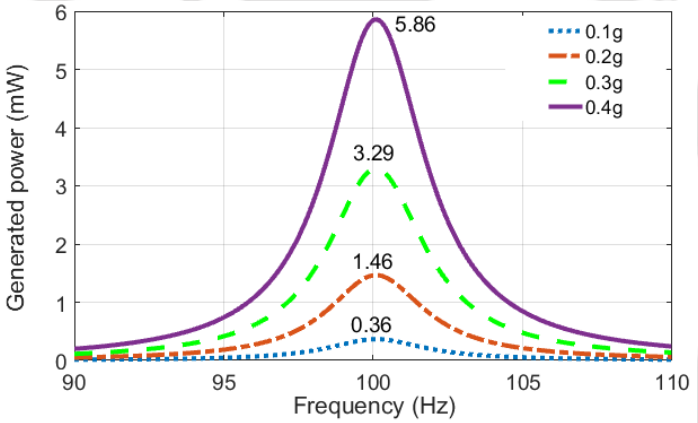

Figure 5.19: Variation of power for different input accelerations for the proposed PVEH-1.

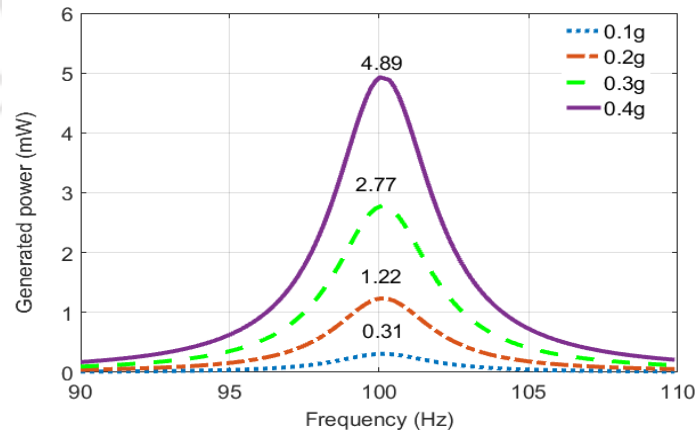

Figure 5.20: Variation of power for different input accelerations for the conventional PVEH.

Generated power and corresponding peak stress for different input accelerations are shown in Table 5.5. It is clear from the table that a two-fold increase in the acceleration results in a four-fold increase in the harvested power. Thus, using the highest input acceleration level available for a particular frequency is very important. The proposed PVEH-1 is suitable for higher

acceleration levels without compromising device reliability. It is also observed that the proposed PVEH-1 always generates 19% more power by experiencing 31.6% less stress than the equivalent conventional PVEH for the same input acceleration.

Table 5.5: Comparison of the proposed PVEH-1 and conventional PVEH at different accelerations.

Input acceleration	Proposed PVEH-1		Conventional PVEH		Increase in power (%)	Reduction in peak stress (%)
	Peak stress (MPa)	Power (mW)	Peak stress (MPa)	Power (mW)		
0.1*g*	2.57	0.36	3.76	0.31	16.13	31.65
0.2*g*	5.14	1.46	7.52	1.22	19.67	31.65
0.3*g*	7.72	3.29	11.29	2.77	18.77	31.63
0.4*g*	10.30	5.86	15.06	4.89	19.84	31.61

5.7 POWER DENSITY

The power density is calculated by dividing the harvested power by the corresponding device volume. The total volume is the summation of beam volume and end-mass volume. The proposed thickness-tapered beam and the equivalent conventional beam have equal volume. The beam volume for both the devices is 0.575 cm^3, the end-mass volume for the proposed PVEH-1 is 2.0 cm^3 and that for the conventional PVEH is 1.656 cm^3. Thus, the total volume of the proposed PVEH-1 is 2.575 cm^3 and the total volume of the conventional PVEH is 2.231 cm^3. The power density for the proposed thickness-tapered PVEH is 0.567 mW/cm^3 and for the conventional PVEH is 0.547 mW/cm^3 for excitation at 100 Hz with 0.2*g* acceleration. At the same acceleration level, the proposed PVEH shows a slight increase in power density and a significant decrease in peak stress value. When both the PVEH are excited to the same level of stress (10 MPa), the power density of the proposed PVEH becomes 2.144 $mW/cm^{3,}$ and the power density of the conventional PVEH becomes 0.981 mW/cm^3.

5.8 ADVANTAGES OF THE PROPOSED THICKNESS-TAPERED PVEH-1

- The generated power is 19% more than conventional PVEH for the same input acceleration (0.2*g*).
- The generated power is 152% more than the conventional PVEH for the same peak stress (10 MPa).
- Power density is higher than the conventional PVEH.
- Input acceleration levels can be higher compared to the conventional PVEH.
- More robust and reliable compared to conventional PVEH.

5.9 POSSIBLE FABRICATION TECHNIQUE FOR PVEH-1

The Proposed PVEH-1 comprises a thickness-varying substrate layer sandwiched between two piezoelectric layers of uniform thickness. The substrate layer material can be casted in the desired shape or machined using a CNC machine, and the uniform-thickness piezoelectric layer can be glued on either side of the substrate.

5.10 CONCLUSIONS

The stress variation on the conventional cantilever-based PVEH is minimized using a thickness-tapered geometry. The proposed geometry consists of a thickness-tapered substrate layer and two piezoelectric layers of uniform thickness. Analytical expressions for end-mass displacement, stress profile and generated electrical voltage are derived for the proposed PVEH-1. The FE analysis results of an identical PVEH are consistent with the results obtained from the analytical expressions. The proposed PVEH-1 can generate 19% more power than the equivalent conventional PVEH with uniform thickness under identical input conditions. Since the stress in the proposed PVEH-1 is uniformly distributed, the peak stress is 32% less compared to the conventional PVEH. Thus, it is mechanically more reliable and capable of operating at higher input vibrations. When both the energy harvesters are exposed to the same peak stress, the proposed PVEH produces 152% more electrical power than the conventional PVEH.

CHAPTER 6

ANALYSIS OF PVEH-2 (THICKNESS-TAPERED PIEZOELECTRIC LAYER)

In chapter-4, we have proposed two new thickness-tapered geometries that give uniform stress along the length of cantilever-based PVEH. The first geometry consists of a substrate layer with a tapered thickness and two piezoelectric layers of uniform thickness and is named PVEH-1, while the second geometry consists of a substrate layer with uniform thickness and two piezoelectric layers of tapered thickness and is named PVEH-2. The width, across the length, is uniform in both the PVEH. In the previous chapter, analytical expressions have been derived for PVEH-1, and the results have been compared with the results from FE analysis. The performances of PVEH-1 have also been compared with an equivalent conventional PVEH of uniform thickness.

In this chapter, the second proposed geometry, PVEH-2, is studied. The main contribution of this chapter is the derivation of analytical expressions for resonance frequency, end-mass displacement, stress profile on the beam surface, and generated power for PVEH-2. In addition, FE analysis is carried out and the results are compared with the results from the derived analytical expressions. The performance of the proposed PVEH-2 is also compared with an equivalent conventional PVEH of uniform thickness.

6.1 Derivation of analytical expressions for PVEH-2

The PVEH-2 consists of a uniform thickness substrate layer placed between two thickness-tapered piezoelectric layers. The end-mass is fixed to the free end, and the input excitation is applied to the base.

6.1.1 Geometry and assumptions

The side view of PVEH-2 geometry is shown in Figure 6.1. The cantilever's width (along y-axis) is kept uniform.

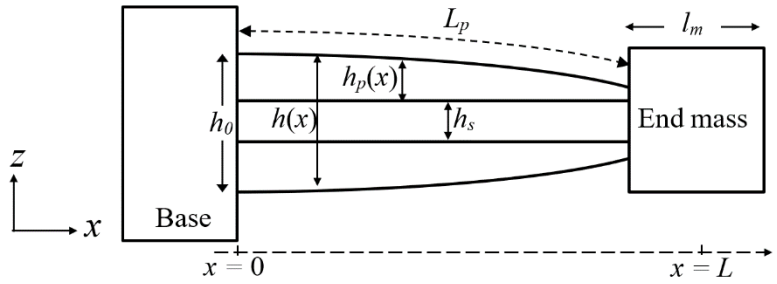

Figure 6.1: Side view of PVEH-2.

The overall thickness of the cantilever beam $h(x)$ is the summation of the thickness h_s of the substrate layer and thickness $h_p(x)$ each of the two piezoelectric layers, and the length of the piezoelectric layer is L_p. The top and bottom sides of the piezoelectric layers are metalized to form electrodes that are used to connect an external resistive load. The end-mass length is l_m and is attached to the free end of the beam. The effective length L is the distance from the base to the center of the end-mass. The cross-section across the length of the beam is shown in Figure 6.2 and it consists of two piezoelectric layers of tapered thickness $h_p(x)$ and a substrate layer of uniform thickness h_s. The width b is constant along the length of the beam. The parameter $h_{ps}(x)$ is the distance between the center of the piezoelectric layer and the beam's neutral axis (*NA*). The end-mass length is l_m and is attached symmetrically to the free end, as shown in Figure 6.1.

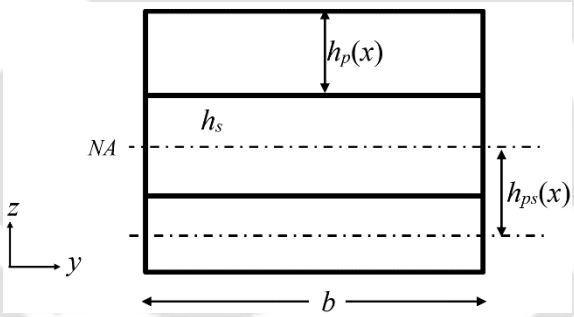

Figure 6.2: Cross-section view of the PVEH-2 beam.

As described in (4.13), $h(x)$ is the thickness of the beam and is a function of x along the length. Thus, the varying piezoelectric layer thickness $h_p(x)$ can be written as

$$h_p(x) = \left(\sqrt{\frac{L-x}{L}}\right)\frac{h_0}{2} - \frac{h_s}{2} \tag{6.1}$$

The input excitation is applied in the z-direction to the base at $x = 0$. When the input excitation frequency is near the cantilever's resonance frequency, the end-mass starts oscillating in the z-direction and exerts stress on the cantilever beam in the x-direction. The stress on the piezoelectric material generates an electrical voltage across the connected load resistance.

6.1.2 Derivation of spring constant and resonance frequency

The spring constant and the resonance frequency of the PVEH-2 are derived using the Euler-Bernoulli beam equation given by [74], [151]

$$\frac{d^2z(x)}{dx^2} = \frac{M(x)}{YI(x)} \tag{6.2}$$

Equation (6.2) is the second-order differential equation of the thickness-tapered cantilever, where $z(x)$ is the displacement of the beam along its length due to the moment $M(x)$ and beam stiffness $YI(x)$. Solving the second-order differential equation of the thickness-tapered beam (6.2) yields the beam deflection equation.

The moment $M(x)$ of the beam due to the end-mass motion can be written as [151]

$$M(x) = F(L - x) \tag{6.3}$$

where F is the force at $x = L$ due to the motion of the end-mass, the stiffness of the thickness-tapered composite beam can be written as [84]

$$YI(x) = \frac{Y_p b h^3(x)}{12} + (Y_s - Y_p)\frac{b h_s^3}{12} \tag{6.4}$$

where Y_p and Y_s are Young's moduli of the piezoelectric material and substrate material, respectively, and b is the uniform width of the beam. The beam equation (6.2) can be rewritten as

$$\frac{d^2z}{dx^2} = \frac{12(L - x)F}{Y_p b h^3(x) + (Y_s - Y_p) b h_s^3} \tag{6.5}$$

Solving (6.5) will produce the beam displacement $z(x)$ along the length due to the force F at $x = L$. The end-mass displacement is the beam displacement at $x = L$. As the cantilever is a mechanical spring, the beam's spring constant (k) can be expressed as the ratio of applied force F and the resultant displacement z at $x = L$. The beam equation (6.5) is solved in MATLAB for a unit force, and the spring constant k is calculated. From the spring constant obtained above, the resonance frequency ω_n of the energy harvester is expressed as

$$\omega_n = \sqrt{\frac{k}{m_e}} = \sqrt{\frac{k}{(33/140)m + M_t}} \tag{6.6}$$

where m_e is the effective mass of the cantilever represented by $(33/140)m + M_t$, where m is the mass of the beam and M_t is the mass of the end-mass [97].

6.1.3 Stress on the piezoelectric material

The end-mass motion exerts stress on the cantilever beam, and the stress is maximum on the top surface and gradually decreases towards the beam's neutral axis. Therefore the stress on the piezoelectric layer along the length *x* due to the moment *M*(*x*) can be written as [21]

$$T(x) = \frac{M(x)}{I(x)} h_{ps}(x) \tag{6.7}$$

and the average stress on the piezoelectric material can be written as

$$T = \frac{1}{L_p} \int_0^{L_p} \frac{M(x)}{I(x)} h_{ps}(x)\, dx \tag{6.8}$$

where *I*(*x*) is the cross-section moment of inertia of the composite beam and $h_{ps}(x)$ is the distance between the center of the piezoelectric layer and the neutral axis (*NA*) as shown in Figure 6.2 and are respectively given as follows.

$$I(x) = \frac{bh^3(x)}{12} + (\eta - 1)\frac{bh_s^3}{12} \tag{6.9}$$

$$h_{ps}(x) = \frac{h_s}{2} + \frac{h_p(x)}{2} \tag{6.10}$$

where η is the ratio of Young's moduli of the substrate and the piezoelectric material. For a sinusoidal input excitation of frequency ω, the end-mass motion will also be periodic, and hence the force and end-mass displacement will be a function of time given as

$$F(t) = kz(t) \tag{6.11}$$

where *z*(*t*) is the displacement of the end-mass. Thus, the average stress as a function of time can be written as

$$T(t) = \frac{1}{L_p} \int_0^{L_p} \frac{kz(t)}{\frac{bh_0^3}{12}\left[\frac{(L-x)}{L}\right]^3 + (\eta - 1)\frac{bh_s^3}{12(L-x)}} \left[\frac{h_s}{4} + \left(\sqrt{\frac{L-x}{L}}\right)\frac{h}{4}\right] dx \tag{6.12}$$

Equation (6.12) defines the instantaneous average stress on the piezoelectric material due to the end-mass displacement *z*(*t*), and it can be rewritten as

$$T(t) = z(t)\psi \tag{6.13}$$

where ψ is given by

$$\psi = \frac{1}{L_p}\int_0^{L_p} \frac{k}{\frac{bh_0^3}{12}\left[\frac{(L-x)}{L}\right]^3 + (\eta-1)\frac{bh_s^3}{12(L-x)}}\left[\frac{h_s}{4} + \left(\sqrt{\frac{L-x}{L}}\right)\frac{h}{4}\right]dx \tag{6.14}$$

Note that ψ depends on the composite cantilever's dimension and material properties and not on the input excitation condition.

6.1.4 Derivation of coupled equations

The equations for the end-mass displacement and the generated voltage across load resistance are derived in section 5.1.4 of the previous chapter. Using the same procedure, the coupled equations for the PVEH-2 can be written as

$$v(t) + RC_p\frac{dv(t)}{dt} - R\theta\frac{dz(t)}{dt} = 0 \tag{6.15}$$

$$\ddot{z}(t) + 2\zeta_m\omega_n\dot{z}(t) + \omega_n^2 z(t) + \frac{\theta}{m_e}v(t) = \ddot{y}(t) \tag{6.16}$$

where, C_p represents the capacitance of a single piezoelectric layer, and θ represents the electromechanical coupling coefficient of the energy harvester and are respectively given by

$$C_p = \frac{\varepsilon_{33}^T bL_p}{h_{p(av)}} \tag{6.17}$$

$$\theta = d_{31}bL_p\psi \tag{6.18}$$

6.1.5 Parallel connection of piezoelectric layers

Using the same procedure as discussed in section 5.1.5 for PVEH-1, the coupled equations for parallel-connected piezoelectric layers of the PVEH-2 can be written as

$$v(t) + 2RC_p\frac{dv(t)}{dt} - 2\theta R\frac{dz(t)}{dt} = 0 \tag{6.19}$$

$$\ddot{z}(t) + 2\zeta_m\omega_n\dot{z}(t) + \omega_n^2 z(t) + \frac{2\theta}{m_e}v = \ddot{y}(t) \tag{6.20}$$

Equations (6.19) and (6.20) are the coupled equations for the thickness-tapered PVEH-2 with parallel-connected piezoelectric layers. Solving (6.19) and (6.20) for displacement $z(t)$ and generated voltage $v(t)$, the generated electrical power can be calculated. When the energy harvester is excited with a sinusoidal excitation of angular frequency ω and peak amplitude Y_0 at the base, the solution for the above equations can be written as

$$z(t) = -\frac{m_e\omega^2 Y_0\left(1 + j2RC_p\omega\right)}{\left(\omega_n^2 - \omega^2 + j2\zeta_m\omega\omega_n\right)\left(m_e + j2m_eRC_p\omega\right) + j4R\theta^2\omega}e^{j\omega t} \tag{6.21}$$

$$v(t) = -\frac{2jR\theta m_e\omega^3 Y_0}{\left(\omega_n^2 - \omega^2 + j2\zeta_m\omega\omega_n\right)\left(m + j2m_eRC_p\omega\right) + j4R\theta^2\omega}e^{j\omega t} \tag{6.22}$$

The above analytical expressions are useful in estimating electrical power transferred to the resistive load due to the mechanical motion of the energy harvester.

6.1.6 Series connection of piezoelectric layers

Using the same procedure as discussed in section 5.1.6 for PVEH-1, the coupled equations for the series-connected piezoelectric layers of PVEH-2 can be written as

$$2v(t) + RC_p\frac{dv(t)}{dt} - 2R\theta\frac{dz(t)}{dt} = 0 \tag{6.23}$$

$$\ddot{z}(t) + 2\zeta_m\omega_n\dot{z}(t) + \omega_n^2 z(t) + \frac{\theta}{m_e}v(t) = \ddot{y}(t) \tag{6.24}$$

Equations (3.21) and (5.30) are the coupled equations for the thickness-tapered PVEH-2 with series-connected piezoelectric layers. Solving (3.21) and (5.30) for displacement $z(t)$ and generated voltage $v(t)$, the generated electrical power can be calculated. When the energy harvester is excited with a sinusoidal excitation of angular frequency ω and peak amplitude Y_0 at the base, the solution for the above equations can be written as

$$z(t) = -\frac{m_e\omega^2 Y_0\left(2 + jRC_p\omega\right)}{\left(\omega_n^2 - \omega^2 + j2\zeta_m\omega\omega_n\right)\left(2m + jm_eRC_p\omega\right) + j2R\theta^2\omega}e^{j\omega t} \tag{6.25}$$

$$v(t) = -\frac{j2m\omega^3 R\theta Y_0}{\left(\omega_n^2 - \omega^2 + j2\zeta_m\omega\omega_n\right)\left(2m_e + jm_eRC_p\omega\right) + j2R\theta^2\omega}e^{j\omega t} \tag{6.26}$$

6.2 GEOMETRICAL AND MATERIAL PROPERTIES OF PVEH-2

The detailed dimensions of the PVEH-2 used in the simulation are shown in Table 6.1. The energy harvester under consideration is a bimorph with parallel-connected piezoelectric layers. All calculations are performed for a constant input acceleration of $0.2g$ or 1.96 m/s^2. The piezoelectric material considered in all the simulations is PZT-5H, and for this material $d_{31} = -274 \text{ x } 10^{-12}$ C/N and $\varepsilon_{33}^T = 30.104 \text{ x } 10^{-9}$ F/m [155].

Table 6.1: Geometric and material parameters of the simulated PVEH-2.

Parameter	Description	Value
L	Beam length	50.0 mm
b	Beam width, end-mass width	5.0 mm
h_{p0}	Piezoelectric layer thickness at the base	1.5 mm
h_s	Substrate layer thickness	1.0 mm
l_m	Length and height of end-mass	21.7 mm
Y_s	Young's modulus of substrate material	110.0 (GPa)
Y_p	Young's modulus of the piezoelectric material	60.6 GPa
ρ_p	piezoelectric material (PZT-5H) density	7500 kg/m^3
ρ_p	Density of substrate material (Brass)	9000 (kg/m^3)
ρ_m	Density of end-mass material	11000 (kg/m^3)

The derived analytical expressions are solved in MATLAB using the specifications mentioned in Table 6.1. An FE model is also developed and studied to compare the analytical results. The 3D view of the proposed PVEH-2 developed for FE analysis in COMSOL Multiphysics is shown in Figure 6.3.

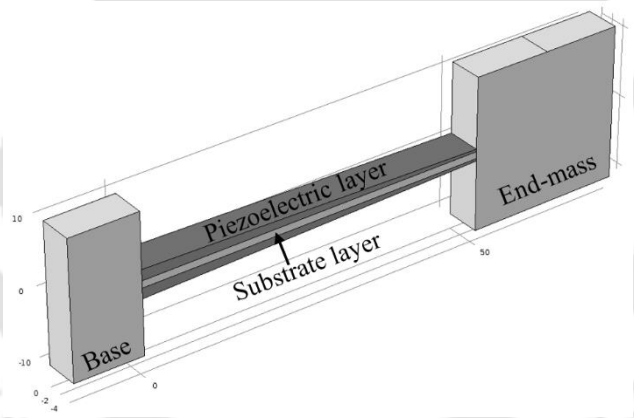

Figure 6.3: Geometry of PVEH-2 simulated in COMSOL Multiphysics.

6.3 RESULTS FROM THE DERIVED ANALYTICAL EXPRESSIONS

The analytical expressions derived for the parallel-connected piezoelectric layers are solved using MATLAB, and results are obtained for the resonance frequency of vibration, end-mass displacement, generated power, and stress profile on the surface. In the following sections, all the results are discussed in detail.

6.3.1 Calculation of resonance frequency

The resonance frequency for the PVEH-2 of the specifications mentioned above is calculated using (6.6). Piezoelectric materials exhibit lower stiffness in short-circuit conditions and higher

stiffness in open-circuit conditions [156]. Thus, the resonance frequency in the open-circuit condition is higher than the short-circuit condition. In this study, the resonance frequency mentioned is for the short-circuit condition. The resonance frequency found from the derived expression is 100.02 Hz and from FE analysis is 100.50 Hz.

6.3.2 Variation of end-mass displacement with load resistance

The end-mass displacement due to input base excitation is maximum near the resonance frequency. The end-mass displacement decreases as the excitation frequency moves away from the system resonance frequency. Figure 6.4 shows the variation of end-mass displacement with input frequency for different load resistances. As the load resistance increases from a very low value to higher values, the end-mass displacement varies and two peaks are observed as shown in Figure 6.4. The first peak at 100.02 Hz corresponds to the short-circuit resonance frequency and the other peak at 106.6 Hz corresponds to the open-circuit resonance frequency.

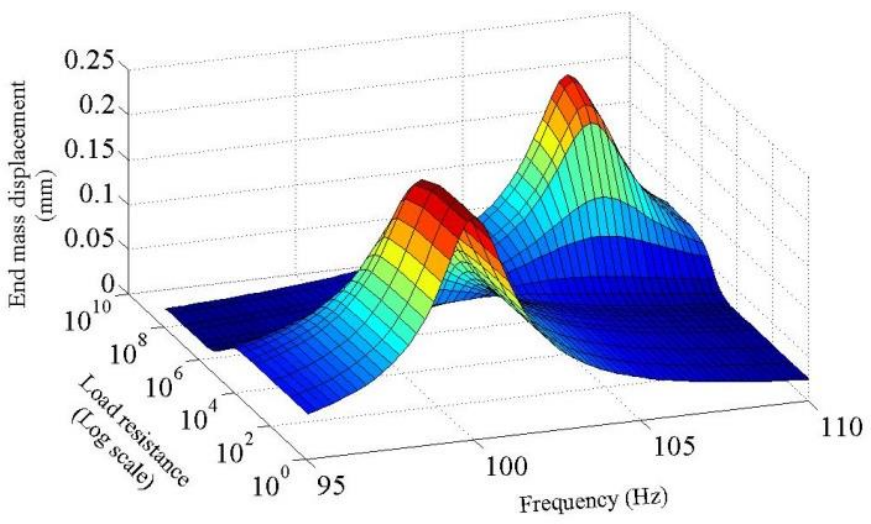

Figure 6.4: Plot of end-mass displacement versus frequency for various load resistance values.

6.3.3 Variation of electrical power with load resistance

The PVEH-2 generates an electrical voltage across the connected load resistance due to stress on it, and the power is calculated as the product of current through the load resistance and voltage across it. Figure 6.5 shows the variation of electrical power with frequency for various load resistances obtained from the derived analytical expressions. As the load resistance increases from a lower value to a very high value, the generated power varies and two peaks are observed as shown in Figure 6.5. The first peak at 100.02 Hz corresponds to the short-circuit resonance frequency and the other peak at 106.6 Hz corresponds to the open-circuit resonance frequency.

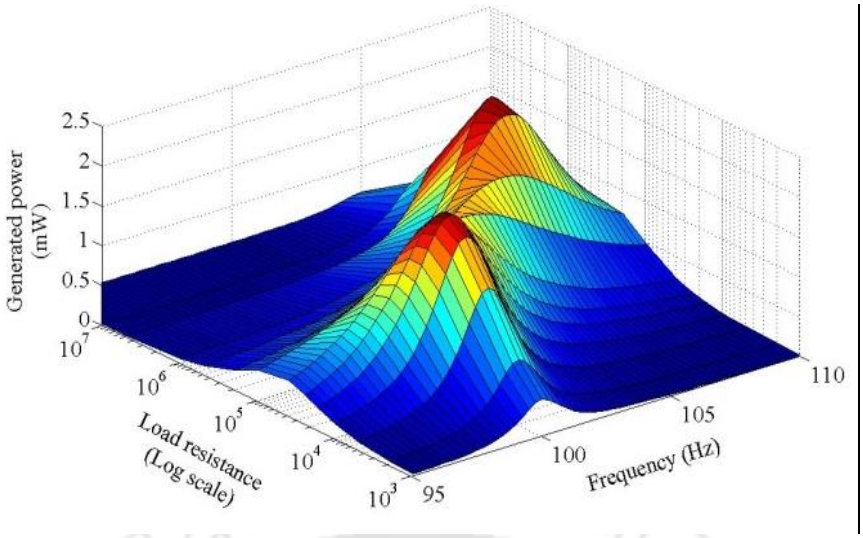

Figure 6.5: Plot of power versus frequency for various load resistance values.

As shown in Figure 6.5, the generated power depends on the connected load resistance, and the load resistance value for which the PVEH generates the highest power is called optimal load resistance. In the above analysis, the optimal load resistance is found to be 17 kΩ when the PVEH is excited with the short-circuit resonance frequency (100 Hz).

6.4 Comparison of analytical results with FE analysis

An FE model of conventional bimorph PVEH has been developed in chapter-2 using COMSOL Multiphysics. Using the same methodology, an FE model for PVEH-2 is developed, and a sinusoidal input of constant acceleration of 0.2*g* is applied at the base. The PVEH is simulated to obtain the end-mass displacement, generated power, and stress profile on the piezoelectric material.

6.4.1 Comparison of end-mass displacement

The end-mass displacement of the PVEH-2 is calculated using (6.21) for the short-circuit condition and plotted against input frequency in Figure 6.6 (a). The end-mass displacement for the same PVEH obtained from FE analysis is also plotted in Figure 6.6 (b). The analytical result shows that the peak value of end-mass displacement is 245 μm at 100 Hz frequency, and the result from the FE analysis shows that the peak value of end-mass displacement is 237 μm at 100.5 Hz frequency. FE analysis results are consistent with the analytical results. When the optimal load resistance (17 kΩ) is connected to the PVEH-2, the plots of end-mass displacement from the analytical result and FE analysis are shown in Figure 6.7 (a) and Figure 6.7 (b), respectively.

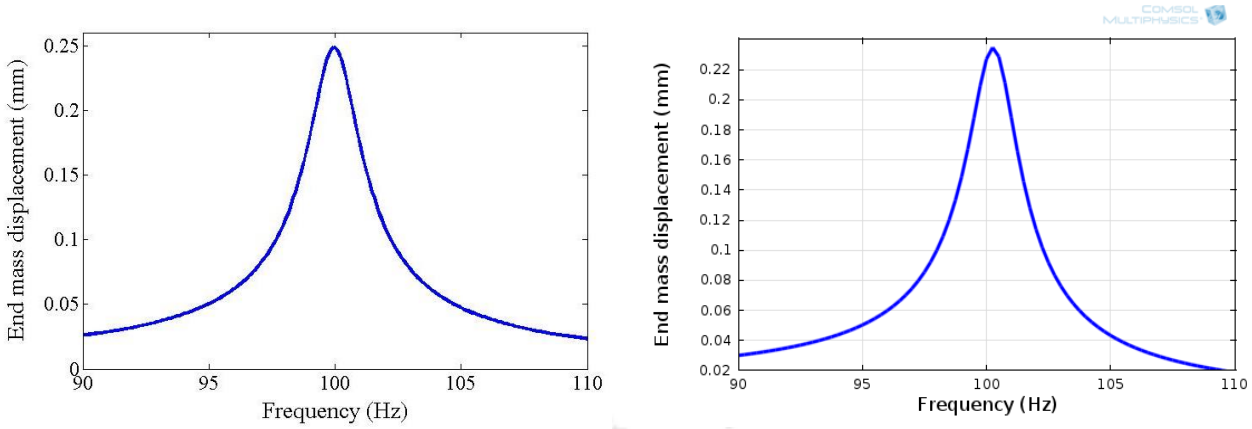

(a) (b)

Figure 6.6: Plot of end-mass displacements versus frequency at short-circuit condition from (a) the derived analytical expression and (b) FE analysis.

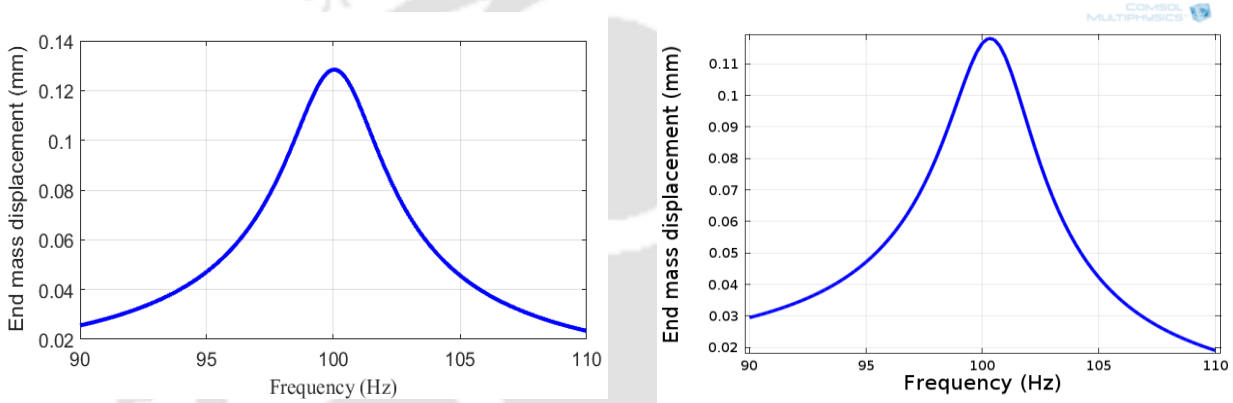

(a) (b)

Figure 6.7: Plot of end-mass displacements versus frequency at optimal load from (a) the derived analytical expression and (b) FE analysis.

6.4.2 Comparison of generated power at optimal load resistance

As shown in Figure 6.5, the electrical power depends on the connected load resistance, and to harvest maximum power, the load resistance should be of optimal value. The load resistance value for which the PVEH-2 generates the highest power is called optimal load resistance. Figure 6.8 (a) and Figure 6.8 (b) show the plots of the generated power at optimal load resistance obtained using the derived analytical expression and FE simulation.

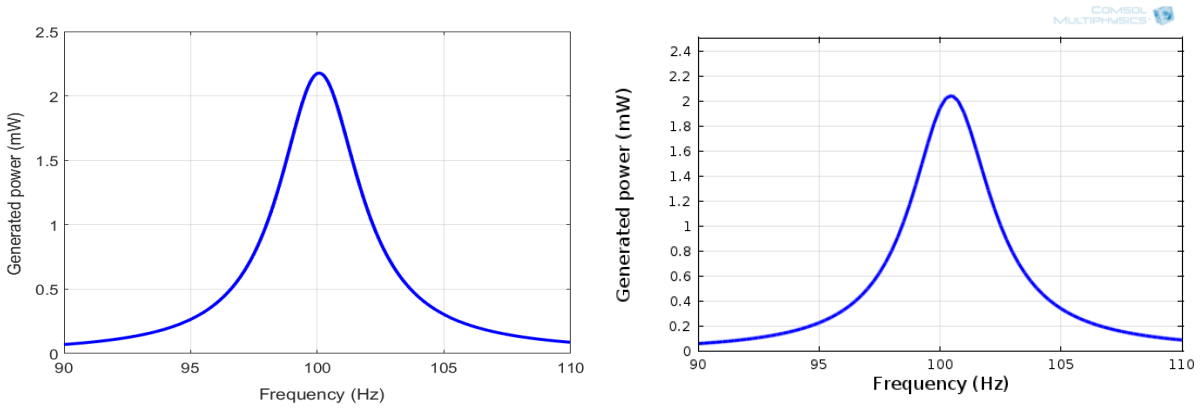

(a) (b)

Figure 6.8: Plot of power versus frequency at optimal load obtained from (a) analytical expression and (b) FE analysis.

6.4.3 Comparison of the stress profile

The end-mass of the cantilever oscillates due to the applied base excitation, and this oscillation produces stress on the piezoelectric material. The stress on the beam surface of the proposed PVEH-2 is uniform in nature which significantly increases the device reliability. The stress profile from the analytical solution and FE analysis results of the proposed PVEH-2 are shown in Figure 6.9 (a) and Figure 6.9 (b), respectively. The stress profiles are for the input excitation at 100 Hz frequency with 0.2*g* acceleration. The stress on the piezoelectric material is uniformly distributed along the entire length. This kind of distribution reduces the peak stress on the piezoelectric material and at the same time, raises the average stress on the piezoelectric material.

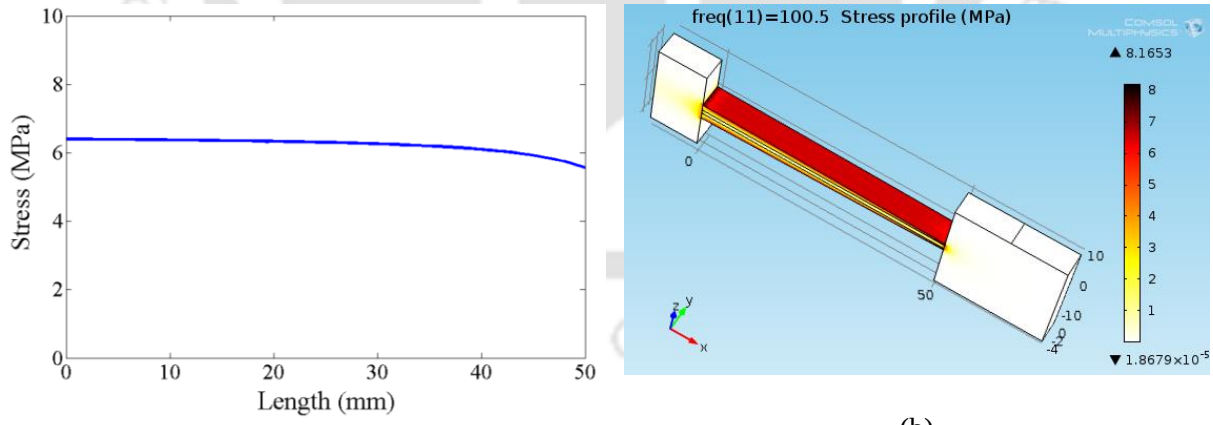

(a) (b)

Figure 6.9: Stress distribution along the length obtained from (a) analytical result and (b) FE analysis.

Table 6.2 summarizes the results from the derived analytical solution and FE analysis of the proposed PVEH-2. From the table, it is clear that the results from the derived analytical model are close to the results from FE analysis. In the next section, the proposed thickness-tapered PVEH-2 is compared with an equivalent conventional PVEH having a uniform thickness.

Table 6.2: Comparison of results using analytical model and FE analysis.

Parameters	**MATLAB result by solving derived analytical expressions**	**Results from FE analysis**
Natural frequency of vibration	100.02 Hz	100.50 Hz
Open circuit natural frequency of vibration	106.6 Hz	106.5 Hz
End-mass displacement in short circuit	245 μm	237 μm
End-mass displacement at optimal load	128 μm	118 μm
Generated power at optimal load of 17 kΩ	2.18 mW	2.08 mW
Peak stress	6.40 MPa	6.43 MPa

The comparison table shown above confirms that the results from the derived analytical model are equivalent to the results from FE analysis. In the next section, we will be comparing the proposed device's performance with its equivalent conventional PVEH with uniform thickness.

6.5 COMPARISON WITH CONVENTIONAL PVEH

The conventional PVEH refers to the cantilever-based PVEH with a uniform cross-section throughout the length. In the equivalent conventional PVEH, the thickness of the piezoelectric layer is set as the average piezoelectric thickness of the proposed energy harvester that is 1.0 mm. The substrate layer thickness and the width of the conventional energy harvester beam are equal to that of the proposed energy harvester. Analytical expressions have been derived for conventional PVEH with uniform thickness in chapter-3 and are used herein to evaluate the performance of the equivalent conventional PVEH. The resonance frequency of the equivalent conventional energy harvester is kept the same (100 Hz) as that of the proposed PVEH-2 by adjusting the end-mass. All the geometrical parameters of the equivalent conventional PVEH are shown in Table 6.3 and the material properties are the same as that of the PVEH-2.

Table 6.3: Geometrical parameters of the equivalent conventional PVEH.

Parameter	**Description**	**Value**
L	Beam length	50 mm
b	Beam width	5 mm
h_p	Piezo layer thickness	1 mm
h_s	Substrate layer thickness	1 mm
l_m	End-mass length and height	20.65 mm

The end-mass for the equivalent conventional energy harvester is 23.45 grams, whereas that of the PVEH-2 is 25.90 grams. Both the energy harvesters are excited with a constant acceleration

of 0.2*g* (1.96 m/s^2) around their resonance frequency, and their responses are recorded. Figure 6.10 shows the schematic diagram of the equivalent conventional PVEH with uniform cross-section beam.

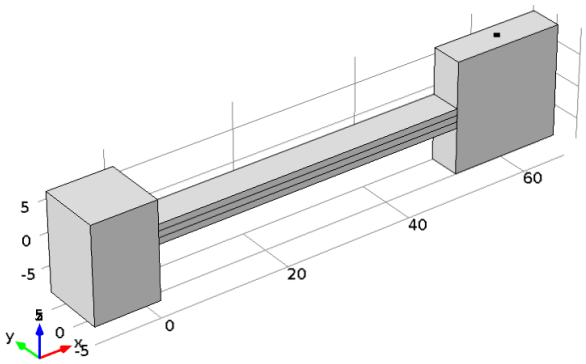

Figure 6.10: Geometry of the equivalent conventional PVEH.

6.5.1 Comparison of end-mass displacement

The proposed PVEH-2 and the equivalent conventional PVEH are excited with the same input acceleration, i.e., 0.2*g* at their respective bases, and their performances are compared. The displacements of the end-mass for both the devices are measured when optimal load resistances are connected. Figure 6.11 compares the end-mass displacements of the proposed PVEH-2 and its equivalent conventional PVEH, which are 128 μm and 124 μm, respectively. Both the energy harvesters resonate at the same frequency and show almost equal end-mass displacement.

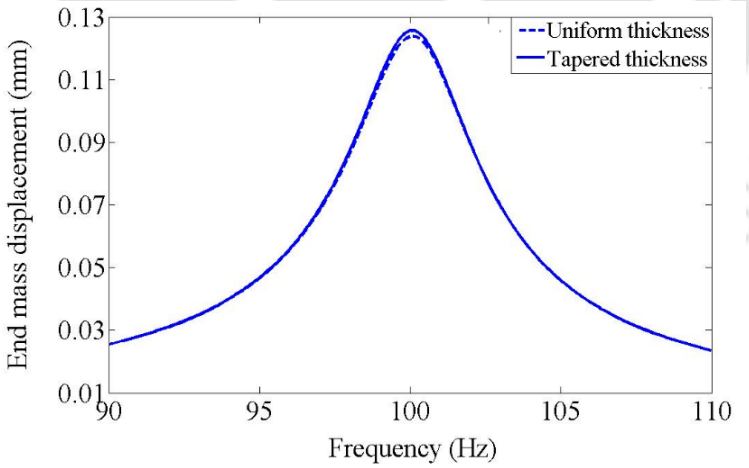

Figure 6.11: Comparison of end-mass displacements of PVEH-2 (tapered thickness) and conventional PVEH (uniform thickness).

6.5.2 Comparison of the stress profile

Figure 6.12 shows the plot of stress distribution on the beam surface for the proposed PVEH-2 and the equivalent conventional PVEH at an excitation frequency of 100 Hz with 0.2*g* (1.96 m/s^2) acceleration. The conventional PVEH experiences the highest stress at the fixed end, whereas the proposed PVEH-2 experiences almost uniform stress all along the length.

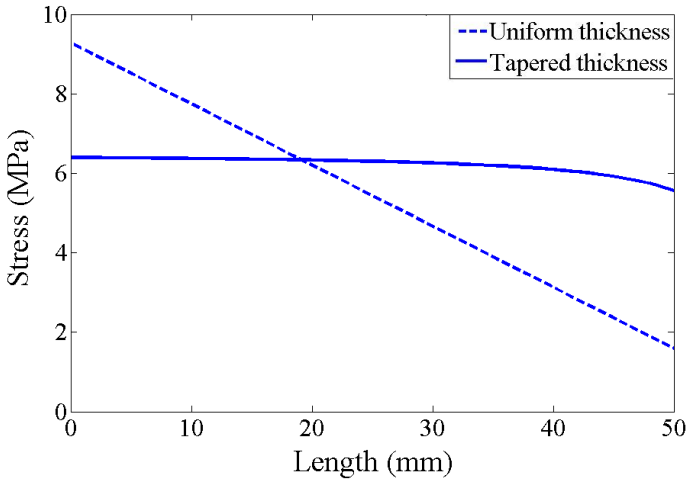

Figure 6.12: Comparison of stress distribution along the length of PVEH-2 (tapered thickness) and conventional PVEH (uniform thickness).

The proposed thickness-tapered PVEH-2 is more reliable as the stress is well distributed along the entire length, and it can be used for higher input accelerations compared to equivalent conventional PVEH. The peak value of stress on the proposed PVEH-2 is 6.40 MPa at the fixed end of the beam, and the minimum value of stress is 5.43 MPa at the free end of the beam. On the other hand, the highest value of stress on the conventional PVEH is 9.28 MPa, and the minimum value of stress is 1.59 MPa. The average stress on the beam is calculated from stress at fifty different points on the beam and it is found to be 6.195 MPa for the proposed PVEH-2 and 5.43 MPa for the conventional PVEH. Though the peak stress on the proposed PVEH is significantly lower, the average stress is noticeably higher than the conventional energy harvester.

FE analyses of the proposed PVEH-2 and its equivalent conventional energy harvester are carried out, and their 3D views of stress distribution are shown in Figure 6.13 (a) and (b), respectively.

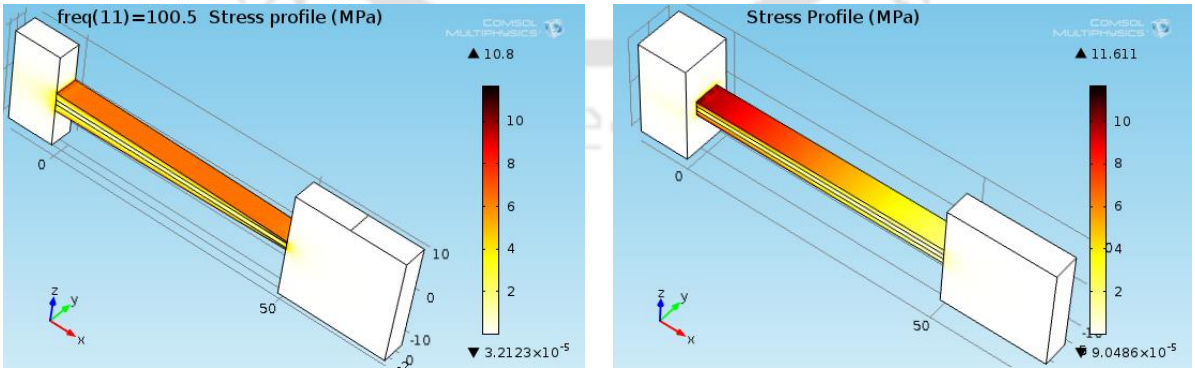

(a) (b)

Figure 6.13: 3-D views of stress distribution on (a) proposed PVEH-2 and (b) conventional PVEH.

6.5.3 Comparison of generated power

The generated power from a PVEH is directly proportional to the average stress on the piezoelectric material. In the previous subsection, we have seen that the proposed energy harvester experiences significantly higher average stress on the piezoelectric material, and thus it should generate higher electrical power compared to the conventional PVEH. Figure 6.14 shows the generated power for optimal load resistance from the proposed PVEH-2 and equivalent conventional PVEH for the same input acceleration ($0.2g$). The peak generated power is 2.18 mW and 1.90 mW from the proposed PVEH-2 and conventional PVEH, respectively. In uniform thickness PVEH, the stress reduces linearly along the length as observed in Figure 6.12, and the piezoelectric material towards the free end remains underutilized, whereas in the proposed PVEH-2, the piezoelectric material experiences almost uniform stress and contributes equally to the energy generation process, resulting in more harvested power.

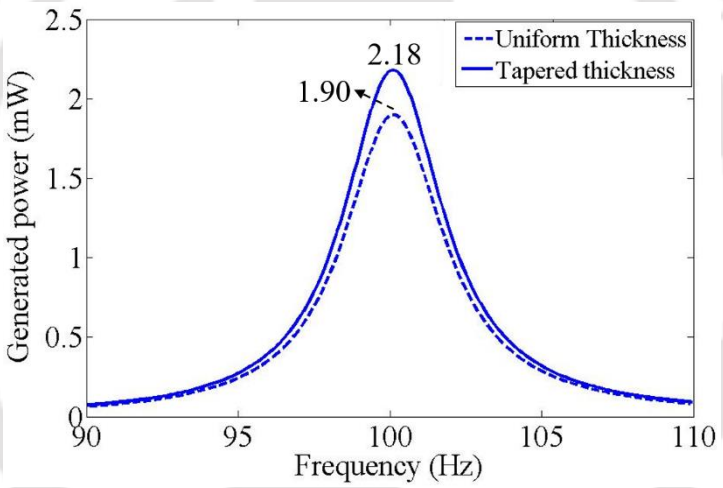

Figure 6.14: Comparison of harvested power from proposed PVEH-2 (tapered thickness) and conventional PVEH (uniform thickness).

6.5.4 Comparison of generated power at equal stress

The proposed PVEH-2 experiences less stress and generates higher power compared to the conventional PVEH for the same input conditions. The lower stress on the proposed PVEH-2 allows the use of this energy harvester for higher input accelerations without much stress on the piezoelectric materials. In this section, both the energy harvesters are exposed to the same peak stress value, and their performances are compared. Here both conventional and proposed PVEH are excited with 100 Hz frequency such that the peak stress on the piezoelectric material is 10 MPa. To achieve the peak stress, the proposed PVEH-2 is excited with 3.065 m/s^2 acceleration, and the conventional energy harvester is excited with 2.112 m/s^2 acceleration. When both the PVEH are excited to the 10 MPa stress level, the stress distributions are as shown in Figure 6.15.

The generated powers at the same stress level are 5.328 mW and 2.205 mW, respectively, for the PVEH-2 and the conventional PVEH and are shown in Figure 6.16.

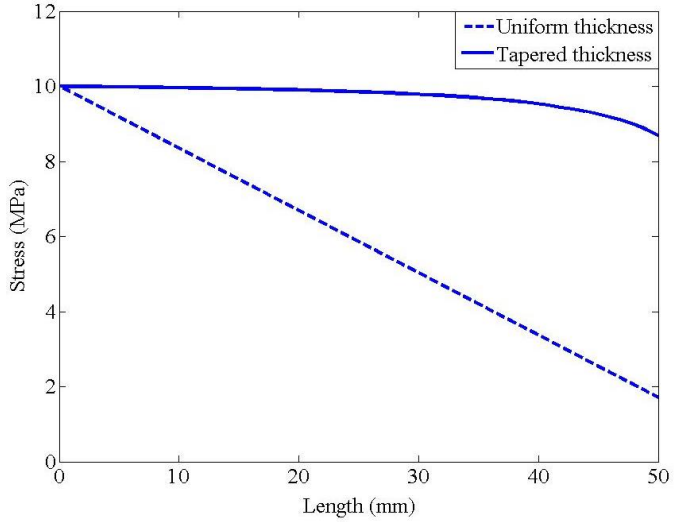

Figure 6.15: Stress profile comparison of the proposed PVEH-2 (tapered thickness) and conventional PVEH (uniform thickness) for equal peak stress of 10 MPa.

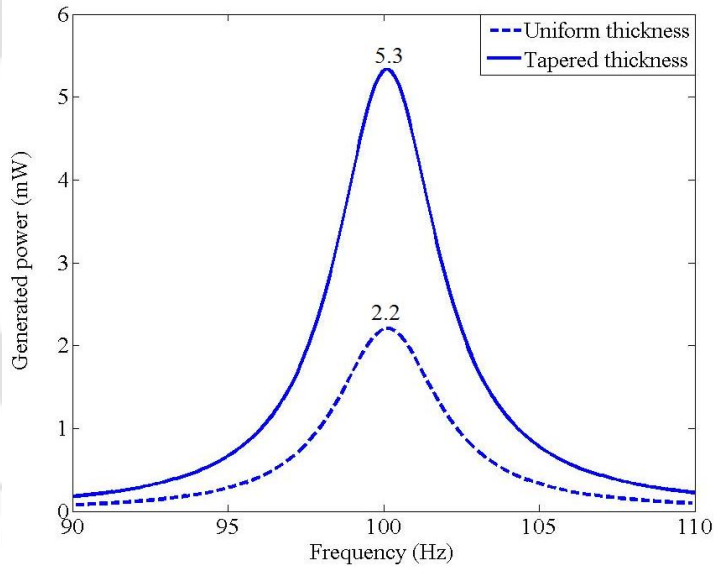

Figure 6.16: Generated power from the proposed PVEH-2 (tapered thickness) and conventional PVEH (uniform thickness) for equal peak stress of 10 MPa.

6.6 POWER DENSITY

The power density is calculated by dividing the harvested power by the corresponding device volume. The total volume is the summation of beam volume and end-mass volume. The proposed PVEH-2 beam and the equivalent conventional beam have equal volume. The beam volume for both the devices is 0.750 cm^3, the end-mass volume for the proposed PVEH-2 is 2.3544 cm^3 and that of the conventional PVEH is 2.132 cm^3. Thus, the total volume of the proposed PVEH-2 is 3.104 cm^3 and the total volume of the conventional PVEH is 2.882 cm^3. The power density for the proposed PVEH-2 is 0.702 mW/cm^3 and for the conventional PVEH is 0.659 mW/cm^3 for

excitation at 100 Hz with 0.2*g* acceleration. At the same acceleration level, the proposed PVEH shows a slight increase in power density and a significant decrease in peak stress value. When both the PVEH are excited to the same level of stress (10 MPa), the power density of the proposed PVEH is 1.716 mW/cm^{3,} and the power density of the conventional PVEH is 0.765 mW/cm^3.

The proposed PVEH-2 shows a significant improvement in the generated power compared to the equivalent conventional PVEH of uniform thickness. The summary of all the observations is given in Table 6.4 to compare both the energy harvesters quantitively.

Table 6.4: Output comparison of the proposed and conventional PVEH.

	Proposed PVEH-2	**Conventional PVEH**
Displacement of end-mass at 0.2*g* acceleration	128 μm	124 μm
Generated power at 0.2*g* acceleration	2.18 mW	1.90 mW
Maximum stress at 0.2*g* acceleration	6.40 MPa	9.28 MPa
Power density at 0.2*g* acceleration	0.702 mW/cm^3	0.659 mW/cm^3
Generated power at 10 MPa stress	5.328 mW	2.205 mW
Power density at 10 MPa stress	1.716 mW/cm^3	0.765 mW/cm^3

6.7 ADVANTAGES OF THE PROPOSED PVEH-2 OVER CONVENTIONAL PVEH

- The generated power is 14.7% more than the conventional PVEH for the same input acceleration (0.2*g*).
- The Peak stress value is 31% lower than the conventional PVEH for the same input acceleration (0.2*g*).
- The generated power is 141.6% more than the conventional PVEH for the same peak stress (10 MPa).
- Higher power density compared to the conventional PVEH.
- The proposed energy harvester can be used for higher acceleration levels compared to conventional PVEH.
- The proposed energy harvester is mechanically more robust and reliable than conventional PVEH.

6.8 POSSIBLE FABRICATION TECHNIQUE FOR PVEH-2

The proposed PVEH-2 comprises a substrate layer of uniform thickness sandwiched between two thickness-varying piezoelectric layers. Since piezoelectric material (PZT-5H) is brittle, the

nonuniform thickness layer is difficult to realize with the present fabrication technology. To attain the desired thickness profile of the piezoelectric layers, piezoelectric patches of different lengths can be stacked together as shown in the Figure 6.17 below.

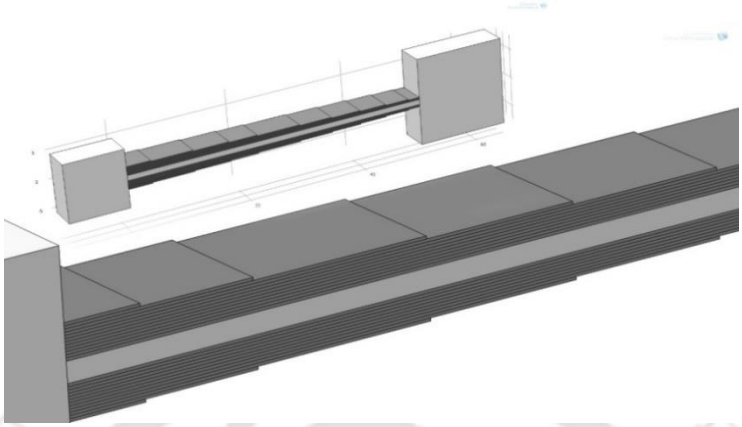

Figure 6.17: Thickness-tapered beam using several layers of piezoelectric material.

6.9 COMPARISON OF PROPOSED PVEH-1 AND PVEH-2

As discussed above, the proposed PVEH-1 and PVEH-2 perform better in all respect compared to equivalent conventional PVEH due to uniform stress profile. In this section comparison between PVEH-1 and PVEH-2 is done to know the suitability of each device.

Table 6.5: Comparison of proposed PVEH-1 and PVEH-2

Parameter	**PVEH-1**	**PVEH-2**
Device volume	2.575 cm^3	**3.104 cm^3**
Volume of piezoelectric material	0.125 cm^3	**0.500 cm^3**
Generated power at 0.2*g*	1.46 mW	**2.18 mW**
Peak stress value	5.14 MPa	**6.40 MPa**
Power density per unit volume of piezo material	**11.68 mW/cm^3**	4.36 mW/cm^3
Input acceleration for 10 MPa stress	**3.81 m/s^2 (0.3884 *g*)**	3.065 m/s^2 (0.313*g*)
Power density mW/cm^3 for 0.2*g* acceleration	0.567 mW/cm^3	**0.702 mW/cm^3**
Generated power at 10 MPa	**5.522 mW**	5.328 mW
Power per unit peak stress	**0.552 mW/MPa**	0.5328 mW/MPa
Power density mW/cm^3 at 10 MPa stress	**2.144 mW/cm^3**	1.716 mW/cm^3

Table 6.5 summaries mechanical and electrical output parameters for both the proposed energy harvesters. When the same input acceleration (0.2*g*) is applied to both the devices, PVEH-2 generates 49% more power, however, PVEH-2 has higher device volume resulting in 27% more power density. The peak stress value on PVEH-2 is 24.5% more compared to PVEH-1. For a

given acceleration, PVEH-1 will experience lower stress, therefore PVEH-1 will be a better choice to deploy when acceleration levels are high.

6.10 CONCLUSIONS

The stress variation on the conventional PVEH is minimized using a thickness-tapered geometry. The proposed geometry (PVEH-2) consists of a uniform thickness substrate layer and two thickness-tapered piezoelectric layers. Analytical expressions for the resonance frequency, end-mass displacement, stress profile and generated electrical voltage are derived for the proposed PVEH-2. The FE analysis results of an identical PVEH are consistent with the results obtained from the analytical expressions. The proposed PVEH-2 can generate 14.7% more power than the equivalent conventional PVEH with uniform thickness under identical input conditions. Since the stress in the proposed PVEH-2 is uniformly distributed, the peak stress is 31% less compared to the conventional PVEH. Thus, it is mechanically more reliable and capable of operating at higher input acceleration. When both the energy harvesters are exposed to the same peak stress, the proposed PVEH produces 141.6% more electrical power than the conventional PVEH.

CHAPTER 7

ANALYSIS OF DIAPHRAGM-BASED PVEH

A diaphragm-based PVEH structure consists of a circular piezoelectric disk generally attached to a metallic substrate layer, and a proof mass is fixed at the center [2]. The diaphragm is normally made of unimorph or bimorph piezoelectric layers. An introduction to the diaphragm-based PVEH has been presented in Chapter-1.

In this chapter, a circular diaphragm-based PVEH is modeled in COMSOL Multiphysics and FE analysis is carried out to find output power, stress profile and displacement of the proof mass. Initially, the entire diaphragm is simulated as a single energy harvester, and subsequently, the diaphragm is divided into different angular slices by introducing radial cuts. The optimal slicing angle is estimated from the FE analysis results. A broadband energy harvester is proposed using a combination of different angular slices.

7.1 FE ANALYSIS OF THE DIAPHRAGM-BASED PVEH

The FE analysis of diaphragm-based PVEH is carried out using the piezoelectric-circuit interface of the software. A sinusoidal input excitation is applied to the outer base of the diaphragm and a proof mass is attached at the center to adjust the resonance frequency. When the input vibration frequency matches the device resonance frequency, the diaphragm starts oscillating, and the mass at the center shows the maximum displacement. The stress due to displacement of the mass induces an electrical voltage between the electrodes placed on piezoelectric layers. The geometrical specification and the material properties of the analyzed diaphragm are given in Table 7.1. The plate of the diaphragm-based PVEH consists of a substrate layer sandwiched between two piezoelectric layers. The circular outer ring works as the base and can be attached to an external vibration source, and a circular proof mass is used at the center to control the resonance frequency, as shown in Figure 7.1. Figure 7.1The piezoelectric material used is PZT-5H and the material properties are already discussed in the previous chapters.

Table 7.1: Geometrical and material parameters of the diaphragm-based PVEH.

Parameter	Description	Value
R	Diaphragm radius	70.00 mm
h_p	Piezo-layer thickness	0.25 mm
h_s	Substrate layer thickness	1.50 mm
R_m	The radius of the proof mass	20.00 mm
h_m	The thickness of the proof mass	25.00 mm
Y_p	Young's modulus of piezoelectric material	60.60 GPa
Y_s	Young's modulus of substrate (Brass)	110 GPa
ρ_p	Density of the substrate (Brass)	9000 kg/m^3
ρ_m	Density of the proof mass	15000 kg/m^3
V	Device volume	59.66 cm^3

In the FE analysis of the above PVEH, the eigenmode frequency analysis and frequency domain analysis are carried out to study different output characteristics of the energy harvester.

7.1.1 Resonance frequency of vibration

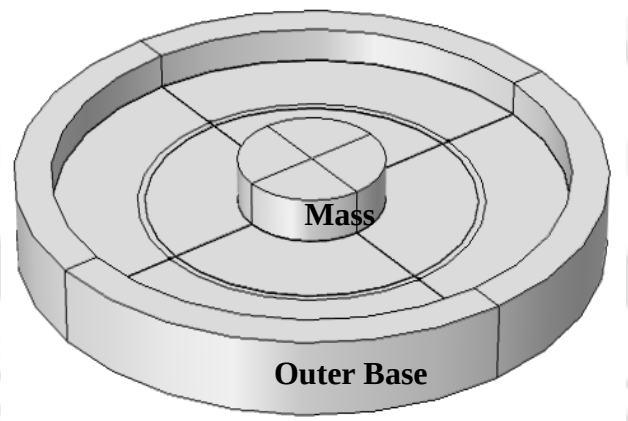

Figure 7.1: Geometry of circular diaphragm-based PVEH.

The resonance frequency of vibration is estimated from the eigenmode frequency analysis. In this analysis, short-circuit and open-circuit resonance frequencies are estimated. The load resistance value should be zero to estimate the short-circuit resonance frequency, and it should be very high to estimate the open-circuit resonance frequency.

The short-circuit and open-circuit resonance frequencies are found by eigenmode frequency analysis of the diaphragm and are 284 Hz and 301.5 Hz, respectively. The proof mass displacement for the open-circuit condition and short-circuit condition is shown in Figure 7.2.

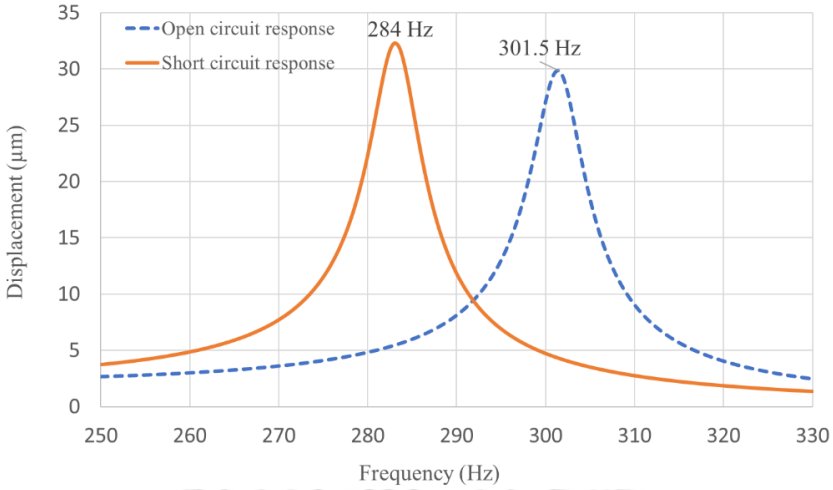

Figure 7.2: Plots of displacement versus frequency for short-circuit and open-circuit conditions.

7.1.2 Voltage and power from the PVEH

The diaphragm-based PVEH is excited with sinusoidal input excitations at the outer base. The input excitation is of the varying frequency with a constant acceleration of 0.2g. The mass at the center oscillates with the same frequency as that of the input excitation. The displacement of the mass exerts stress on the piezoelectric material, generating an electrical voltage across the connected load resistance. As the central mass moves upward, the strain on the outer edge of the plate is negative and on the inner edge is positive and vice versa. This opposite strain on the diaphragm surface generates two opposite polarity voltages on the electrodes, as shown in Figure 7.3. Therefore, the piezoelectric layer on the surface is divided into two sections, viz. inner region, close to proof mass, and outer region, close to the base.

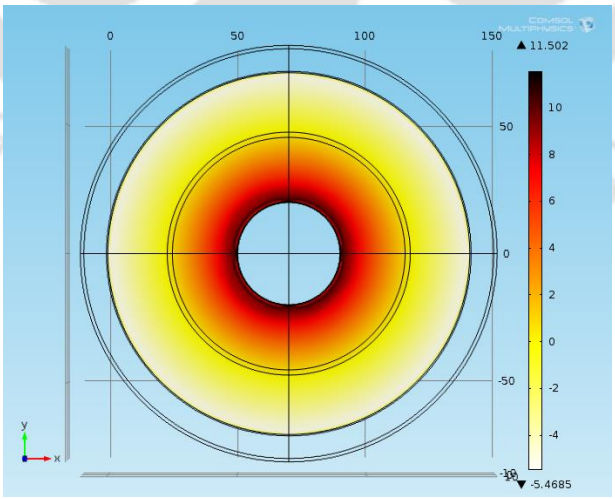

Figure 7.3: Distribution of voltage on the diaphragm surface.

In Figure 7.3, the generated voltages on the inner and outer regions are of opposite polarity. Therefore, separate electrodes are needed for each region. The electrodes are connected with two separate resistive loads, and the total generated power is the summation of powers from both the

load resistances. The variations of proof mass displacement and the corresponding total power are plotted against the input frequency and are shown in Figure 7.4 and Figure 7.5, respectively.

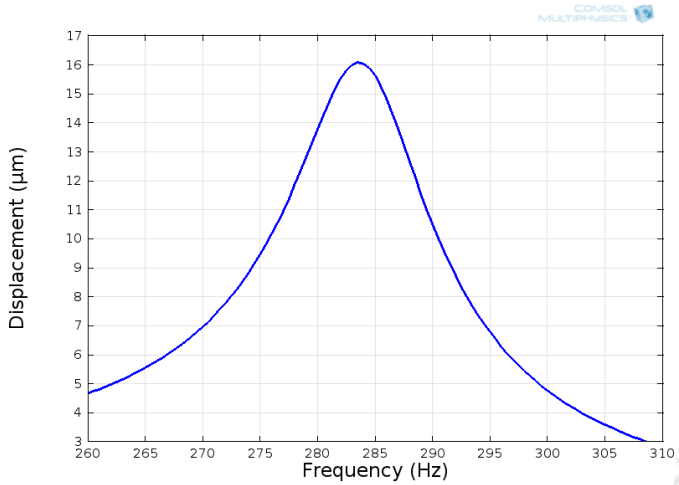

Figure 7.4: Plot of proof mass displacement versus frequency at optimal load.

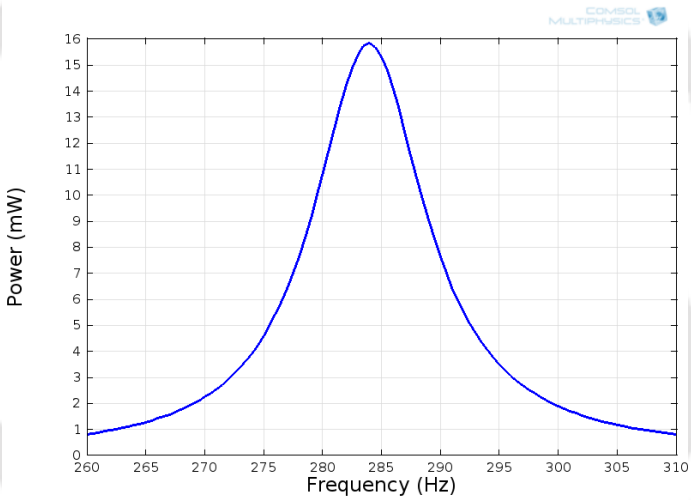

Figure 7.5: Plot of generated power versus frequency at optimal load.

The above results show that the peak value of the proof mass displacement is 16.08 µm at the frequency 284 Hz. The peak stress on the diaphragm is 3.7 MPa and the generated peak power is 15.84 mW at the resonance frequency. The electrical power density of the diaphragm-based energy harvester is 0.261 mW/cm^3 for an input acceleration of 0.2*g*.

7.1.3 Stress profile on the diaphragm surface

The stress profile on the piezoelectric surface is shown in Figure 7.6 for 284 Hz excitation with optimal load resistance connected. It is observed from the stress profile that the stress is mainly concentrated at the inner edge close to the proof mass. The stress distribution is similar to that of the conventional cantilever-based PVEH discussed in section 4.2. In this type of stress distribution, the average stress on the piezoelectric material significantly reduces, resulting in

lower electrical power generation. In addition, the inner edge near the proof mass experiencing the highest stress is prone to mechanical failure.

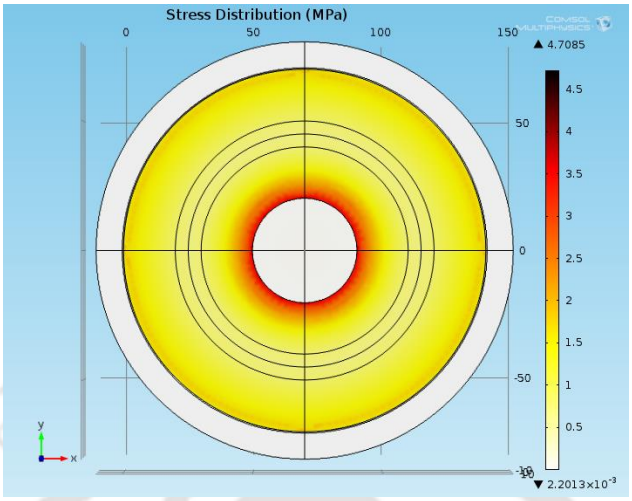

Figure 7.6: Distribution of stress on the diaphragm surface.

In the following sections, the conventional diaphragm-based PVEH is divided into several angular slices by giving radial cuts to study harvested power and bandwidth.

7.3 ANGULAR SLICING OF THE DIAPHRAGM

The diaphragm-based structures typically have higher resonance frequency than the cantilever-based structures. On the other hand, most of the vibration sources suitable for energy harvesting range from 100 Hz to 200 Hz. The options to reduce the resonance frequency of vibration are generally by increasing the mass at the center or by increasing the diameter. Both the options increase the device's mass and volume, thus reducing the power density. The other option to reduce resonance frequency is by reducing the diaphragm thickness, which increases the stress and makes the device more prone to mechanical failure.

In this study, we propose to divide the diaphragm into angular slices (*sectors*) so that the individual slices will behave as cantilevers and the resonance frequency will reduce, increasing the harvested power. The entire diaphragm is divided into an integral number (n) of identical slices and Figure 7.7 shows the conventional diaphragm and divided diaphragm for $n = 8$.

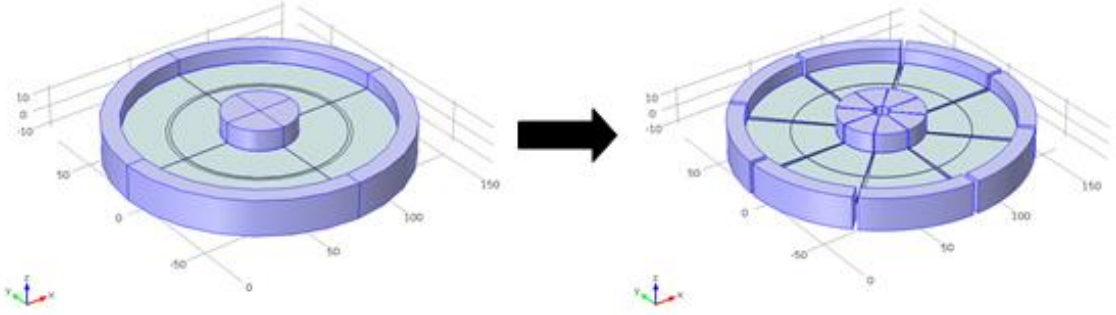

Figure 7.7: Schematic of conventional diaphragm (left) and diaphragm sliced in 8 sectors (right).

7.3.1 Angular slicing

Analysis is carried out for cases in which the diaphragm is divided into integral number (*n*) of identical slices (*sectors*) for all integers between 2 and 16, and selected values of *n* beyond 16. The division results in 2, 3, 4, 5, 6, 7, 8, 9, 10, 11, 12, 13, 14, 15, 16, 18, 20, 24, 30, 36, 40, 45, 60, 90, 120, 180 and 360 number of slices (*sectors*) corresponding to the *central angles* of 180^o, 120^o, 90^o, 72^o, 60^o, 51.4^o,45^o, 40^o, 36^o, 32.7^o, 30^o, 27.6^o, 25.7^o, 24^o, 22.5^o, 20^o, 18^o, 15^o, 12^o, 10^o, 9^o, 8^o, 6^o, 4^o, 3^o, 2^o and 1^o, respectively.

The 180^o slicing results in two equal slices of the diaphragm, similarly 120^o slicing results in the three equal slices and so on. The pictorial representation of 90^o (n = 4) and 36^o (n = 10) slicing of the diaphragm is shown in Figure 7.8.

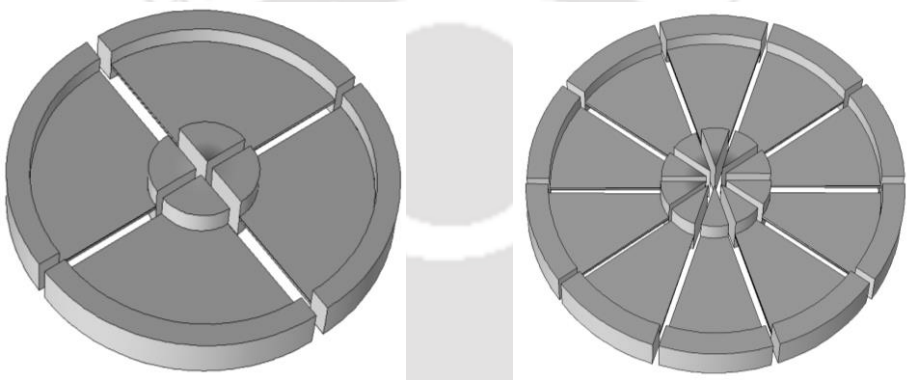

(a) (b)

Figure 7.8: 3-D view of the diaphragm divided in equal slices each of angle (a) 90^o and (b) 36^o.

7.3.2 FE analysis of the angular slices

The diaphragms sliced with the above-mentioned angles are studied using FE analysis, and the results are obtained for resonance frequency of vibration, displacement of the mass, distribution of stress, and generated power. For the entire study, a sinusoidal excitation is applied for a range of frequencies around the resonance frequency and the acceleration level is kept constant at 0.2g.

A total of 27 cases of sliced diaphragm mentioned above are simulated and their results are studied. The plots of generated power in the entire diaphragm and stress distribution for angles of 120^o, 90^o, 60^o, 45^o, 36^o, 20^o, and 10^o in one sector are shown in Figure 7.9 to Figure 7.15, respectively.

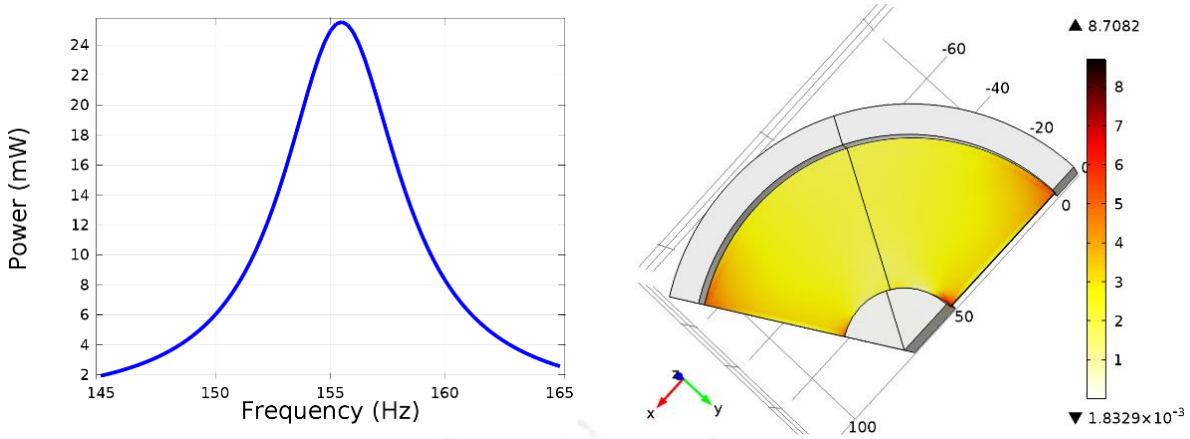

Figure 7.9: Plots of (a) total power generated in the diaphragm versus frequency and (b) stress distribution in 120^0 slice.

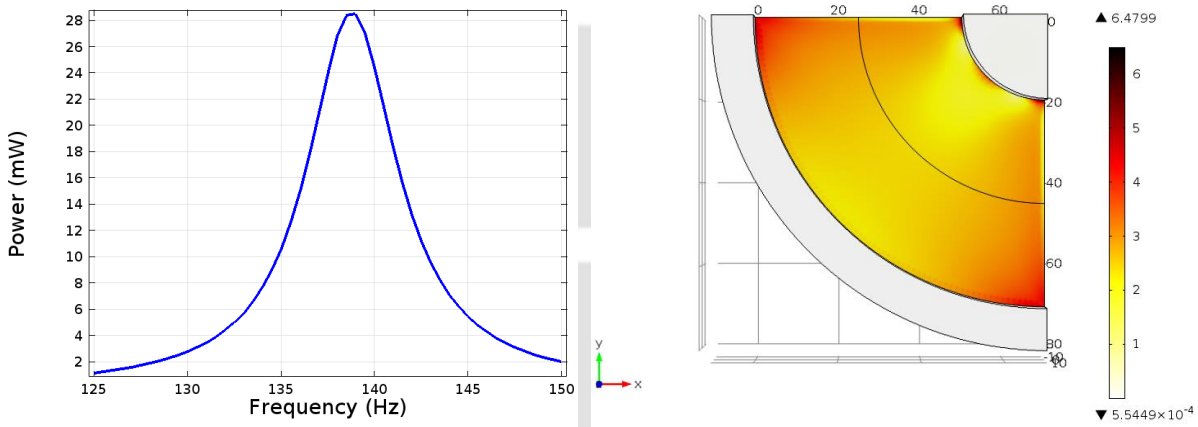

(a) (b)

Figure 7.10: Plots of (a) total power generated in the diaphragm versus frequency and (b) stress distribution in 90^0 slice.

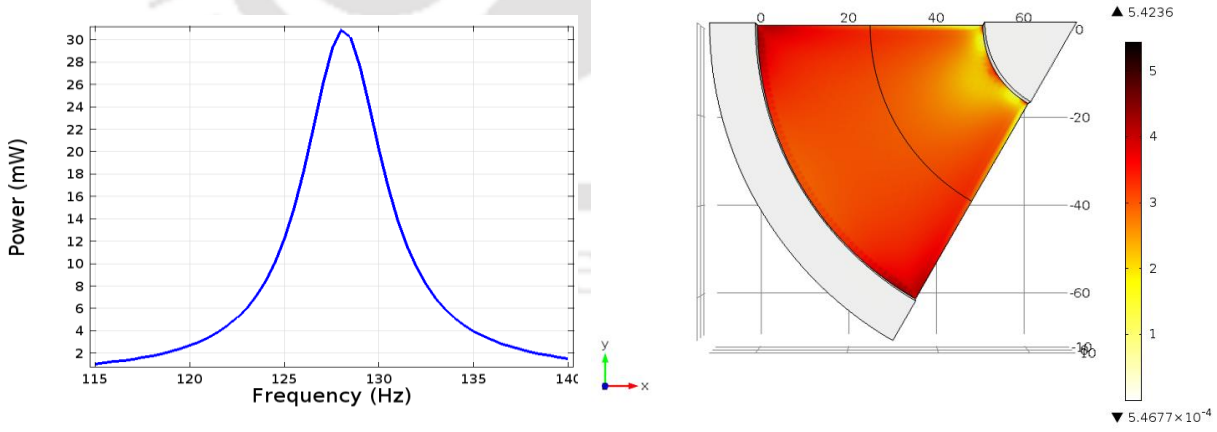

Figure 7.11: Plots of (a) total power generated in the diaphragm versus frequency and (b) stress distribution in 60^o slice.

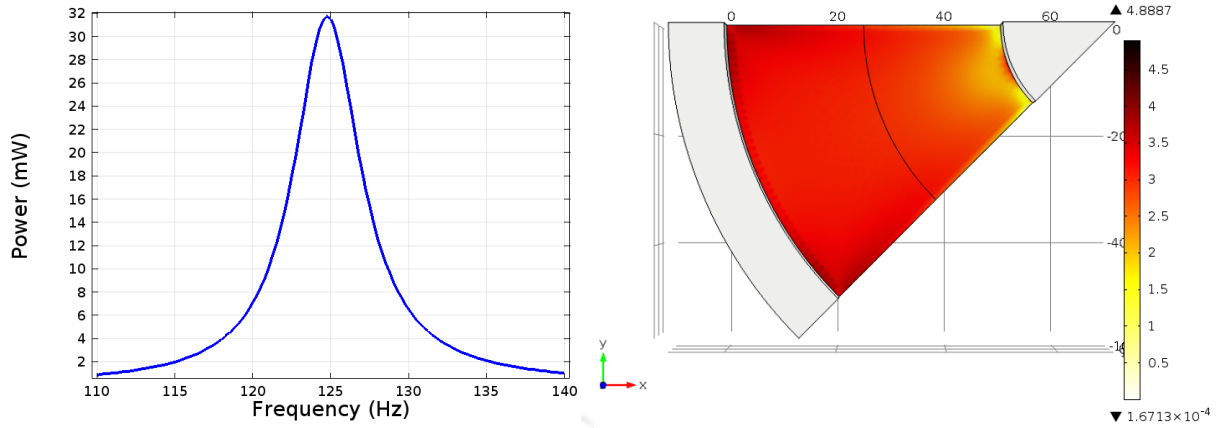

Figure 7.12: Plots of (a) total power generated in the diaphragm versus frequency and (b) stress distribution in 45º slice.

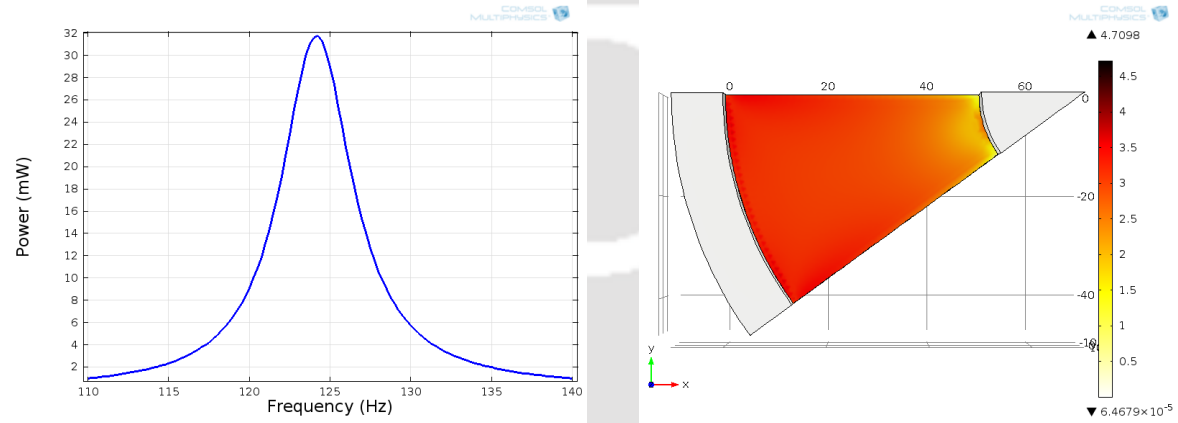

Figure 7.13: Plots of (a) total power generated in the diaphragm versus frequency and (b) stress distribution in 36º slice.

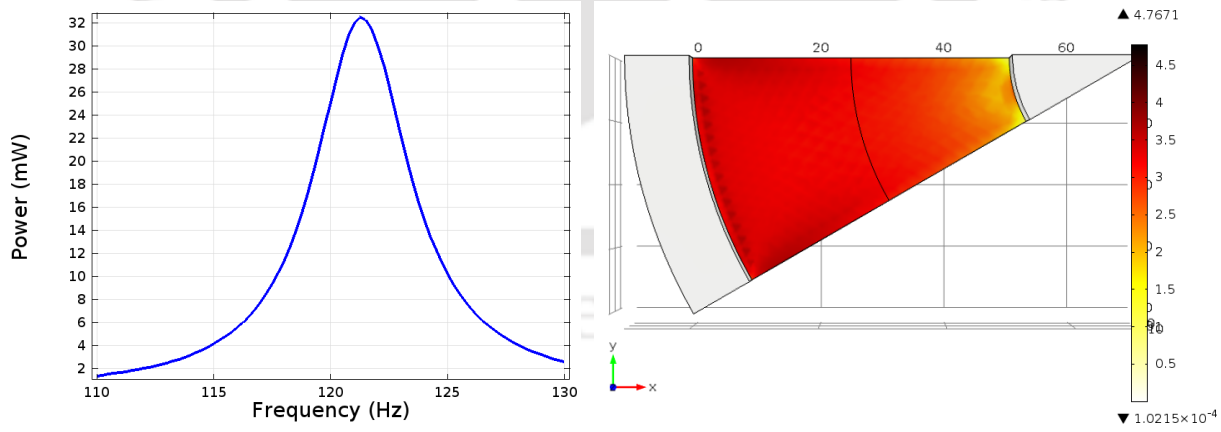

Figure 7.14: Plots of (a) total power generated in the diaphragm versus frequency and (b) stress distribution in 20º slice.

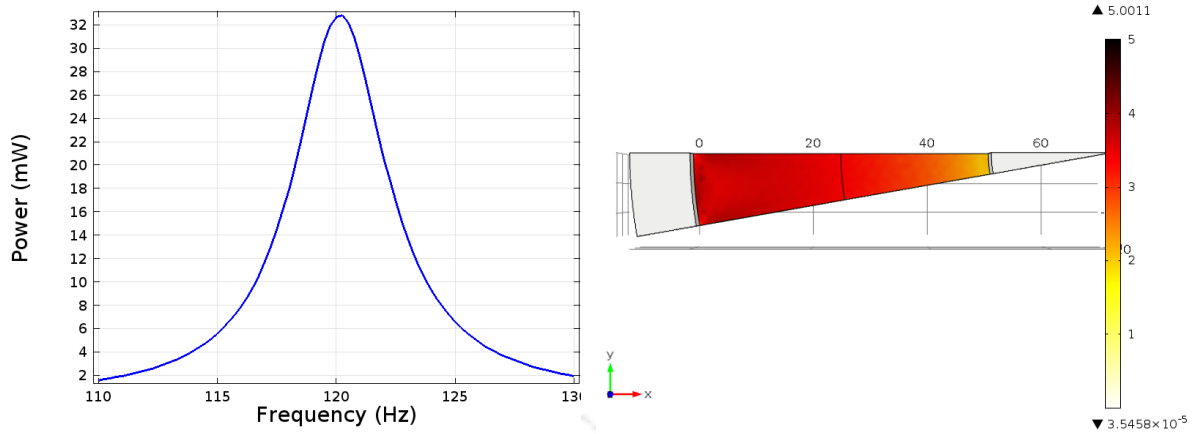

Figure 7.15: Plots of (a) total power generated in the diaphragm versus frequency and (b) stress distribution in 10^{o} slice.

The 120^{o} slice shows a resonance frequency of 155.25 Hz and three such slices form the complete diaphragm and generate total electrical power of 25.53 mW across an optimal load resistance of 500 Ω. The generated power is 63.88% higher than that of the conventional undivided diaphragm-based PVEH. Similarly, the results from other angular slices show that slicing has improved the overall power generation capability of the diaphragm without sacrificing any additional volume or mass. The stress on the slices are also very well distributed all over the surface compared to the conventional diaphragm. In Table 7.2, the mechanical and electrical performances of all the angular slices are compared, and the optimal slicing angle for efficient power generation is determined. In, Table 7.2 it is observed that the generated power for the conventional diaphragm is 15.58 mW, and slicing the diaphragm into integral number (n) of identical slices results in increase in the total output power. The generated power is lowest for the 180^{o} slice and increases as the number of slices (n) increases. Thus, the generated power is found to be proportional to the number of slices (n) but, a large value of n will increase stress on the surface as well as the operational and wiring difficulty. Thus, we have to pick a suitable angle of slicing that should generate a decent amount of power without compromising reliability.

Table 7.2: Performance comparison of diaphragm divided in different *n* number of slices.

Number of equal sections (*n*)	Slicing angle	Resonance frequency (Hz)	Displacement of mass (μm)	Total generated power (mW)	Power density (mW/cm^3)	Increase in power density (%)	Maximum stress (MPa)	Power per unit stress (mW/MPa)
1	360^o	284.00	16.44	15.58	0.261	-----	3.70	4.210
2	180^o	202.50	48.07	18.51	0.310	18.80	9.18	2.016
3	120^o	155.25	68.85	25.53	0.428	63.88	7.32	3.488
4	90^o	138.50	82.70	28.64	0.480	83.82	5.25	5.455
5	72^o	132.00	94.92	30.30	0.508	94.48	4.22	7.180
6	60^o	127.50	104.50	30.72	0.515	97.17	4.12	7.474
7	51.4^o	126.00	105.48	31.55	0.529	102.61	3.89	8.110
8	45^o	124.50	106.00	31.68	0.531	103.33	3.73	8.516
9	40^o	124.00	104.23	31.68	0.532	103.53	3.56	8.899
10	36^o	123.25	104.98	31.95	0.535	105.07	3.52	9.077
11	32.7^o	122.75	105.54	31.97	0.536	105.27	3.49	9.156
12	30^o	122.00	111.30	31.98	0.536	105.26	3.59	8.908
13	27.6^o	122.00	111.77	32.06	0.539	106.45	3.62	8.856
14	25.7^o	121.75	112.56	32.28	0.541	107.33	3.63	8.894
15	24^o	121.50	112.41	32.40	0.543	107.96	3.61	8.950
16	22.5^o	121.50	113.72	32.38	0.543	107.85	3.65	8.872
18	20^o	121.25	115.00	32.28	0.543	107.96	3.67	8.820
20	18^o	121.00	115.72	32.40	0.546	109.24	3.70	8.828
24	15^o	120.50	118.00	32.45	0.547	109.50	3.72	8.818
30	12^o	120.50	119.00	32.60	0.548	109.88	3.76	8.811
36	10^o	120.00	121.00	32.64	0.548	109.80	3.79	8.774
40	9^o	120.00	121.00	32.70	0.550	110.52	3.81	8.697
45	8^o	120.00	121.70	32.69	0.551	110.84	3.82	8.625
60	6^o	120.00	123.00	32.80	0.553	111.81	3.85	8.609
90	4^o	119.75	124.60	32.85	0.551	110.84	3.94	8.599
120	3^o	119.75	125.32	33.00	0.551	111.04	4.20	8.571
180	2^o	119.50	126.01	32.85	0.551	110.84	4.25	8.338
360	1^o	119.50	126.70	32.88	0.552	111.19	4.40	7.829

7.3.3 Optimal slicing angle

Figure 7.16 shows the variation of peak stress on the surface and power density for different slicing angles. The optimal angle for the slicing is selected based on the results from and Figure 7.16. It is observed that the generated power increases by more than 100% for slicing angles less than 51.4^o (n = 7). On the other hand, the peak value of stress initially decreases with the decrease in slicing angle and shows a minimum for the 32.7^o (n = 11), and increases with further decrease in slicing angle. Thus, the optimal angle to cut the diaphragm is 32.7^o, resulting in 11 identical slices, as shown in Figure 7.17.

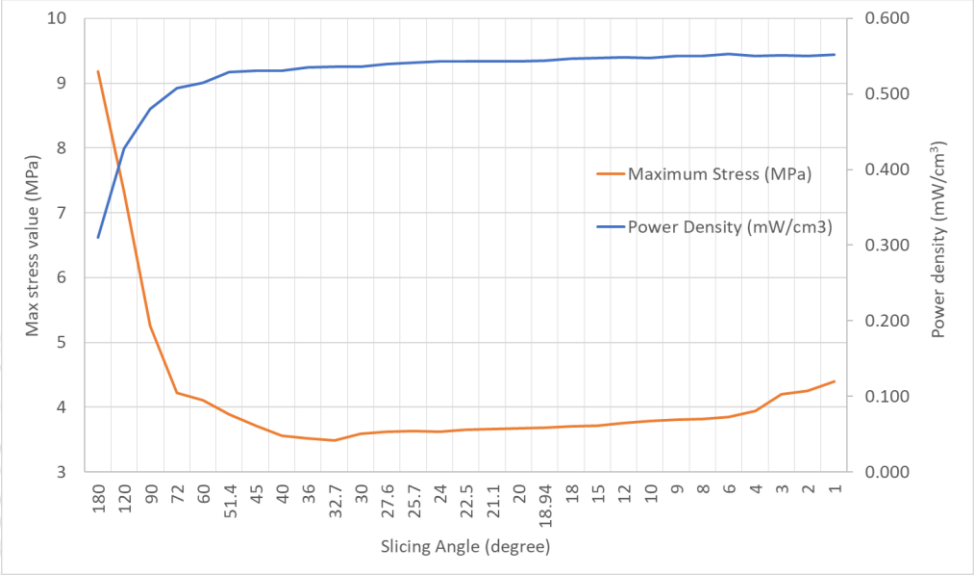

Figure 7.16: Variation of peak stress and power density with slicing angle.

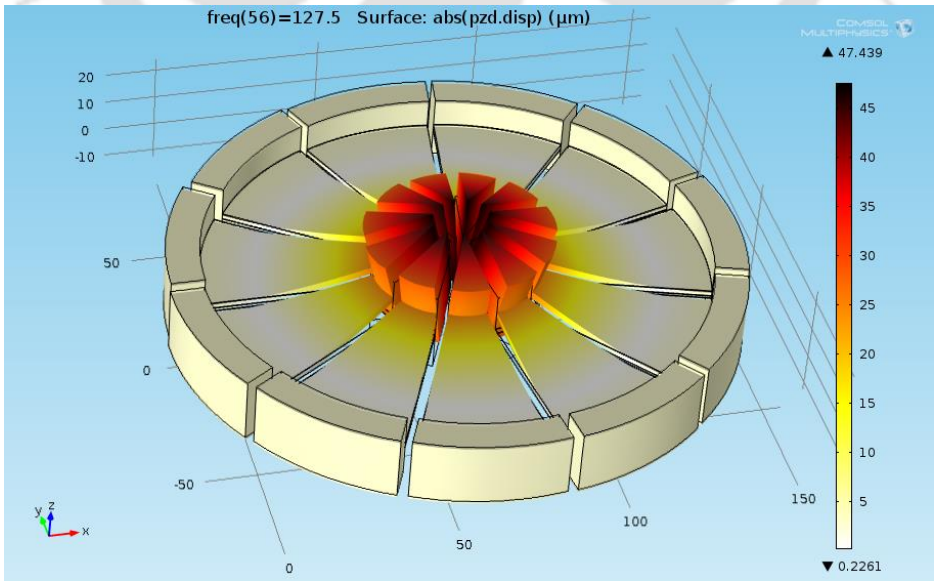

Figure 7.17: Displacement profile of 32.7^o slices from FE simulation.

The plot of total generated power versus frequency for the conventional diaphragm and corresponding divided diaphragm sliced with 32.7° (n = 11) is shown in Figure 7.18.

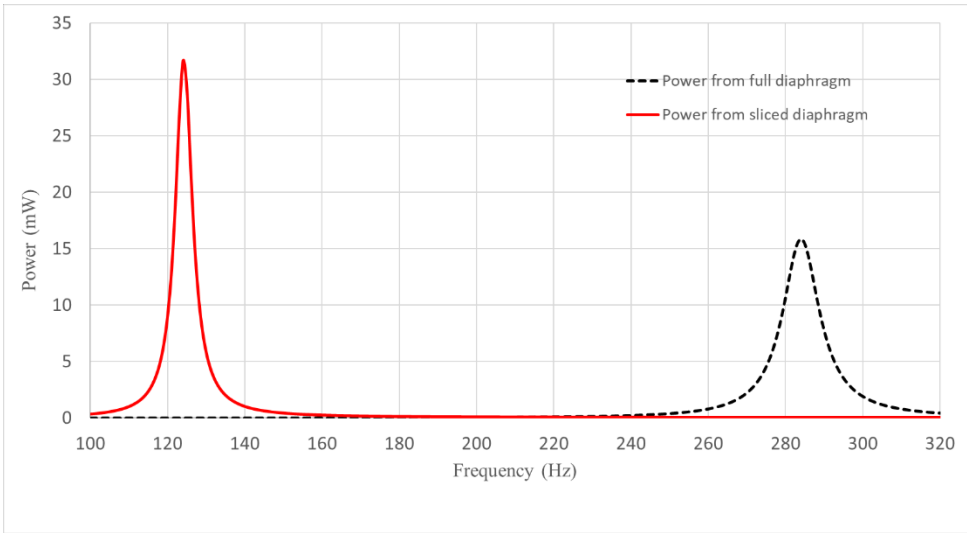

Figure 7.18: Plot of generated power versus frequency from the conventional diaphragm and divided diaphragm sliced with 32.7°.

The divided diaphragm sliced with 32.7° consists of 11 identical slices, and the resonance frequency is 122.75 Hz for all the slices. Each 32.7° slice generates 2.91 mW of power for an optimal resistance of 1.43 kΩ, and the total generated power from all the slices is 31.97 mW. Since the conventional diaphragm generates only 15.58 mW of power, cutting the diaphragm into 11 equal pieces will increase the generated power by 105%.

Since the angular slices are more like width-tapered PVEH, consequently, the stress on the piezoelectric material surface is well distributed along the entire length. Figure 7.19 shows the distribution of stress on the sliced diaphragm surface.

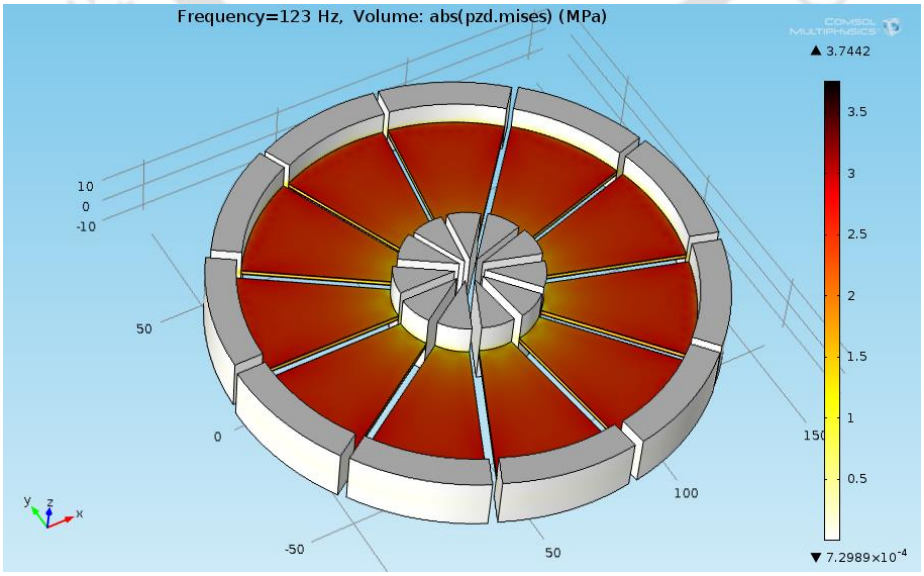

Figure 7.19: Stress distribution on the 32.7° slices.

7.4 BROADBAND PVEH USING ANGULAR SLICES

A PVEH with a resonant structure suffers from a narrow bandwidth problem. As the source vibration frequency shifts away from the system resonance frequency, the output power falls significantly. To minimize this effect of frequency dependency, researchers have used multiple resonant structures of different frequencies together [108], [130], [157]–[161] for PVEH applications. In the above study, we have observed that the slices of different angles exhibit different resonance frequencies. Thus, a set of different angular slices can be combined to obtain a broadband energy harvester.

7.4.1 Design of the broadband PVEH

In the broadband PVEH design, the following requirements are kept in mind.

- The energy harvester should generate power from a wide range of input frequencies.
- The generated power should be uniform in the entire frequency range of the harvester.
- The summation of angles of all the slices should be 360^o.

With the above design requirement in mind, a broadband PVEH is designed using five different angular slices of different resonance frequencies. The slice angles are selected so that the energy harvester should be able to harvest from 120 Hz to 140 Hz frequency, and all the slices should generate almost equal power. The broadband frequency range of 120 Hz to 140 Hz is selected because the slices from 90^o to 10^o show resonance frequency in that range. Table 7.3 shows the details of the slices used in the design of broadband PVEH.

Table 7.3: Details of the angular slices used to design broadband PVEH.

Slicing angle	Number of slices used in the design	Total angle covered	Resonance frequency (Hz)	Optimal load resistance (Ω)	Total expected power (mW)
84^o	1	84^o	137.75	620	7
72^o	1	72^o	132.00	650	6
60^o	1	60^o	127.50	700	5.1
36^o	2	72^o	123.25	675	6.4
12^o	6	72^o	120.5	625	6.5

The slices mentioned in Table 7.3 are used, and FE analysis is carried out to study the performances. The 3-D view of the broadband energy harvester geometry is shown in Figure 7.20. A set of five corresponding optimal load resistances mentioned in Table 7.3 is used.

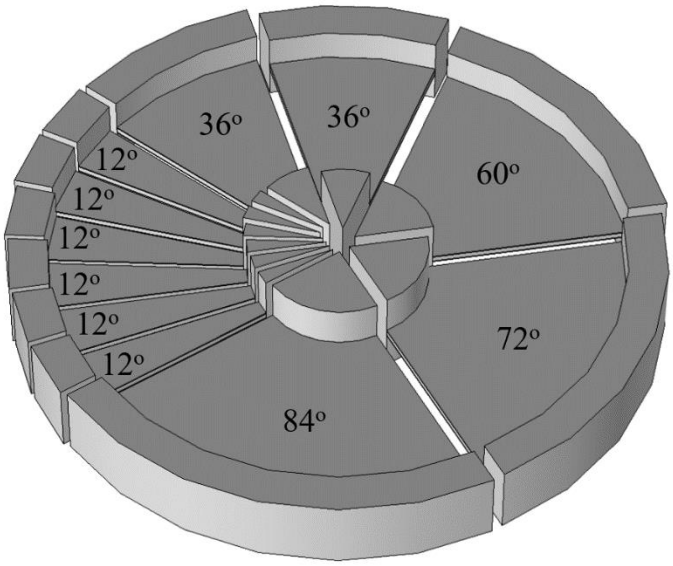

Figure 7.20: A 3-D view of the broadband PVEH geometry.

7.5. RESULTS FROM THE BROADBAND PVEH

The FE analysis of the above geometry is carried out using the same procedure as described in the earlier chapters. A sinusoidal input excitation of varying frequency and constant acceleration of 0.2*g* is applied to all the bases, and frequency domain analysis is carried out. The results from the above-designed broadband PVEH are discussed in the following subsections.

7.5.1 Displacement of the proof mass

The angular slices of different angles show different resonance frequencies and are responsible for power generation around their respective resonance frequencies. Figure 7.21 shows the displacement of the mass for different angular slices.

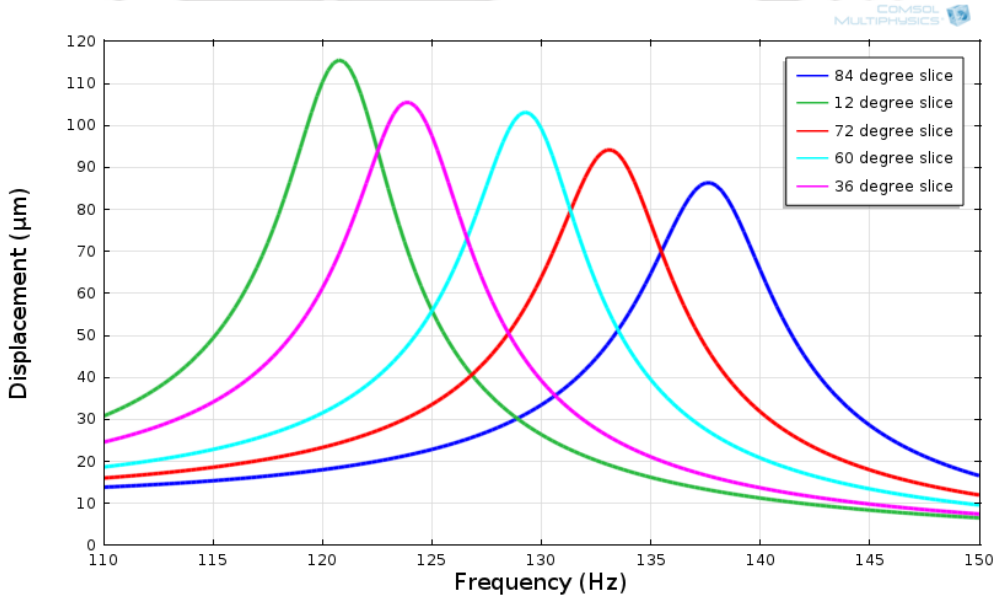

Figure 7.21: Displacement of the mass for different angular slices.

7.5.2 Stress on the surfaces

As the angular slices of different angles show different resonance frequencies, the displacement is also different. A higher displacement develops more stress on the surface and generates higher power. The designed broadband PVEH experiences different stress for different frequencies. The stress profiles on the surface of slices are shown in Figure 7.22 (a), (b), (c), (d), and (e) for input frequencies 120 Hz, 125 Hz, 130 Hz, 135 Hz, and 140 Hz respectively. The stress distribution profile shows that a particular input frequency excites a particular set of angular slices.

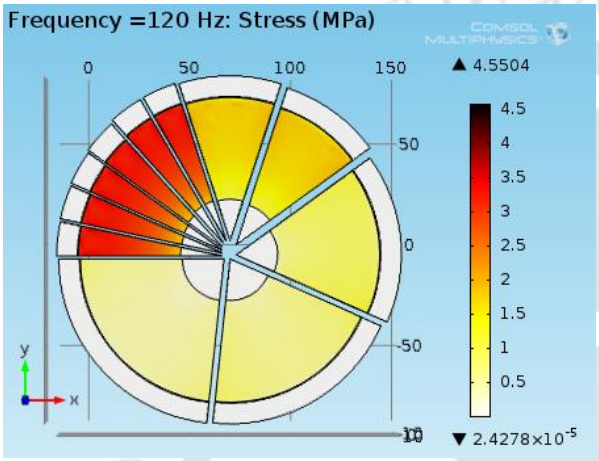

(a)

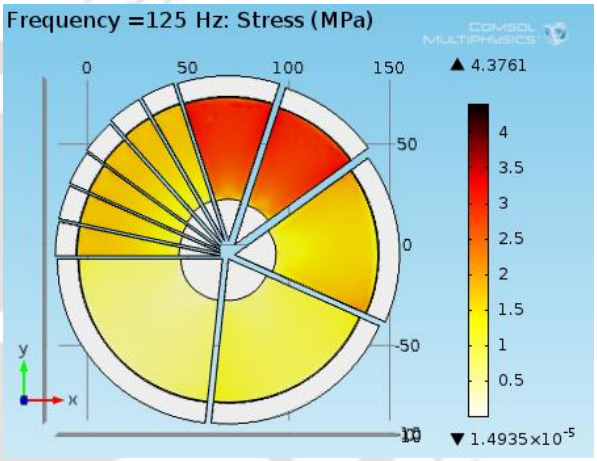

(b)

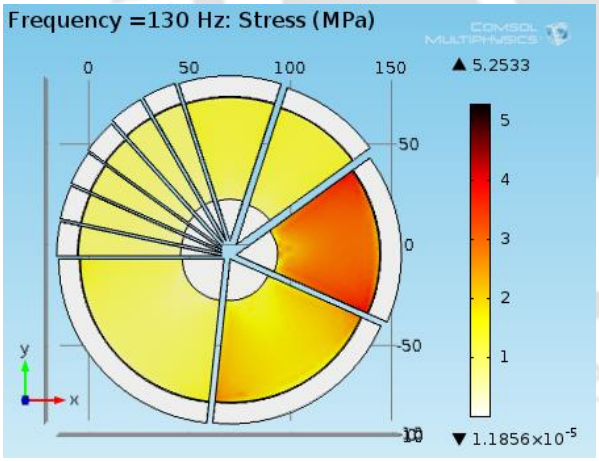

(c)

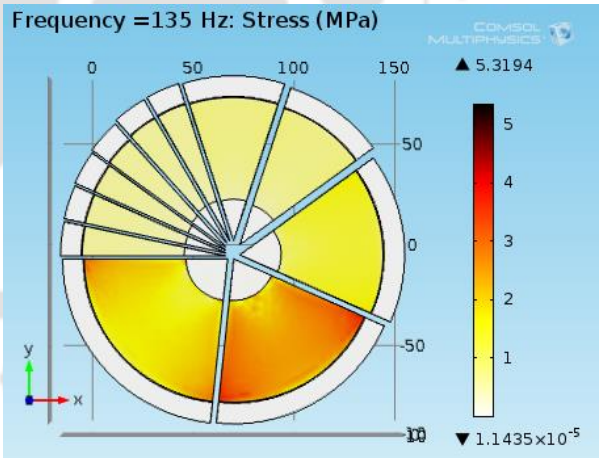

(d)

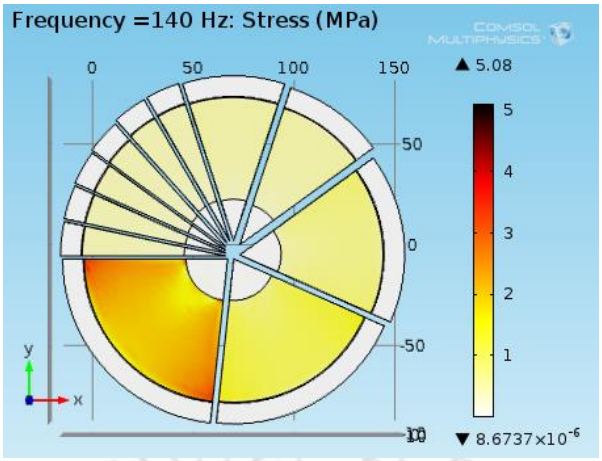

(e)

Figure 7.22: Stress profile on the surface for input frequencies (a) 120 Hz, (b) 125 Hz, (c) 130 Hz, (d) 135 Hz, and (e) 140 Hz.

7.5.3 Generated power from the broadband PVEH

As the angular slices of different angles experience stress at different frequencies, the generated power is also different for different frequencies. The individual power from the slices and the total power are plotted against input frequency in Figure 7.23. The plot shows that the energy harvester can generate electrical power for a wide range of input frequencies (120-140 Hz).

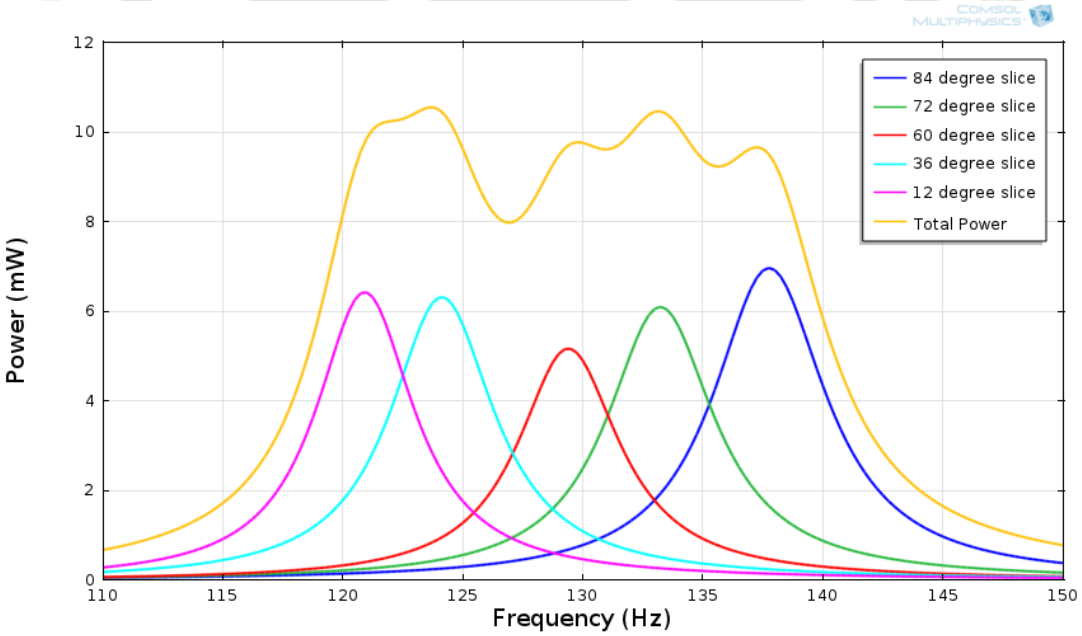

Figure 7.23: Plot of generated power versus frequency for individual slices and their combination.

7.6 Advantages of using slices

The conventional diaphragm-based PVEH has a higher resonance frequency of vibration. The stress on the diaphragm is concentrated at the central portion only and generates most of the

electrical power. The voltage generated on the diaphragm surface is of opposite polarity, i.e., if the voltage is positive at the central portion, then the voltage at the outer side will be negative. Hence, we need two sets of electrodes to harvest electrical power from conventional diaphragm-based PVEH. After dividing the diaphragm-based PVEH into angular slices of 32.7^0 each the power is increased by 105%. The proposed sliced-PVEH has the following advantages over the conventional diaphragm-based PVEH.

- The Resonance frequency of vibration is lower than the intact diaphragm.
- It can generate more than double electrical power.
- The stress distribution is almost uniform.
- The generated voltage is of the same polarity, hence no need to use separate sets of electrodes.

7.7 POSSIBLE FABRICATION APPROACH FOR THE DIAPHRAGM-BASED PVEH

The conventional diaphragm-based PVEH can be machined to introduce radial cuts into the desired angular slices.

7.8 CONCLUSIONS

An FE analysis of the diaphragm-based PVEH is carried out. A diaphragm-based PVEH generally has a high resonance frequency of vibration, and the stress distribution on the diaphragm is mainly concentrated at the central portion only and responsible for most of the generated electrical power. We have introduced radial cuts on the diaphragm to produce eleven identical angular slices of 32.7^o and found that the sliced PVEH has lower resonance frequency and generates more electrical power. The observed increase in power is 105% more than the intact diaphragm-based PVEH. The slices of different angles are proposed in order to obtain a broadband PVEH.

CHAPTER 8

CONCLUSIONS AND FUTURE SCOPE

The thesis presents geometrical modification of conventional PVEH to improve output performance. The thickness profile of the cantilever-based PVEH is modified to obtain uniform stress distribution on the piezoelectric material along the beam length and two geometries are proposed. The first proposed geometry PVEH-1 consists of a thickness-tapered substrate layer sandwiched between two piezoelectric layers of uniform thickness. The second geometry PVEH-2 consists of a substrate layer of uniform thickness sandwiched between two thickness-tapered piezoelectric layers. The thesis also presents modification of diaphragm-based PVEH to reduce resonance frequency and higher throughput by introducing radial cuts in the diaphragm. The optimal slicing angle for the best performance at a given frequency is found and a broadband PVEH using several slices of different angles is proposed.

Chapter-1 presents an introduction to the PVEH and covers a brief background of piezoelectric materials and different energy harvesting techniques. It also presents literature review for various types of PVEH and different geometrical modifications adopted to improve stress distribution.

In Chapter 2, conventional PVEH with bimorph piezoelectric layers and an end-mass is modeled and simulated using finite element (FE) analysis software. A piezoelectric-circuit coupled model is developed and simulated for Eigenmode frequency analysis to obtain the resonance frequency of vibration for open and short circuit conditions. The FE model is also analyzed for time domain and frequency domain responses of the PVEH with respect to the sinusoidal input excitation. The FE analysis results are verified with the published experimental and analytical results.

In chapter 3, an analytical model is derived for the one-dimensional vibration of a PVEH consisting of piezoelectric bimorph cantilever with an end-mass. The model can be used to study series-connected as well as parallel-connected piezoelectric layers. The analytical model can estimate the harvested electrical power across a resistive load due to input sinusoidal base

excitation. It can also be used to estimate resonance frequency of vibration, displacement of end-mass, and stress on the piezoelectric material. The effect of load resistance on the end-mass displacement and output power is studied. The results from the derived analytical expressions are verified with the results from FE analysis of the same PVEH.

Chapter 4 presents an analytical derivation of the optimal thickness profile for cantilever-based PVEH to achieve uniform stress along the beam length. The stress uniformity ensures that the entire piezoelectric material on the beam surface experiences the same level of stress. In the proposed geometry, width is kept constant while the thickness is optimized. The proposed thickness profile is further used to design two separate PVEH geometries, PVEH-1 and PVEH-2. The PVEH-1, consists of a substrate of tapered thickness profile and two piezoelectric layers of uniform thickness, and the PVEH-2 consists of a substrate of uniform thickness and two piezoelectric layers of tapered thickness.

Chapter 5 presents the derivation of analytical expressions for the proposed geometry PVEH-1. Analytical expressions are derived for the end-mass displacement, resonance frequency, generated voltage, and power. The analytical model can be used to study series-connected as well as parallel-connected piezoelectric layers. The results from the derived analytical expressions are verified with the results from FE analysis. The performance of the proposed PVEH-1 is compared with the equivalent conventional PVEH of uniform thickness. The proposed PVEH-1 can generate 19% more power than the equivalent conventional PVEH with uniform thickness under identical input conditions. Since the stress in the proposed PVEH-1 is uniformly distributed, the peak stress is 32% less compared to the conventional PVEH. When excited with equal peak stress, the proposed PVEH-1 generates 152% more power than the equivalent conventional PVEH.

In chapter 6, the derivation of analytical expressions for the proposed PVEH-2 is presented. Analytical expressions are derived to estimate the end-mass displacement, resonance frequency, generated voltage, and output power. The results from the derived analytical expressions are verified with the results from FE analysis. The proposed PVEH-2 generates 14.7% more power than the equivalent conventional PVEH with uniform thickness under identical input conditions. Since the stress in the proposed PVEH-2 is uniformly distributed, the peak stress is 31% less compared to the conventional PVEH. The proposed PVEH-2 generates 141.6% more power when excited with equal peak stress than the equivalent conventional PVEH. Both the proposed PVEHs are compared in terms of performances and suitability. For the same input acceleration, the peak stress on PVEH-2 is more and it generates more power. For a given acceleration, PVEH-

1 will experience lower stress, therefore PVEH-1 will be a better choice to deploy when acceleration levels are high.

In chapter 7, a circular diaphragm-based PVEH is simulated using finite element analysis. The modeled diaphragm is a bimorph parallel-connected energy harvester with resistive load. Initially, the conventional diaphragm is simulated to estimate the total harvested electrical power, and subsequently, the diaphragm is divided into integral number of identical angular slices, and performance is studied. It is found that the slicing of the diaphragm increases the generated power, and an optimal slicing angle for high power and minimum stress is found to be 32.7^{o}. The PVEH with optimal slicing gives 105% more power than the conventional diaphragm-based PVEH. A broadband PVEH is designed by combination of slices of different angles. The proposed broadband PVEH can be operated in a frequency range of 120 Hz to 140 Hz.

Compared to conventional PVEH, the proposed PVEH-1 and PVEH-2 show considerable improvement in harvested power and at the same time exhibit lower peak stress on the beam surface. The lower stress on the beam increases device reliability from mechanical failure. It also enables the device to be used for higher input acceleration. Though the proposed devices are comparatively difficult to fabricate, once fabricated the advantage of extra harvested power will compensate the fabrication cost.

Compared to width-tapered PVEH, the advantage of the proposed PVEH is that it occupies less volume resulting in higher power density and will be preferred where space constraint is major issue, in spite of difficulty in fabrication.

Following are possible future research directions of the present work

- The analytical expressions for the proposed PVEH-1 and PVEH-2 are derived for the first vibration mode only. It is possible to harvest electrical energy from higher-order modes of vibrations, analytical expressions can be derived for the higher-order modes of vibrations.
- Performances of the proposed geometries are verified with FE simulations. Fabrication and testing of all the proposed devices may be carried out.
- Only resistive load is considered in this thesis, however, PVEH with other kinds of loads can also be studied.
- In diaphragm-based broadband PVEH, 5 separate optimal load resistances are used. Different angular slices can be combined in series and parallel connections to study the effect on the bandwidth changes.

PUBLICATIONS

Journals:

[1] Sushanta Kundu and Harshal B. Nemade, "Piezoelectric vibration energy harvester with tapered substrate thickness for uniform stress," *Microsystem Technologies, Springer*, vol. 27, no. 1, pp. 105–113, 2021, doi: 10.1007/s00542-020-04922-6.

[2] Sushanta Kundu and Harshal B. Nemade, "Modeling and simulation of a piezoelectric vibration energy harvester," *Procedia Engineering, Elsevier*, vol. 144, pp. 568–575, 2016. doi: 10.1016/j.proeng.2016.05.043.

Conferences:

[1] Sushanta Kundu and Harshal B. Nemade, "Vibration energy harvester based on thickness-tapered Cantilever," Presented in COMSOL conference, Pune, India, 29–30 Oct. 2015.

[2] Sushanta Kundu and Harshal B. Nemade, "Modeling and simulation of a piezoelectric vibration energy harvester," Presented in 12th ICOVP 2015, IIT Guwahati, India, 14–17 Dec. 2015.

[3] Sridevi Gugulothu, Gaurav Kumar, Sushanta Kundu, Harshal B. Nemade, and Gaurav Trivedi, "Design of a next generation framework for MEMS devices," Presented in 2017 Devices for Integrated Circuit, Kalyani, India, 23–24 Mar. 2017.

BIBLIOGRAPHY

[1] J. R. Farmer, "A comparison of power harvesting techniques and related energy storage issues," M.S. thesis, Mech. Eng. Dept. Virginia Polytechnic Inst. and State Univ., Virginia, 2007, Accessed on: Dec. 14, 2021 [Online] Available: https://vtechworks.lib.vt.edu/bitstream/handle /10919/33072/Farmer_Thesis_05_15_2007_v2.pdf?sequence=1&isAllowed=y.

[2] C. Covaci and A. Gontean, "Piezoelectric energy harvesting solutions: A review," *Sensors (Switzerland)*, vol. 20, no. 12, pp. 1–37, 2020, doi: 10.3390/s20123512.

[3] Z. Yang, S. Zhou, J. Zu, and D. Inman, "High-performance piezoelectric energy harvesters and their applications," *Joule*, vol. 2, no. 4, pp. 642–697, 2018, doi: 10.1016/j.joule.2018.03.011.

[4] T. Torfs *et al.*, "Low power wireless sensor network for building monitoring," *IEEE Sens. J.*, vol. 13, no. 3, pp. 909–915, 2013, doi: 10.1109/JSEN.2012.2218680.

[5] P. C. Fitzgerald *et al.*, "Scour damage detection and structural health monitoring of a laboratory-scaled bridge using a vibration energy harvesting device," *Sensors*, vol. 19, no. 11. 2019, doi: 10.3390/s19112572.

[6] P. R. Bhaskaran, J. D. Rathnam, S. Koilmani, and K. Subramanian, "Multiresonant frequency piezoelectric energy harvesters integrated with high sensitivity piezoelectric accelerometer for bridge health monitoring applications," *Smart Mater. Res.*, vol. 2017, id. 6084309, 2017, doi: 10.1155/2017/6084309.

[7] A. Nair and C. S. Cai, "Acoustic emission monitoring of bridges: Review and case studies," *Eng. Struct.*, vol. 32, no. 6, pp. 1704–1714, 2010, doi: https://doi.org/10.1016/j.engstruct.2010. 02.020.

[8] J. Li, S. Jang, and J. Tang, "Implementation of a piezoelectric energy harvester in railway health monitoring," in *Proc.SPIE*, 2014, vol. 9061, doi: 10.1117/12.2045224.

[9] M. Gao, P. Wang, Y. Cao, R. Chen, and D. Cai, "Design and verification of a rail-borne energy harvester for powering wireless sensor networks in the railway industry," *IEEE Trans. Intell. Transp. Syst.*, vol. 18, no. 6, pp. 1596–1609, 2017, doi: 10.1109/TITS.2016.2611647.

[10] A. Somov, Z. J. Chew, T. Ruan, Q. Li, and M. Zhu, "Piezoelectric energy harvesting powered WSN for aircraft structural health monitoring," in *2016 15th ACM/IEEE International Conference on Information Processing in Sensor Networks (IPSN)*, pp. 1–2, 2016.

[11] L. Janak, Z. Ancik, J. Vetiska, and Z. Hadas, "Thermoelectric generator based on mems module as an electric power backup in aerospace applications," *Mater. Today Proc.*, vol. 2, no. 2, pp. 865–870, 2015, doi: 10.1016/j.matpr.2015.05.112.

[12] M. Gao, P. Wang, Y. Wang, and L. Yao, "Self-powered zigbee wireless sensor nodes for railway condition monitoring," *IEEE Trans. Intell. Transp. Syst.*, vol. 19, no. 3, pp. 900–909, 2018, doi: 10.1109/TITS.2017.2709346.

[13] C. R. Bowen and M. H. Arafa, "Energy harvesting technologies for tire pressure monitoring systems," *Adv. Energy Mater.*, vol. 5, no. 7, p. 1401787, 2015.

[14] H. J. Song, Y. T. Choi, G. Wang, and N. M. Wereley, "Energy harvesting utilizing single crystal pmn-pt material and application to a self-powered accelerometer," *J. Mech. Des.*, vol. 131, no. 9, Aug. 2009, doi: 10.1115/1.3160311.

[15] J. P. Lynch and K. J. Loh, "A summary review of wireless sensors and sensor networks for structural health monitoring," *Shock Vib. Dig.*, vol. 38, no. 2, pp. 91–130, 2006.

[16] T. Quan, X. Wang, Z. L. Wang, and Y. Yang, "Hybridized electromagnetic-triboelectric nanogenerator for a self-powered electronic watch," *ACS Nano*, vol. 9, no. 12, pp. 12301–12310, Dec. 2015, doi: 10.1021/acsnano.5b05598.

[17] Z. Yang, S. Zhou, J. Zu, and D. Inman, "High-performance piezoelectric energy harvesters and their applications," *Joule*, vol. 2, no. 4, pp. 642–697, 2018.

[18] C. Kompis and S. Aliwell, "Energy harvesting technologies to enable remote and wireless sensing." London: KTN, pp. 25–32, 2008.

[19] V. Raghunathan, A. Kansal, J. Hsu, J. Friedman, and M. Srivastava, "Design considerations for solar energy harvesting wireless embedded systems," in *IPSN 2005. Fourth International Symposium on Information Processing in Sensor Networks, 2005.*, pp. 457–462, 2005, doi: 10.1109/IPSN.2005.1440973.

[20] Y. K. Tan and S. K. Panda, "Energy harvesting from hybrid indoor ambient light and thermal energy sources for enhanced performance of wireless sensor nodes," *IEEE Trans. Ind. Electron.*, vol. 58, no. 9, pp. 4424–4435, 2011, doi: 10.1109/TIE.2010.2102321.

[21] S. Priya, "Advances in energy harvesting using low profile piezoelectric transducers," *J. Electroceramics*, vol. 19, no. 1, pp. 165–182, 2007, doi: 10.1007/s10832-007-9043-4.

[22] D. Shen, "Piezoelectric energy harvesting devices for low frequency vibration applications," Ph.D. thesis, Dept. of Material Eng. Auburn University, Alabama, 2009. Accessed on: Dec. 17, 2021 Available:https://etd.auburn.edu/bitstream/handle/10415/1603/Shen_Dongna_6.pdf?sequence=1&is Allowed=y

[23] S. Roundy, P. K. Wright, and J. Rabaey, "A study of low level vibrations as a power source for wireless sensor nodes," *Comput. Commun.*, vol. 26, no. 11, pp. 1131–1144, 2003, doi: 10.1016/S0140-3664(02)00248-7.

[24] G. J. Snyder, "Thermoelectric energy harvesting," in *Energy Harvesting Technologies*, 1st ed, vol. 21, D. J. Inman and S. Priya, Ed. New York: Springer, 2009, pp. 325–327.

[25] K. A. Cook-Chennault, N. Thambi, and A. M. Sastry, "Powering MEMS portable devices— A review of non-regenerative and regenerative power supply systems with special emphasis on piezoelectric energy harvesting systems," *Smart Mater. Struct.*, vol. 17, no. 4, p. 043001, 2008, doi: 10.1088/0964-1726/17/4/043001.

[26] S. P. Beeby *et al.*, "A micro electromagnetic generator for vibration energy harvesting," *J. Micromechanics Microengineering*, vol. 17, no. 7, pp. 1257–1265, 2007, doi: 10.1088/0960-1317/17/7/007.

[27] R. Amirtharajah and A. P. Chandrakasan, "Self-powered signal processing using vibration-based power generation," *IEEE J. Solid-State Circuits*, vol. 33, no. 5, pp. 687–695, 1998, doi: 10.1109/4.668982.

[28] S. Meninger, J. O. Mur-Miranda, R. Amirtharajah, A. P. Chandrakasan, and J. H. Lang, "Vibration to electric energy conversion," *IEEE Trans. Very Large Scale Integr. Syst.*, vol. 9, no. 1, pp. 64–76, 2001, doi: 10.1109/92.920820.

[29] P. D. Mitcheson, E. M. Yeatman, G. K. Rao, A. S. Holmes, and T. C. Green, "Energy harvesting from human and machine motion for wireless electronic devices," *Proc. IEEE*, vol. 96, no. 9, pp. 1457–1486, 2008, doi: 10.1109/JPROC.2008.927494.

[30] I. Kuehne, A. Frey, D. Marinkovic, G. Eckstein, and H. Seidel, "Power MEMS— A capacitive vibration-to-electrical energy converter with built-in voltage," *Sensors Actuators A Phys.*, vol. 142, no. 1, pp. 263–269, 2008, doi: https://doi.org/10.1016/j.sna.2007.02.036.

[31] S. R. Anton and H. A. Sodano, "A review of power harvesting using piezoelectric materials (2003–2006)," *Smart Mater. Struct.*, vol. 16, no. 3, pp. R1–R21, 2007, doi: 10.1088/0964-1726/16/3/R01.

[32] S. Roundy *et al.*, "Improving power output for vibration-based energy scavengers," in *IEEE Pervasive Computing*, vol. 4, no. 1, pp. 28-36, Jan-March 2005, doi: 10.1109/MPRV.2005.14.

[33] A. Abdelkefi, A. H. Nayfeh, and M. R. Hajj, "Global nonlinear distributed-parameter model of parametrically excited piezoelectric energy harvesters," *Nonlinear Dyn.*, vol. 67, no. 2, pp. 1147–1160, 2012.

[34] C. Lan, W. Qin, and W. Deng, "Energy harvesting by dynamic unstability and internal resonance for piezoelectric beam," *Appl. Phys. Lett.*, vol. 107, no. 9, p. 93902, 2015.

[35] C. De Marqui Junior, A. Erturk, and D. J. Inman, "An electromechanical finite element model for piezoelectric energy harvester plates," *J. Sound Vib.*, vol. 327, no. 1, pp. 9–25, 2009, doi: https://doi.org/10.1016/j.jsv.2009.05.015.

[36] G. Litak, M. I. Friswell, and S. Adhikari, "Regular and chaotic vibration in a piezoelectric energy harvester," *Meccanica*, vol. 51, no. 5, pp. 1017–1025, 2016, doi: 10.1007/s11012-015-0287-9.

[37] A. Keshmiri, X. Deng, and N. Wu, "New energy harvester with embedded piezoelectric stacks," *Compos. Part B Eng.*, vol. 163, pp. 303–313, 2019, doi: https://doi.org/10.1016/j.compositesb.2018.11.028.

[38] Y. Wang, W. Chen, and P. Guzman, "Piezoelectric stack energy harvesting with a force amplification frame: Modeling and experiment," *J. Intell. Mater. Syst. Struct.*, vol. 27, no. 17, pp. 2324–2332, Feb. 2016, doi: 10.1177/1045389X16629568.

[39] J. Palosaari, M. Leinonen, J. Juuti, J. Hannu, and H. Jantunen, "Piezoelectric circular diaphragm with mechanically induced pre-stress for energy harvesting," *Smart Mater. Struct.*, vol. 23, no. 8, p. 85025, 2014, doi: 10.1088/0964-1726/23/8/085025.

[40] S. Kim, W. W. Clark, and Q.-M. Wang, "Piezoelectric energy harvesting using a diaphragm structure," in *Proc. SPIE*, 2003, vol. 5055, doi: 10.1117/12.483587.

[41] C. Mo, L. J. Radziemski, and W. W. Clark, "Analysis of piezoelectric circular diaphragm energy harvesters for use in a pressure fluctuating system," *Smart Mater. Struct.*, vol. 19, no. 2, p. 25016, 2010, doi: 10.1088/0964-1726/19/2/025016.

[42] X. Hu, Y. Li, and X. Xie, "A study on a U-shaped piezoelectric coupled beam and its corresponding ingenious harvester," *Energy*, vol. 185, pp. 938–950, 2019, doi: https://doi.org/10.1016/j.energy.2019.07.084.

[43] G. W. Kim, J. Kim, and J. H. Kim, "Flexible piezoelectric vibration energy harvester using a trunk-shaped beam structure inspired by an electric fish fin," *Int. J. Precis. Eng. Manuf.*, vol. 15, no. 9, pp. 1967–1971, 2014, doi: 10.1007/s12541-014-0552-1.

[44] W. B. Hobbs and D. L. Hu, "Tree-inspired piezoelectric energy harvesting," *J. Fluids Struct.*, vol. 28, pp. 103–114, 2012, doi: https://doi.org/10.1016/j.jfluidstructs.2011.08.005.

[45] X. He, D. Li, H. Zhou, X. Hui, and X. Mu, "Theoretical and experimental studies on MEMS variable cross-section cantilever beam based piezoelectric vibration energy harvester," *Micromachines*, vol. 12, no. 7, 2021, doi: 10.3390/mi12070772.

[46] K. Tsuchiya, T. Kitagawa, Y. Uetsuji, and E. Nakamachi, “Fabrication of smart material PZT thin films by RF magnetron sputtering method in microactuators,” *JSME Int. Journal, Ser. A Solid Mech. Mater. Eng.*, vol. 49, no. 2, pp. 201–208, 2006, doi: 10.1299/jsmea.49.201.

[47] S. Beeby, M. Tudor, and N. White, “Energy harvesting vibration sources for microsystems applications,” *Meas. Sci. Technol.*, vol. 17, no. 12, pp. R175–R195, 2006, doi: 10.1088/0957-0233/17/12/R01.

[48] S. Beeby and W. Neil, *Energy Harvesting for Autonomous Systems*. Artech House, 2010, pp. 97–100.

[49] I. B. Kobiakov, “Elastic, piezoelectric and dielectric properties of ZnO and CdS single crystals in a wide range of temperatures,” *Solid State Commun.*, vol. 35, no. 3, pp. 305–310, 1980, doi: 10.1016/0038-1098(80)90502-5.

[50] “IEEE standard on piezoelectricity,” *ANSI/IEEE Std. 176-1987, Inst. Electr. Electron. Eng. Ultrason. Ferroelectr. Freq. Control Soc.*, 1987, doi: 10.1109/IEEESTD.1988.79638.

[51] Nader Jalili, *Piezoelectric-based vibration control: From macro to micro/nano scale systems*. Springer Science & Business Media, 2009, pp. 115–120.

[52] M. N. Fakhzan and A. G. Muthalif, “Vibration based energy harvesting using piezoelectric material,” In *2011 4th International Conference on Mechatronics (ICOM)*, pp. 1-7. IEEE, 2011. doi: 10.1109/ICOM.2011.5937182.

[53] H. S. Yoon, “Modeling, optimization, and design of efficient initially curved piezoceramic unimorphs for energy harvesting applications,” *J. Intell. Mater. Syst. Struct.*, vol. 16, no. 10, pp. 877–888, 2005, doi: 10.1177/1045389X05055759.

[54] H. Xue, Y. Hu, and Q. Wang, “Broadband piezoelectric energy harvesting device using multiple bimorph with different operating frequencies,” *IEEE Trans. Ultrason. Ferroelectr. Freq. Control.*, vol. 55, no. 9, pp. 2104–2108, 2008.

[55] N. Chaulagain, V. Hegde, V. S. Nagaraja, and N. Veerapandi, “Design and performance analysis of piezoresistive circular diaphragm based acoustic sensor,” in *2019 Second International Conference on Advanced Computational and Communication Paradigms (ICACCP)*, 2019, pp. 1–6, doi: 10.1109/ICACCP.2019.8882960.

[56] V. Hegde, S. Veena, H. M. Ravikumar, and S. Yellampalli, “Piezoelectric acoustic pressure sensor diaphragm design for energy harvesting,” in *2014 International Conference on Advances in Energy Conversion Technologies (ICAECT)*, 2014, pp. 21–26, doi: 10.1109/ICAECT.2014.6757055.

[57] T.-C. Yuan, F. Chen, J. Yang, R.-G. Song, and Y. Kong, “A novel circular plate acoustic energy harvester for urban railway noise,” *Shock & Vib.*, 2021, p. 6647162, 2021, doi: 10.1155/2021/6647162.

[58] Z. Xiao, T. Q. Yang, Y. Dong, and X. C. Wang, “Energy harvester array using piezoelectric circular diaphragm for broadband vibration,” *Appl. Phys. Lett.*, vol. 104, no. 22, 2014, doi: 10.1063/1.4878537.

[59] H. Li, C. Tian, and Z. D. Deng, “Energy harvesting from low frequency applications using piezoelectric materials,” *Appl. Phys. Rev.*, vol. 1, no. 4, pp. 0–20, 2014, doi: 10.1063/1.4900845.

[60] Y. Yang, S. Wang, P. Stein, B.-X. Xu, and T. Yang, “Vibration-based energy harvesting with a clamped piezoelectric circular diaphragm: analysis and identification of optimal structural parameters,” *Smart Mater. Struct.*, vol. 26, no. 4, p. 45011, 2017, doi: 10.1088/1361-665x/aa5fda.

[61] T. C. Yuan, J. Yang, and L. Q. Chen, “Nonlinear dynamics of a circular piezoelectric plate for vibratory energy harvesting,” *Commun. Nonlinear Sci. Numer. Simul.*, vol. 59, pp. 651–656, 2018, doi: 10.1016/j.cnsns.2017.12.010.

[62] X. R. Chen, T. Q. Yang, W. Wang, and X. Yao, “Vibration energy harvesting with a clamped piezoelectric circular diaphragm,” *Ceram. Int.*, vol. 38, no. 1, pp. S271–S274, 2012, doi: 10.1016/j.ceramint.2011.04.099.

[63] M. Umeda, K. Nakamura, and S. Ueha, “Analysis of the transformation of mechanical impact energy to electric energy using piezoelectric vibrator,” *Japanese J. Appl. Physics*, vol. 35, no. 5, pp. 3267–3273, 1996, doi: 10.1143/jjap.35.3267.

[64] Z. Wang *et al.*, “Self-powered viscosity and pressure sensing in microfluidic systems based on the piezoelectric energy harvesting of flowing droplets,” *ACS Appl. Mater. Interfaces*, vol. 9, no. 34, pp. 28586–28595, 2017, doi: 10.1021/acsami.7b08541.

[65] M. Leinonen, J. Juuti, H. Jantunen, and J. Palosaari, “Energy harvesting with a bimorph type piezoelectric diaphragm multilayer structure and mechanically induced pre-stress,” *Energy Technol.*, vol. 4, no. 5, pp. 620–624, 2016, doi: 10.1002/ente.201500429.

[66] A. Hosseinkhani, D. Younesian, P. Eghbali, A. Moayedizadeh, and A. Fassih, “Sound and vibration energy harvesting for railway applications: A review on linear and nonlinear techniques,” *Energy Reports*, vol. 7, pp. 852–874, 2021, doi: 10.1016/j.egyr.2021.01.087.

[67] P. B. Stephen *et al.*, “A comparison of power output from linear and nonlinear kinetic energy harvesters using real vibration data,” *Smart Mater. Struct.*, vol. 22, no. 7, p. 75022, 2013, doi: 10.1088/0964-1726/22/7/075022.

[68] G. Litak, M. Borowiec, M. I. Friswell, and S. Adhikari, “Energy harvesting in a magnetopiezoelastic system driven by random excitations with uniform and Gaussian distributions,” *J. Theor. Appl. Mech.*, vol. 49, no. 3, pp. 757–764, 2011.

[69] S. F. Ali, S. Adhikari, M. I. Friswell, and S. Narayanan, “The analysis of piezomagnetoelastic energy harvesters under broadband random excitations,” *J. Appl. Phys.*, vol. 109, no. 7, pp. 1–8, 2011, doi: 10.1063/1.3560523.

[70] M. Borowiec *et al.*, “Energy harvesting in piezoelastic systems driven by random excitations,” *Int. J. Struct. Stab. Dyn.*, vol. 13, no. 7, pp. 1–11, 2013, doi: 10.1142/S0219455413400063.

[71] C. B. Williams and R. B. Yates, “Analysis of a Micro-Electric Generator for Microsystems,” *Sensors and Actuators A: Physical*, vol. 44, no. 1–3, 1995.

[72] S. P. Beeby, A. Blackburn, and N. M. White, “Processing of PZT piezoelectric thick films on silicon for microelectromechanical systems,” *J. Micromechanics Microengineering*, vol. 9, no. 3, p. 218, 1999, doi: 10.1088/0960-1317/9/3/302.

[73] P. Glynne-Jones, S. P. Beeby, and N. M. White, “Towards a piezoelectric vibration-powered microgenerator,” *IEE Proc. Sci. Meas. Technol.*, vol. 148, no. 2, pp. 68–72, 2001, doi: 10.1049/ip-smt:20010323.

[74] S. Roundy and P. K. Wright, “A piezoelectric vibration based generator for wireless electronics,” *Smart Mater. Struct.*, vol. 13, no. 5, pp. 1131–1142, 2004, doi: 10.1088/0964-1726/13/5/018.

[75] S. M. Shahruz, “Design of mechanical band-pass filters for energy scavenging,” *J. Sound Vib.*, vol. 292, no. 3, pp. 987–998, 2006, doi: https://doi.org/10.1016/j.jsv.2005.08.018.

[76] H. B. Fang *et al.*, “Fabrication and performance of MEMS-based piezoelectric power generator for vibration energy harvesting,” *Microelectronics J.*, vol. 37, no. 11, pp. 1280–1284, 2006, doi:

https://doi.org/10.1016/j.mejo.2006.07.023.

[77] Y. Hu, H. Xue, and H. Hu, "A piezoelectric power harvester with adjustable frequency through axial preloads," *Smart Mater. Struct.*, vol. 16, no. 5, pp. 1961–1966, 2007, doi: 10.1088/0964-1726/16/5/054.

[78] H. Xue, Y. Hu, and Q. Wang, "Broadband piezoelectric energy harvesting devices using multiple bimorphs with different operating frequencies," *IEEE Trans. Ultrason. Ferroelectr. Freq. Control*, vol. 55, no. 9, pp. 2104–2108, 2008, doi: 10.1109/TUFFC.903.

[79] A. Erturk and D. J. Inman, "A distributed parameter electromechanical model for cantilevered piezoelectric energy harvesters," *J. Vib. Acoust.*, vol. 130, no. 4, p. 041002, 2008, doi: 10.1115/1.2890402.

[80] A. Erturk and D. J. Inman, "Issues in mathematical modeling of piezoelectric energy harvesters," *Smart Mater. Struct.*, vol. 17, no. 6, p. 065016, 2008, doi: 10.1088/0964-1726/17/6/065016.

[81] A. Erturk and D. J. Inman, "On mechanical modeling of cantilevered piezoelectric vibration energy harvesters," *J. Intell. Mater. Syst. Struct.*, vol. 19, no. 11, pp. 1311–1325, 2008, doi: 10.1177/1045389X07085639.

[82] B. S. Lee, S. C. Lin, W. J. Wu, X. Y. Wang, P. Z. Chang, and C. K. Lee, "Piezoelectric MEMS generators fabricated with an aerosol deposition PZT thin film," *J. Micromechanics Microengineering*, vol. 19, no. 6, p. 65014, 2009, doi: 10.1088/0960-1317/19/6/065014.

[83] N. G. Elvin and A. A. Elvin, "A general equivalent circuit model for piezoelectric generators," *J. Intell. Mater. Syst. Struct.*, vol. 20, no. 1, pp. 3–9, 2009, doi: 10.1177/1045389X08089957.

[84] A. Erturk and D. J. Inman, "An experimentally validated bimorph cantilever model for piezoelectric energy harvesting from base excitations," *Smart Mater. Struct.*, vol. 18, no. 2, p. 025009, 2009, doi: 10.1088/0964-1726/18/2/025009.

[85] H. Durou, G. A. A. Rodríguez, A. Ramond, X. Dollat, C. Rossi, and D. Estève, "Micromachined bulk PZT piezoelectric vibration harvester to improve effectiveness over low amplitude and low frequency vibrations," *Proc. Power MEMS'10*, pp.27-30, Nov. 2010.

[86] J. C. Park, J. Y. Park, and Y.P. Lee, "Modeling and characterization of piezoelectric d_{33}-mode MEMS energy harvester," *J. Microelectromechanical Syst.*, vol. 19, no. 5, pp. 1215–1222, 2010, doi: 10.1109/JMEMS.2010.2067431.

[87] M. Zhu, E. Worthington, and A. Tiwari, "Design study of piezoelectric energy-harvesting devices for generation of higher electrical power using a coupled piezoelectric-circuit finite element method.," *IEEE Trans. Ultrason. Ferroelectr. Freq. Control*, vol. 57, no. 2, pp. 427–437, 2010, doi: 10.1109/TUFFC.2010.1423.

[88] V. R. Challa, M. G. Prasad, and F. T. Fisher, "Towards an autonomous self-tuning vibration energy harvesting device for wireless sensor network applications," *Smart Mater. Struct.*, vol. 20, no. 2, p. 025004, 2011, doi: 10.1088/0964-1726/20/2/025004.

[89] R. Xu *et al.*, "Fabrication and characterization of MEMS-based PZT/PZT bimorph thick film vibration energy harvesters," *J. Micromechanics Microengineering*, vol. 22, no. 9, p. 94007, 2012, doi: 10.1088/0960-1317/22/9/094007.

[90] M. Al Ahmad and G. E. Jabbour, "Electronically droplet energy harvesting using piezoelectric cantilevers," *Electron. Lett.*, vol. 48, no. 11, pp. 647–649, 2012.

[91] S. Zhao and A Erturk, "Electroelastic modeling and experimental validations of piezoelectric energy harvesting from broadband random vibrations of cantilevered bimorphs," *Smart Mater.*

Struct., vol. 22, no. 1, p. 015002, 2013, doi: 10.1088/0964-1726/22/1/015002.

[92] A. S. Alsuwaiyan, M. E. H. Eltaib, and H. A. Sherif, "Ambient vibrations piezoelectric harvester array with discrete multiple low frequencies," in *2014 2nd International Conference on Technology, Informatics, Management, Engineering & Environment*, 2014, pp. 174–178.

[93] Y. Yang, H. Wu, and C. K. Soh, "Experiment and modeling of a two-dimensional piezoelectric energy harvester," *Smart Mater. Struct.*, vol. 24, no. 12, p. 125011, 2015, doi: 10.1088/0964-1726/24/12/125011.

[94] S. Emamian, A. A. Chlaihawi, B. B. Narakathu, B. J. Bazuin, and M. Z. Atashbar, "A piezoelectric based vibration energy harvester fabricated using screen printing technique," in *2016 IEEE SENSORS*, 2016, pp. 1–3, doi: 10.1109/ICSENS.2016.7808560.

[95] S. Baishya, D. Borthakur, R. Kashyap, and A. Chatterjee, "A high precision lumped parameter model for piezoelectric energy harvesters," *IEEE Sens. J.*, vol. 17, no. 24, pp. 8350–8355, 2017, doi: 10.1109/JSEN.2017.2764165.

[96] J. Zhang, Z. Fang, C. Shu, J. Zhang, Q. Zhang, and C. Li, "A rotational piezoelectric energy harvester for efficient wind energy harvesting," *Sensors Actuators A Phys.*, vol. 262, pp. 123–129, 2017, doi: https://doi.org/10.1016/j.sna.2017.05.027.

[97] Z. Yang, A. Erturk, and J. Zu, "On the efficiency of piezoelectric energy harvesters," *Extrem. Mech. Lett.*, vol. 15, pp. 26–37, 2017, doi: 10.1016/j.eml.2017.05.002.

[98] J. Palosaari, M. Leinonen, J. Juuti, and H. Jantunen, "The effects of substrate layer thickness on piezoelectric vibration energy harvesting with a bimorph type cantilever q," *Mech. Syst. Signal Process.*, vol. 106, pp. 114–118, 2018, doi: 10.1016/j.ymssp.2017.12.029.

[99] M. Khalili, A. B. Biten, G. Vishwakarma, S. Ahmed, and A. T. Papagiannakis, "Electro-mechanical characterization of a piezoelectric energy harvester," *Appl. Energy*, vol. 253, p. 113585, 2019, doi: https://doi.org/10.1016/j.apenergy.2019.113585.

[100] E. L. Pradeesh and S. Udhayakumar, "Effect of placement of piezoelectric material and proof mass on the performance of piezoelectric energy harvester," *Mech. Syst. Signal Process.*, vol. 130, pp. 664–676, 2019, doi: https://doi.org/10.1016/j.ymssp.2019.05.044.

[101] P. Asthana and G. Khanna, "Characterization and optimization of piezoelectric bimorph cantilever structure for ambient vibration-based energy harvesting application," *Integr. Ferroelectr.*, vol. 211, no. 1, pp. 45–59, 2020, doi: 10.1080/10584587.2020.1803674.

[102] T. Kim, Y. Ko, C. Yoo, B. Choi, S. Han, and N. Kim, "Design optimisation of wide-band piezoelectric energy harvesters for self-powered devices," *Energy Convers. Manag.*, vol. 225, p. 113443, 2020, doi: https://doi.org/10.1016/j.enconman.2020.113443.

[103] J. H. Kim *et al.*, "Development of a hybrid type smart pen piezoelectric energy harvester for an IoT platform," *Energy*, vol. 222, p. 119845, 2021, doi: https://doi.org/10.1016/j.energy.2021.119845.

[104] H. W. Kim *et al.*, "Energy harvesting using a piezoelectric 'cymbal' transducer in dynamic environment," *Jpn. J. Appl. Phys.*, vol. 43, no. 9A, pp. 6178–6183, 2004, doi: 10.1143/jjap.43.6178.

[105] C. Mo, L. J. Radziemski, and W. W. Clark, "Experimental validation of energy harvesting performance for pressure-loaded piezoelectric circular diaphragms," *Smart Mater. Struct.*, vol. 19, no. 7, p. 75010, 2010, doi: 10.1088/0964-1726/19/7/075010.

[106] M. Deterre, E. Lefeuvre, and E. Dufour-Gergam, "An active piezoelectric energy extraction

method for pressure energy harvesting," *Smart Mater. Struct.*, vol. 21, no. 8, p. 85004, 2012, doi: 10.1088/0964-1726/21/8/085004.

[107] S. Mohammadi and M. Abdalbeigi, "Analytical optimization of piezoelectric circular diaphragm generator," *Adv. Mater. Sci. Eng.*, vol. 2013, p. 620231, 2013, doi: 10.1155/2013/620231.

[108] W. Wang, R. J. Huang, C. J. Huang, and L. F. Li, "Energy harvester array using piezoelectric circular diaphragm for rail vibration," *Acta Mech. Sin. Xuebao*, vol. 30, no. 6, pp. 884–888, 2014, doi: 10.1007/s10409-014-0115-9.

[109] Y. Dong, T. Yang, Z. Xiao, Y. Liu, and X. Wang, "Performance enhancement of PZT material for circular diaphragm energy harvester," *J. Mater. Sci. Mater. Electron.*, vol. 26, no. 10, pp. 7921–7926, 2015, doi: 10.1007/s10854-015-3445-x.

[110] F. Shu, T. Yang, and Y. Liu, "Enhancement of power output by a new stress-applied mode on circular piezoelectric energy harvester," *AIP Adv.*, vol. 8, no. 4, p. 45102, Apr. 2018, doi: 10.1063/1.5016200.

[111] C. Xu, Y. Li, and T. Yang, "Optimization of non-uniform deformation on piezoelectric circular diaphragm energy harvester with a ring-shaped ceramic disk," *Micromachines*, vol. 11, no. 11. 2020, doi: 10.3390/mi11110963.

[112] I. Mehdipour and F. Honarvar, "Finding the optimum polarization boundary line for enhancing the performance of clamped piezoelectric circular plates," *Appl. Math. Model.*, vol. 91, pp. 1141–1153, 2021, doi: https://doi.org/10.1016/j.apm.2020.11.008.

[113] N. M. White and N. R. Harris, "Fabrication and characterization of free-standing thick-film piezoelectric cantilevers for energy harvesting," *Measurement Science and Technology*, vol. 20, no. 12, 2009, doi: 10.1088/0957-0233/20/12/124010.

[114] H. Yu, J. Zhou, L. Deng, and Z. Wen, "A vibration-based MEMS piezoelectric energy harvester and power conditioning circuit," *Sensors (Switzerland)*, vol. 14, no. 2, pp. 3323–3341, 2014, doi: 10.3390/s140203323.

[115] M. Safaei, H. A. Sodano, and S. R. Anton, "A review of energy harvesting using piezoelectric materials: State-of-the-art a decade later (2008-2018)," *Smart Mater. Struct.*, vol. 28, no. 11, 2019, doi: 10.1088/1361-665X/ab36e4.

[116] N. Sezer and M. Koç, "A comprehensive review on the state-of-the-art of piezoelectric energy harvesting," *Nano Energy*, vol. 80, p. 105567, 2021, doi: 10.1016/j.nanoen.2020.105567.

[117] A. Sharma, O. Z. Olszewski, J. Torres, A. Mathewson, and R. Houlihan, "Fabrication, simulation and characterisation of MEMS piezoelectric vibration energy harvester for low frequency," *Procedia Eng.*, vol. 120, pp. 645–650, 2015, doi: 10.1016/j.proeng.2015.08.695.

[118] D. Gibus *et al.*, "Strongly coupled piezoelectric cantilevers for broadband vibration energy harvesting," *Appl. Energy*, vol. 277, p. 115518, 2020, doi: 10.1016/j.apenergy.2020.115518.

[119] J. Lee and B. Choi, "Development of a piezoelectric energy harvesting system for implementing wireless sensors on the tires," *Energy Convers. Manag.*, vol. 78, pp. 32–38, 2014, doi: 10.1016/j.enconman.2013.09.054.

[120] R. Hosseini, O. Zargar, and M. Hamedi, "Improving power density of piezoelectric vibration-based energy scavengers," *J. Solid Mech.*, vol. 10, no. 1, pp. 98–109, 2018.

[121] B. Wang, X. Luo, Y. Liu, and Z. Yang, "Thickness-variable composite beams for vibration energy harvesting," *Compos. Struct.*, vol. 244, p. 112232, 2020, doi: 10.1016/j.compstruct.2020.112232.

[122] J. Baker, “Alternative geometries for increasing power density in vibration energy scavenging,” *3rd Int. Energy Convers. Eng. Conf. 15 - 18 August 2005, San Fr. Calif.*, pp. 1–12, August 2005.

[123] S. Mehraeen, S. Jagannathan, and K. A. Corzine, “Energy harvesting from vibration with alternate scavenging circuitry and tapered cantilever beam,” *IEEE Transactions on Industrial Electronics*, vol. 57, no. 3, pp. 820–830, 2010.

[124] S. Ben Ayed, A. Abdelkefi, F. Najar, and M. R. Hajj, “Design and performance of variable-shaped piezoelectric energy harvesters,” *J. Intell. Mater. Syst. Struct.*, vol. 25, no. 2, pp. 174–186, 2014, doi: 10.1177/1045389X13489365.

[125] A. G. A. Muthalif and N. H. D. Nordin, “Optimal piezoelectric beam shape for single and broadband vibration energy harvesting: Modeling, simulation and experimental results,” *Mech. Syst. Signal Process.*, vol. 54–55, pp. 417–426, 2015, doi: 10.1016/j.ymssp.2014.07.014.

[126] R. Sriramdas, S. Chiplunkar, R. M. Cuduvally, and R. Pratap, “Performance enhancement of piezoelectric energy harvesters using multilayer and multistep beam configurations,” *IEEE Sens. J.*, vol. 15, no. 6, pp. 3338–3348, 2015, doi: 10.1109/JSEN.2014.2387882.

[127] R. Hosseini and M. Nouri, “Shape design optimization of unimorph piezoelectric cantilever energy harvester,” *J. Comput. Appl. Mech.*, vol. 47, no. 2, pp. 247–259, 2016, doi: 10.22059/jcamech.2017.224975.126.

[128] X. D. Xie, A. Carpinteri, and Q. Wang, “A theoretical model for a piezoelectric energy harvester with a tapered shape,” *Eng. Struct.*, vol. 144, pp. 19–25, 2017, doi: 10.1016/j.engstruct.2017.04.050.

[129] H. Salmani, G. H. Rahimi, and S. A. H. Kordkheili, “An exact analytical solution to exponentially tapered piezoelectric energy harvester,” *Shock and Vibration*, vol. 2015, Apr. 2015.

[130] A. Keshmiri and N. Wu, “A wideband piezoelectric energy harvester design by using multiple non-uniform bimorphs,” *Vibration*, vol. 1, no. 1, pp. 93–104, 2018, doi: 10.3390/vibration1010008.

[131] S. Srinivasulu Raju, S. B. Choi, M. Umapathy, and G. Uma, “An effective energy harvesting in low frequency using a piezo-patch cantilever beam with tapered rectangular cavities,” *Sensors Actuators, A: Phys.*, vol. 297, p. 111522, 2019, doi: 10.1016/j.sna.2019.07.046.

[132] E. L. Pradeesh and S. Udhayakumar, “Investigation on the geometry of beams for piezoelectric energy harvester,” *Microsyst. Technol.*, vol. 25, no. 9, pp. 3463–3475, 2019, doi: 10.1007/s00542-018-4220-8.

[133] D. Chaudhuri, S. Kundu, and N. Chattoraj, “Design and analysis of MEMS based piezoelectric energy harvester for machine monitoring application,” *Microsyst. Technol.*, vol. 25, no. 4, pp. 1437–1446, 2019, doi: 10.1007/s00542-018-4156-z.

[134] D. S. Ibrahim, S. Beibei, O. A. Oluseyi, and U. Sharif, “Performance analysis of width and thickness tapered geometries on electrical power harvested from a unimorph piezoelectric cantilever beam,” in *2020 IEEE 3rd Int. Conf. Electron. Technol. ICET 2020*, pp. 100–104, 2020, doi: 10.1109/ICET49382.2020.9119588.

[135] A. Erturk and D. J. Inman, *Piezoelectric energy harvesting*, 1st ed. UK: John Wiley & Sons, 2011, pp 49–94.

[136] M. Zhu, E. Worthington, and J. Njuguna, “Analyses of power output of piezoelectric energy-harvesting devices directly connected to a load resistor using a coupled piezoelectric-circuit finite element method,” *IEEE Trans. Ultrason. Ferroelectr. Freq. Control*, vol. 56, no. 7, pp. 1309–1318, 2009, doi: 10.1109/TUFFC.2009.1187.

[137] G. Wang and Y. Lu, "An improved lumped parameter model for a piezoelectric energy harvester in transverse vibration," *Shock and Vibration*, vol. 2014, Article ID 935298, 2014, doi: https://doi.org/10.1155/2014/935298

[138] S. S. Rao, *Mechanical Vibrations*. Prentice Hall, USA. 2011, pp. 124–258.

[139] J. S. Rao, *Theory of machines through solved problem*, 1st Ed. New Age International, New Delhi, 1996, pp. 337–368.

[140] L. Tang, Y. Yang, and C. K. Soh, "Toward broadband vibration-based energy harvesting," *J. Intell. Mater. Syst. Struct.*, vol. 21, no. 18, pp. 1867–1897, 2010, doi: 10.1177/1045389X10390249.

[141] H. Madinei, H. Haddad Khodaparast, S. Adhikari, and M. I. Friswell, "Design of MEMS piezoelectric harvesters with electrostatically adjustable resonance frequency," *Mech. Syst. Signal Process.*, vol. 81, pp. 360–374, 2015, doi: 10.1016/j.ymssp.2016.03.023.

[142] L. Li, J. Xu, J. Liu, and F. Gao, "Recent progress on piezoelectric energy harvesting: structures and materials," *Adv. Compos. Hybrid Mater.*, vol. 1, no. 3, pp. 478–505, 2018, doi: 10.1007/s42114-018-0046-1.

[143] A. Akarapu, R. P. Nighot, L. Devsoth, M. Yadav, P. Pal, and A. K. Pandey, "Experimental and theoretical analysis of drag forces in micromechanical-beam arrays," *Phys. Rev. Appl.*, vol. 13, no. 3, p. 34003, 2020.

[144] S. Naval, P. K. Sinha, N. K. Das, A. Anand, and S. Kundu, "Bandwidth increment of piezoelectric energy harvester using multi-beam structure," in *2019 Devices for Integrated Circuit (DevIC)*, 2019, pp. 370–373.

[145] D. Benasciutti, L. Moro, S. Zelenika, and E. Brusa, "Vibration energy scavenging via piezoelectric bimorphs of optimized shapes," *Microsyst. Technol.*, vol. 16, no. 5, pp. 657–668, 2010, doi: 10.1007/s00542-009-1000-5.

[146] F. Goldschmidtboeing and P. Woias, "Characterization of different beam shapes for piezoelectric energy harvesting," *J. Micromechanics Microengineering*, vol. 18, no. 10, p. 104013, 2008, doi: 10.1088/0960-1317/18/10/104013.

[147] S. P. Matova, M. Renaud, M. Jambunathan, M. Goedbloed, and R. Van Schaijk, "Effect of length/width ratio of tapered beams on the performance of piezoelectric energy harvesters," *Smart Mater. Struct.*, vol. 22, no. 7, p. 075015, 2013, doi: 10.1088/0964-1726/22/7/075015.

[148] O. Pertin, P. Shrivas, K. Guha, K. S. Rao, and J. Iannacci, "New and efficient design of multimode piezoelectric vibration energy harvester for MEMS application," *Microsyst. Technol.*, pp. 1–9, 2021, doi: 10.1007/s00542-020-05108-w.

[149] S. S. Raju, M. Umapathy, and G. Uma, "Design and analysis of high output piezoelectric energy harvester using non uniform beam," *Mech. Adv. Mater. Struct.*, vol. 27, no. 3, pp. 218–227, 2020, doi: 10.1080/15376494.2018.1472341.

[150] M. N. Fakhzan and A. G. A. Muthalif, "Harvesting vibration energy using piezoelectric material: Modeling, simulation and experimental verifications," *Mechatronics*, vol. 23, no. 1, pp. 61–66, 2013, doi: 10.1016/j.mechatronics.2012.10.009.

[151] Alexander Blake, *Practical Stress Analysis in Engineering Design*, 2nd Ed. New York: CRC Press, 1989.

[152] M. Kurata, "On beams and columns of uniform strength solved by the method of calculus of variation," *Mem. Fac. Eng. Hokkaido Univ.*, vol. 8, no. 1, pp. 141–165, 1948.

[153] A. C. Ugural and S. K. Fenster, *Advanced Mechanics of Materials and Applied Elasticity*, 6th Edition. Pearson Education, 2011.

[154] A. Anand, S. Pal, and S. Kundu, "Multi-perforated energy-efficient piezoelectric energy harvester using improved stress distribution," *IETE J. Res.*, pp. 1–16, Apr. 2021, doi: 10.1080/03772063.2021.1913071.

[155] D. Berlincourt, H. Krueger, and C. Near, "Properties of Morgan electro ceramic ceramics," *Tech. Publ. TP-226*, Morgan Electro Ceramics. 2000.

[156] T. T. T. Le, F. Jost, and S. Sager, "Optimal control of vibration-based micro-energy harvesters," *J. Optim. Theory Appl.*, vol. 179, no. 3, pp. 1025–1042, 2018, doi: 10.1007/s10957-018-1250-4.

[157] V. J. Caetano and M. A. Savi, "Multimodal pizza-shaped piezoelectric vibration-based energy harvesters," *J. Intell. Mater. Syst. Struct.*, vol. 32, no. 20, pp. 2505–2528, 2021, doi: 10.1177/1045389X211006910.

[158] B. Y. Jing and K. S. Leong, "Demonstration of piezoelectric cantilever arrays for broadband vibration harvesting," in *2016 IEEE International Conference on Power and Energy (PECon)*, 2016, pp. 814–817, doi: 10.1109/PECON.2016.7951670.

[159] Y. J. Bong and K. Swee Leong, "Broadband energy harvesting using multi-cantilever based piezoelectric," *J. Telecommun. Electron. Comput. Eng.*, vol. 9, no. 3, pp. 111–116, 2017.

[160] D. Mažeika, A. Čeponis, and Y. Yang, "Multifrequency piezoelectric energy harvester based on polygon-shaped cantilever array," *Shock Vib.*, vol. 2018, p. 11, Article ID 5037187, 2018, doi: 10.1155/2018/5037187.

[161] V. J. Caetano and M. A. Savi, "Star-shaped piezoelectric mechanical energy harvesters for multidirectional sources," *Int. J. Mech. Sci.*, vol. 215 p. 106962, 2021, doi:https://doi.org /10.1016/j.ijmecsci.2021.106962.